Precision Deuteron Charge Radius Measurement with Elastic Electron-Deuteron Scattering

A. Gasparian (spokesperson and contact person), T. Hague, S. Mtingwa, R. Pedroni
North Carolina A&T State University, Greensboro, NC 27411

I. Akushevich, D, Byer, H. Gao (spokesperson), C.R. Howell, B. Karki, V. Khachatryan, G. Matousek, X. Li, A.P. Smith, E. van Nieuwenhuizen, B. Yu, Z. Zhao, J. Zhou
Duke University and Triangle Universities Nuclear Laboratory, Durham, NC 27708

C. Ayerbe, H. Bhatt, D. Bhetuwal, T. Chetry, B. Devkota, J. Dunne, D. Dutta (spokesperson), L. El-Fassi, A. Karki
Mississippi State University, Mississippi State, MS 39762

X. Bai, D. Di, S. Jian, N. Liyanage (spokesperson), K. Gnanvo, J. Matter, V. Nelyubin, H. Nguyen
University of Virginia, Charlottesville, VA 22904

J. Brock, C. Carlin, D. Gaskell, Y. Gotra, D. W. Higinbotham (spokesperson), C. Keith, J. Maxwell, D. Meekins, E. Pasyuk (spokesperson), S. Stepanyan, B. Wojtsekhowski
Thomas Jefferson National Accelerator Facility, Newport News, VA 23606

M. Khandaker
Energy Systems, Davis, CA 95616

C. Peng
Argonne National Lab, Lemont, IL 60439

W. Xiong
Syracuse University, Syracuse, NY 13244

L. Gan
University of North Carolina Wilmington, NC 28403

I. Larin, R. Miskimen
University of Massachusetts, Amherst, MA 01003

H.J. Karwowski
University of North Carolina at Chapel Hill, Chapel Hill, NC 27516
and Triangle Universities Nuclear Laboratory, Durham, NC 27708

A. Dolgolenko, V. Goryachev, V. Matveev, V. Tarasov
ITEP, Moscow, Russia

A. Shahinyan
Yerevan Physics Institute, Yerevan Armenia

E. Christy
Hampton University, Hampton VA 23669

and
The PRad Collaboration

Abstract

Recent high precision deuteron rms charge radius measurements performed by the CREMA collaboration at PSI using spectroscopy of muonic deuterium atoms demonstrated a $\sim 6\sigma$ discrepancy with the radius obtained from spectroscopy of ordinary deuterium atoms and the long-established CODATA-2014 world-average value. This created a new *"deuteron charge radius puzzle"* in hadronic physics. The puzzle remains unresolved even after the recent revision of the CODATA-2018 world average, which is essentially determined by the muonic result with its unprecedented precision (0.05%).

The uncertainty of previous ed electron scattering measurements are too large to contribute to a satisfactory resolution of this puzzle. We propose to perform a new high precision elastic ed scattering cross section measurement at very low scattering angles, $\theta_e = 0.7^\circ - 6.0^\circ$ (Q^2= 2×10^{-4} to 5×10^{-2} $(\mathrm{GeV/c})^2$) at $E_0 =$ 1.1 and 2.2 GeV, using the proposed PRad-II experimental setup with one major modification. To ensure the elasticity of the ed scattering process we will add a low energy Si-based cylindrical recoil detector within the windowless gas flow target cell. As in the PRad experiment, to control the systematic uncertainties associated with measuring the absolute ed cross section, a well known QED process, the ee Møller scattering will be simultaneously measured in this experiment. The proposed experiment will allow a high precision (0.22%) and essentially model independent extraction of the deuteron charge radius to address the newly developed *"deuteron charge radius puzzle"*.

Contents

1 Introduction

Elastic electron scattering has been a well established tool to determine the radii of nuclear charge distributions. The unique advantage of electron scattering is that, the well understood electromagnetic interaction being weak enables the separation of the scattering process from the effects of the strong nuclear force and other nuclear properties. The availability of intense and precisely controlled electron beams, such as the CW electron beam at Jefferson Lab, allows for very accurate measurements of the nuclear charge distributions. The charge radii of the lightest nuclei can also be extracted from laser spectroscopy of atomic hydrogen (H) and deuterium (D). The radii extracted from electron scattering and atomic spectroscopy were typically found to be consistent within experimental uncertainties. This allowed them to be combined together to obtain a "world average" value of the proton (r_p) and deuteron (r_d) root mean square (rms) charge radius, by a self-consistent least-squares adjustment of the fundamental physical constants, published in the CODATA compilations [1]. However, recently the most precise radii have been obtained from the spectroscopy of muonic atoms [2, 3, 4]. The radii obtained from these ultra-precise muonic atom measurements were found to be inconsistent with the CODATA values, as shown in Figs. 1 and 2.

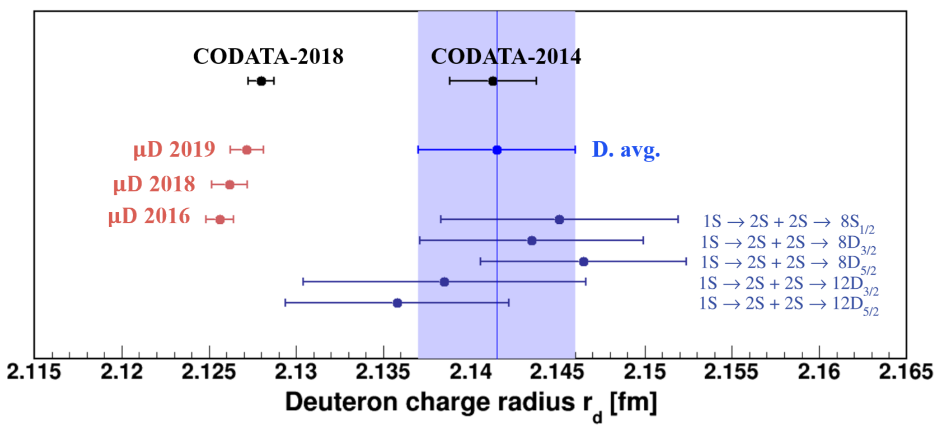

Figure 1: The CODATA values for the deuteron charge radius along with the existing data from atomic deuterium spectroscopy that was used to deduce the deuteron charge radius without relying on the value of the proton charge radius [10].

For example, the $\sim 7\ \sigma$ discrepancy between the CODATA and the muonic spectroscopy values for the proton charge radius gave rise to the "*Proton Radius Puzzle*" [5, 6]. A similar, more than $\sim 6\ \sigma$, discrepancy between the deuteron charge radius from spectroscopy of muonic deuterium and the CODATA-2014 value was reported recently [4]. It is tempting to dismiss such comparisons between r_p and r_d as redundant because the CODATA values of the two are highly correlated [1]. The large correlation is the result of the very precisely measured isotope shift of the $1S \rightarrow 2S$ transition in H and D obtained from cyclotron frequency measurements in a Penning trap [7, 8]. The accurately known isotope shift then yields a very accurate value for the difference of the (squared) deuteron and proton charge radii: $r_d^2 - r_p^2 = 3.82007(65)$ [9], which along with the elastic electron scattering on protons and deuterons determine the CODATA values of r_p and r_d respectively. Thus, it can be argued that the CODATA deuteron charge radius is larger than the muonic deuterium value only because the highly correlated and accurately determined proton charge radius is larger than the muonic hydrogen value. But, a recent re-analysis of the existing data from atomic deuterium spectroscopy was used to deduce a deuteron charge radius without relying on the value of the proton charge radius [10] (see Fig. 1). The newly deduced value is in excellent agreement with the CODATA value but still $\sim 3.5\ \sigma$ larger than the value obtained from muonic deuterium. This indicates that in addition to the "*Proton Radius Puzzle*" there also exists a "*Deuteron Radius Puzzle*". Unfortunately, all the $e-D$ scattering experiments to date, with their significantly larger uncertainties have not been able to address the discrepancy between the atomic deuterium and muonic deuterium measurements (see Fig. 2 top panel). The most recent $e-D$ scattering result (Sick *et al.*) [11] is a re-analysis of the world data on $e-D$ scattering and does not help discriminate between the atomic deuterium and muonic deuterium spectroscopy results. The situation calls out for a high precision $e-D$ scattering experiment that can directly address this as yet unresolved discrepancy.

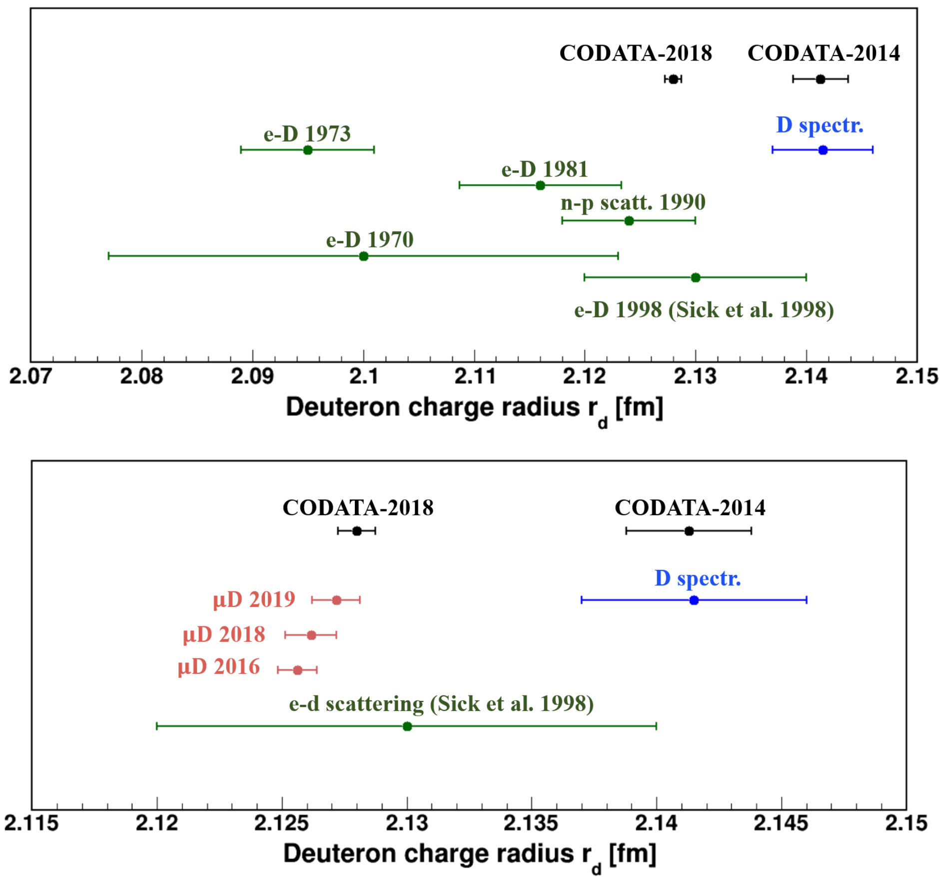

Figure 2: (top) The deuteron radius measurements using ed scattering and np scattering. The result of Sick *et al.* [11] is the re-analysis of the ed scattering world data. (bottom) The CODATA values for the deuteron charge radius along with measurements using spectroscopy of muonic atoms, electron scattering and atomic spectroscopy, reproduced from Ref. [4]. The point labeled as D-spectroscopy is the deuteron charge radius from just deuteron spectroscopy without using the proton charge radius as described in Ref. [10].

In order to address the "*Proton Radius Puzzle*", PRad, a new high precision electron scattering experiment, was completed at JLab in 2016 and the results were recently published [12]. This experiment included several unique features such as a new windowless cryo-cooled hydrogen gas flow target, a magnetic spectrometer free design using a high resolution electromagnetic calorimeter (HyCal) which allowed the experiment to reach the lowest four momentum transfer squared (Q^2) amongst electron scattering experiments. Two large area gas electron multiplier (GEM) chambers were also used to help improve the angular resolution. Finally, the simultaneous detection of Møller and elastic electron-proton (e-p) scattering events within the same experimental acceptance helped reduce many systematic uncertainties. The PRad experiment found a small r_p consistent within its uncertainties with the small radius measured by the muonic hydrogen experiments. The success of all of the unique features of the PRad experiment demonstrated the superiority of this technique. Based on the experience gained during the PRad experiment we are proposing a new set of measurements on deuterium using the same technique, but with an upgraded setup. The proposed experiment will enable the most precise measurement of the deuteron charge radius using electron scattering, with the ultimate goal of resolving the "*Deuteron Radius Puzzles*".

2 Physics Motivation

As the only bound two-nucleon system, the deuteron is of fundamental importance to nuclear physics and has been studied extensively both experimentally and theoretically. The wave function of the deuteron can be calculated accurately for a variety of nucleon-nucleon (NN) potentials. It is expected that at very low momentum transfer Q, where the non-nucleonic degrees of freedom and relativistic corrections are negligible, the electromagnetic properties of the deuteron, can be accurately predicted. The deuteron form factors at low Q are dominated by the parts of the deuteron wave function for which the two nucleons are far apart, and hence the deuteron's electromagnetic properties such as its rms charge radius should be determined just by the nucleon-nucleon (NN) interaction and the nucleon form factors, both of which are well known. The theoretical calculations of the rms radius of the deuteron are considered reliable as they are independent of the NN potential for a broad class of potentials and depends mostly on its well known binding energy and n-p scattering length [13]. This is why the deuteron rms radius is an ideal observable to compare experiments with theory.

2.1 Radius from Electron Scattering

The earliest experimental knowledge on the deuteron rms charge radius came from elastic electron-deuteron (e-d) scattering [14]. Although, e-d elastic scattering was first studied to learn about the neutron form factors, they were also used to extract the deuteron rms charge radius. In the Born approximation the cross section for elastic scattering from a nuclear target is given by [15];

$$\frac{d\sigma}{d\Omega} = \frac{d\sigma}{d\Omega}|_{NS}[A(Q^2) + B(Q^2)\tan^2\theta/2], \tag{1}$$

where $\frac{d\sigma}{d\Omega}|_{NS}$ is the cross section for the elastic scattering from a point-like and spinless particle with the mass of the nucleus, at electron incident energy of E_0, and, scattering angle θ. The structure functions $A(Q^2)$ and $B(Q^2)$ are related to the deuteron charge, electric quadrupole and magnetic dipole form factors G_{Cd}, G_{Qd} and G_{Md} respectively, as [16, 17];

$$\begin{aligned} A(Q^2) &= G^2_{Cd}(Q^2) + \frac{2}{3}\eta G^2_{Md}(Q^2) + \frac{8}{9}\eta^2 G^2_{Qd}(Q^2) \\ B(Q^2) &= \frac{4}{3}\eta(1+\eta)G^2_{Md}(Q^2), \end{aligned} \tag{2}$$

where $\eta = Q^2/4m_d^2$, the deuteron mass is given by m_d, $G_{Cd}(0) = 1, G_{Md}(0)/\mu_{Md} = 1$ and $G_{Qd}(0)/\mu_{Qd} = 1$, with μ_{Md} and μ_{Qd} being the deuteron magnetic moment and quadrupole moment respectively. The two structure functions are separated using the standard Rosenbluth separation method. At low Q^2 the contributions from the magnetic and quadrupole form factors are small and the rms charge radius can be obtained from the slope of the elastic e-d electric structure function $A(Q^2)$ as,

$$r_d^2 = -6[\frac{dA(Q^2)}{dQ^2}]_{Q^2=0}. \tag{3}$$

Information from elastic e-d scattering has been available since 1957 [18], but the overall normalization uncertainty in most measurements up to the mid-seventies was $\sim$ 5% [19]. Later measurements at Mainz were able to achieve uncertainties below 1% [20]. However, the ratio of e-d to e-p scattering can be determined much more precisely, for example an uncertainty of 0.13% on the ratio was reported in Ref. [20]. These ratios of cross sections are used to determine the deuteron rms matter (structure) radius, r_{md} instead of the rms charge radius. This is because the ratio of e-d to e-p scattering cross sections at low Q^2 provide the ratio of the experimental charge form factors, $R(Q^2) = \frac{G_{Cd}(Q^2)}{G_{Ep}(Q^2)}$, where G_{Ep} is the proton electric form factor, and the ratio of charge form factors can also be written as;

$$\frac{G_{Cd}(Q^2)}{G_{Ep}(Q^2)} = \left(1 + \frac{G_{En}}{G_{Ep}}\right) \frac{C_E(Q^2)}{\sqrt{1+\tau}} \frac{1}{1+cQ^2}, \tag{4}$$

where $C_E(Q^2)$ is called the deuteron structure factor and given by $C_E(Q^2) = 1 - \frac{1}{6}r_d^2 Q^2 + ...$, $G_{En} = -\frac{dG_{En}}{dQ^2}|_{Q^2=0}Q^2 + ...$, $G_{Ep}(Q^2) = 1 - \frac{1}{6}r_p^2 Q^2 + ...$, $\tau = Q^2/4m_p^2$, the factor $1/\sqrt{1+\tau}$ is the relativistic correction and the factor $\frac{1}{1+cQ^2}$ is the correction for non-nucleonic degrees of freedom. Neglecting terms of order Q^4 and higher we get;

$$R(Q^2) = \frac{G_{Cd}(Q^2)}{G_{Ep}(Q^2)} = 1 - \frac{Q^2}{6} r_x^2|_{Q^2=0}, \tag{5}$$

where $r_x^2 = r_{md}^2 + r_n^2 + \frac{3}{4}(\frac{\hbar}{m_p c})^2$, and $r_n^2 = -6\frac{dG_{En}}{dQ^2}|_{Q^2=0}$ is the neutron radius square which is known with high precision from the scattering of thermal neutrons on atomic electrons [21], and the term $\frac{3}{4}(\frac{\hbar}{m_p c})$ represents the relativistic Zitterbewegung corrections. In most analyses the measured ratio of cross sections $R(Q^2)$ is fitted to a polynomial;

$$R(Q^2) = \sum_{n=0}^{N} (-)^n a_n Q^{2n}, \tag{6}$$

and the mean square (ms) radius is deduced from $r_x^2 = 6a_1/a_0$. Finally, one can obtain the ms charge radius as $r_d^2 = r_{md}^2 + r_p^2$, where r_p^2 is the proton charge radius square. Thus, even though the ratio of e-d to e-p cross section is much more precise compared to the absolute e-d scattering cross section, one must use the proton charge radius in order to get the deuteron charge radius.

To date, elastic e-d scattering has been investigated in many experiments which cover a large range of Q (0.2 - 4.0 fm^{-1}), for a brief review see Ref. [11]. The most relevant among these, for rms radius extraction, are three measurements at low Q that have reached the highest accuracy [22, 20, 23]. Berard *et al.* [22] used cooled H_2 and D_2 gas targets to measure the ratio of cross sections relative to hydrogen over a Q range of 0.2-0.7 fm^{-1}. The deuterium cross sections were obtained by normalizing to the absolute cross section data on hydrogen. Simon *et al.* [20] used both gas and liquid targets to cover different ranges in Q, with a net coverage of 0.2-2.0 fm^{-1}. The hydrogen data collected on a gas target using a special small angle spectrometer served as the absolute cross section standard. Finally, Platchkov *et al.* [23] used a liquid deuterium target to cover a range of Q = 0.7 - 4.5 fm^{-1} with data collected on a liquid hydrogen target for absolute cross sections. As noted in Ref. [11] these publications did not adequately discuss all the systematic uncertainties, and sometimes important sources of uncertainty such as electron beam energy, beam halos e.t.c. are not mentioned.

Nonetheless, the extracted deuteron rms radius tended to be consistent with the calculated radius until about 1980 [13]. The situation changed in 1980 when the value of the proton charge radius was revised from the long accepted value of 0.805(11) fm to the new much larger value of 0.862(12) fm as a result of a measurement at Mainz [24]. Using the revised proton radius, the new value of the deuteron rms radius was in serious disagreement with the theoretical values given by the best models of the nuclear forces. This discrepancy between electron scattering results and theoretical calculations led several authors to explore potential corrections such as meson exchange currents [25], dispersive corrections [26], and energy dependence of the NN interaction [27], however the effect on the rms radius from these corrections were found to be very small. In 1996, Sick and Trautmann [28], re-analyzed the world data on e-d scattering and showed that much of the discrepancy originates from the fact that the Coulomb distortions were neglected in the Plane-Wave Born Approximation (PWBA) commonly used to analyze e-d scattering data. Although Coulomb distortions are small ($\sim 1\%$), the distortion effects are significant at the level of precision reported in the extraction of the rms radius. Once the Coulomb distortions were accounted for, the rms deuteron radius determined from electron scattering [11] ($r_d(e,e) = 2.13 \pm 0.01$ fm) was found to be consistent with theoretical calculations, radius determined from NN scattering [29]($r_d(NN) = 2.13 \pm 0.002$), and optical isotope shifts [30]($r_d(iso) = 2.1316 \pm 0.001$), as shown in Fig. 1.

It must be stressed that, all previous extractions of the deuteron charge radius have relied on deuteron cross sections measurements which were normalized to absolute cross section measurements on hydrogen. The 2010 measurement of the proton charge radius using muonic atoms which gave rise to the so called "*Proton Radius Puzzle*", forces us to consider alternative techniques that do not rely on the absolute hydrogen cross section. The normalization uncertainty can be better controlled if the measured cross section and cross section ratios are normalized to a well understood, pure QED cross section such as the Møller scattering cross section, instead of the $e-p$ cross section. The systematic uncertainties of the deuteron rms radius extracted from electron scattering can be further reduced by reaching lower values of Q^2 than previously achieved but simultaneously covering a wide enough range in Q^2 in a single experiment with a fixed detection system. The measurement proposed here incorporates all of these improvements and allows for a high precision extraction of the deuteron charge radius using a complementary technique that has completely different, and in our opinion, better control over systematic uncertainties compared to all previous measurements.

2.2 Radius from Atomic Deuteron Spectroscopy

The deuteron charge radius can also be obtained from the Lamb shift of the energy levels of atomic deuterium. The Lamb shift describes self-energy and other effects not included in the energies calculated from Dirac equation. One of its smaller contributions is the leading order nuclear structure (NS) contribution coming from the nuclear charge distribution acting only on the atomic nS state [31]:

$$L_{NS}(nS) = (Z\alpha)^4 m \frac{2}{3n^3}(mR_N)^2 = 1.566(Z^4/n^3)R_n^2 MHz \tag{7}$$

Here, Z is the nuclear charge, α is the fine structure constant, m is the electron mass, n is the principal quantum number, and R_N is the nuclear rms charge radius. It contributes about 0.888 MHz in the 2S state of deuterium if its charge radius is 2.13 fm. The experimental precision in measuring the Lamb shift in deuterium is currently 1.5 kHz [32], while an ultimate precision that could be orders of magnitude smaller [33]. This indicates that, assuming the accuracy of QED, Lamb-shift measurements can provide very precise information on the deuterium charge radius.

Another commonly used technique involves using the very precisely measured isotope shift of the $1S \rightarrow 2S$ transition in atomic hydrogen and deuterium [34, 35] to obtain a very accurate value of the difference of the squared deuteron and proton charge radii ($r_d^2 - r_p^2 = 3.82007(65)$ fm^2) [36]. This difference along with the proton charge radius extracted from Lamb shift measurements on atomic hydrogen is used to extract the deuteron charge radius. In fact the CODATA-2010 compilation uses only the radii from isotope shifts and from electron scattering in their evaluation of the current best value of the deuteron charge radius, $r_d =$ 2.1424 (21) fm [1].

Recently, Pohl *et al.* [10] have argued that the $1S \rightarrow 2S$ transitions in atomic deuterium have been previously measured [32, 35] with sufficient accuracy to extract the deuteron charge radius directly from these measurements rather than from the isotope shifts. Using these $1S \rightarrow 2S$ transitions they are able to deduce a deuteron charge radius of $r_d = 2.1415(45)$ fm. This value is independent of the proton charge radius and is consistent with the CODATA-2010 value but less accurate by a factor of 2. This is shown as the deuteron spectroscopy only value in Fig. 1.

2.3 Radius from Muonic Atom Spectroscopy

Muonic atoms are a special class of "exotic" atoms that provide access to the charge radius with much higher precision compared to other methods. In a muonic atom, the nucleus is orbited by one negative muon μ^-, instead of the usual electron. The muon's larger mass $m_\mu = 207 m_e$ results in a muonic Bohr radius that is smaller than the corresponding electronic Bohr radius by the ratio of the reduced masses, m_{red}. For μd, the $m_{red} = 196 m_e$, and as the Bohr radius reduces proportional to $1/m_{red}$, the overlap of the muon's wave function with the nuclear charge distribution increases as m_{red}^3. Hence, the wave function overlap is $\sim 10^7$ larger in μd compared to D. A measurement of the Lamb shift ($2P \rightarrow 2S$ energy difference) in μd is therefore extremely sensitive to the deuteron charge radius.

The CREMA collaboration has recently reported a deuteron charge radius r_d = 2.12562(78) fm, extracted from measurement of three $2P \rightarrow 2S$ transitions in μd [4]. This value is 2.7 times more accurate but $\sim 6\sigma$ smaller than the CODATA-2014 value. It is also 3.5σ smaller than the r_d obtained just from electronic deuterium spectroscopy [10].

Clearly, these results indicate that there is a "*deuteron radius puzzle*" in addition to the already known "*proton radius puzzle*".

2.4 Summary

There is a clear discrepancy in the deuteron rms charge radius obtained from electronic vs muonic atoms. The uncertainties in the electron scattering results are too large to have an impact on helping resolve the discrepancy. Therefore, there is an urgent need for an electron scattering experiment which can extract the deuteron radius more precisely than achieved to date. We propose an experiment which can accomplish the higher precision by using a single setup to measure e-d scattering and use a pure QED Møller scattering cross section for normalization rather than the e-p scattering cross section as have been done for all previous electron scattering experiments. This experiment will extract the deuteron charge radius from determining the charge form factor from measuring e-d scattering cross sections normalized to Møller scattering reaching unprecedentedly low values of Q^2.

The recently completed PRad experiment, has successfully demonstrated the techniques proposed in this experiment. The PRad experiment was able to reach the lowest Q^2 of any electron scattering experiment, and at the same time cover a wide range in Q in a single setting, to enable a precise extrapolation to $Q^2 = 0$. Using an upgraded version of the PRad setup we can measure e-d, e-p and Møller scattering in the same experimental setup. This will allow us to extract the most precise deuteron charge radius to date using electron scattering and thereby make a direct impact on the "*deuteron radius puzzle*".

3 Overview of the Proposed Measurement

The PRad collaboration at JLab developed and successfully ran a new magnetic-spectrometer-free, calorimetric experiment to measure the proton charge radius with a high precision. This method has a proven ability to reach extreme small scattering angles ($\theta_e = 0.7^\circ - 6.0^\circ$), as well as measure a well known QED process, $e^-e^- \to e^-e^-$ Møller scattering in parallel to the main process, to control the systematic uncertainties (see Sec. 4 for details).

We propose to perform a new electron scattering experiment on deuterium ($ed \to ed$) at small angles to address the newly developed *"deuteron charge radius puzzle"* in hadronic physics. As in the case of the $ep \to ep$ experiments, most of the $ed \to ed$ experiments quoted in literature have been performed with a traditional magnetic spectrometer method. Almost all of them implemented the detection of the recoiled deuterons to control the elasticity in the scattering process.

Similar to the PRad experiment, the proposed $ed \to ed$ scattering experiment will use the HyCal calorimeter together with an additional cylindrical Si-strip recoil detector. The proposed experimental apparatus will include:

(1) a windowless gas flow deuterium/hydrogen target;

(2) cylindrical Si-strip detector for detection of the recoiling low-energy deuterons;

(3) two planes of high position resolution GEM detectors to provide tracking of the scattered electrons and dramatically improve the Q^2 resolutions;

(4) high resolution and large acceptance, all $PbWO_4$ calorimeter (upgraded HyCal) located at $\sim$ 5.5 m downstream from the gas target to measure scattered electrons energies and positions (see Sec. 5). The readout electronics of the calorimeter will be upgraded to a fADC based system.

The proposed experimental design will allow the detection of the scattered electrons to angles as low as $\sim 0.7^\circ$ and recoiling deuteron nuclei to ensure the elasticity in the measured cross sections. Also, with its high acceptance and azimuthal symmetry, the setup will simultaneously detect multi-electron processes such as Møller scattering, for the first time in $ed \to ed$ scattering experiments.

3.1 Major advantage of the proposed experiment

This experiment will have three major improvements over previous $ed \to ed$ scattering experiments:

(1) The cross sections will be normalized to the well known QED process - Møller scattering, which will be measured simultaneously during the experiment within similar detector acceptances. This, arguably, will be a superior method to control the systematic uncertainties in the $ed \to ed$ cross sections.

(2) The proposed non-magnetic and calorimetric experiment will have the ability to reach extreme forward angles for the first time in ed scattering experiments. The experimental setup will cover the very forward angles $(0.7^\circ - 6^\circ)$, which in turn will allow for access to extremely low Q^2 range ($\sim$ $(2 \times 10^{-4}$ - $5 \times 10^{-2})$ $(\mathrm{GeV/c})^2)$ for few GeV incident electron beams. The lowest Q^2 range measured in ed scattering to date is from Ref. [22], where the minimum value of Q^2 reached is $2 \cdot 10^{-3}$ $(\mathrm{GeV/c})^2$. The very low Q^2 range is critically important since the rms charge radius of the deuteron is being extracted as the slope of the measured deuteron charge form factor, $G_{Cd}(Q^2)$ at the Q^2=0 point (see Eq. 3). We also understand that in going to very small Q^2 range, one has to take care of the uncertainties in the measured cross sections and Q^2, as well as, still provide a reasonably large interval of Q^2 to facilitate the extraction of the slope from G_{Cd} *vs.* Q^2 dependence.

In order to achieve these objectives we propose to run at two different beam energies, which will ensure coverage of a large enough range in Q^2 and also provide significant overlap in the Q^2 range for systematic studies. This will also help control the systematics of the radiative correction calculations. Moreover, the large range in Q^2 will be covered in a single setting without any change to the experimental setup, unlike in magnetic spectrometer experiments. This last point is a significant advantage over previous measurements.

(3) We propose to use a windowless gas flow target in this experiment. This will sufficiently cut down the experimental background from the target windows which is typical for most of the previous $ed \to ed$ experiments. With this type of gas target the majority of events detected in the setup will be produced by the two processes: $ed \to ed$ and $e^-e^- \to e^-e^-$, both of which are of direct interest in this proposed experiment. The electro-disintegration of the target deuterons ($ed \to epn$ inelastic breakup reaction) will constitute the major part of the background in this experiment. The suggested measurements of the time-of-flight (between the HyCal and the recoil detector) and the azimuthal angles (between GEMs and recoil detector) will effectively control this background (Sec. **??**).

As stated above, the proposed experimental setup will allow for a direct and simultaneous detection of both $ed \to ed$ and $e^-e^- \to e^-e^-$ processes. The trigger in this experiment (total energy deposited in calorimeter $\geq 20\%$ of E_0, as described in Sec. 4.4) will allow for the effective detection of the Møller events in both single-arm and double-arm modes. In the case of double-arm mode, already two selection criteria, the co-planarity and elasticity in energy (described in Sec. 6.2.2) will provide a good event selection in this rather low background experiment.

3.2 Normalization to the Møller cross section

The $ed \to ed$ elastic cross sections in this proposed experiment will be normalized to the $e^-e^- \to e^-e^-$ Møller cross sections, which can be calculated with a sub-percent accuracy within the QED framework, including the radiative corrections.

The experimental differential cross sections for $ed \to ed$ scattering can be written as:

$$\left(\frac{d\sigma}{d\Omega}\right)_{ed}(Q_i^2) = \frac{N_{\text{exp}}^{\text{yield}}\,(ed \to ed \text{ in } \theta_i \pm \Delta\theta)}{N_{\text{beam}}^{e^-} \cdot N_{\text{tgt}}^{\text{D}} \cdot \varepsilon_{\text{geom}}^{ed}\,(\theta_i \pm \Delta\theta) \cdot \varepsilon_{\text{det}}^{ed}}\,. \tag{8}$$

On the other hand, the differential cross sections for the Møller process, measured simultaneously in this experiment, will have a similar dependence on the experimental quantities:

$$\left(\frac{d\sigma}{d\Omega}\right)_{e^-e^-} = \frac{N_{\text{exp}}^{\text{yield}}\,(e^-e^- \to e^-e^-)}{N_{\text{beam}}^{e^-} \cdot N_{\text{tgt}}^{\text{D}} \cdot \varepsilon_{\text{geom}}^{e^-e^-} \cdot \varepsilon_{\text{det}}^{e^-e^-}}\,, \tag{9}$$

where $N_{\text{exp}}^{\text{yield}}$ $(ed \to ed \text{ in } \theta_i \pm \Delta\theta)$ is the number of elastically scattered $ed \to ed$ events inside a particular azimuthally symmetric ring on GEM/HyCal with polar angles in $(\theta_i \pm \Delta\theta)$ range which defines the $Q_i^2 \pm \Delta Q^2$ for a fixed incident energy (see Fig. 3); $N_{\text{exp}}^{\text{yield}}\,(e^-e^- \to e^-e^-)$ is the same quantity as for ed, defined in three different ways described below; $N_{\text{beam}}^{e^-}$ is the number of beam electrons that passed through the target with the number of D atoms/cm^2 - $N_{\text{tgt}}^{\text{D}}$, during the measurement; $\varepsilon_{\text{geom}}^{ed}\,(\theta_i \pm \Delta\theta)$ is the geometrical acceptance of the $(\theta_i \pm \Delta\theta)$ ring for the $ed \to ed$ reaction; $\varepsilon_{\text{geom}}^{e^-e^-}$ is the same for the $e^-e^- \to e^-e^-$ process and it will be calculated in three different ways depending on the accepted method for the Møller process, and it is described below; $\varepsilon_{\text{det}}^{ed}$ and $\varepsilon_{\text{det}}^{e^-e^-}$ are the detection efficiencies of the particular elements of the setup for the scattered electrons.

The ratio of Eqs. 8 to 9 will relate the ed cross sections relative to the e^-e^- Møller cross sections, as:

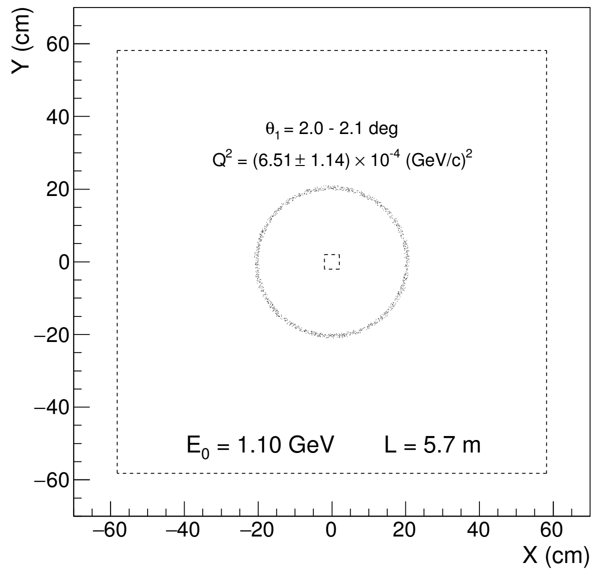

Figure 3: The simulated $X-Y$ position distribution of a single Møller scattered electron in the calorimeter at $E_0 = 1.1$ GeV. The angular range of the detected electron is $\theta_1 = 2.0^\circ - 2.1^\circ$ giving a Q^2 range of $Q^2 = (6.5 \pm 1.1) \cdot 10^{-4}$ $(\mathrm{GeV/c})^2$.

$$\left(\frac{d\sigma}{d\Omega}\right)_{ed}(Q_i^2) = \left[\frac{N_{\mathrm{exp}}^{\mathrm{yield}}\,(ed \to ed \;\mathrm{in}\; \theta_i \pm \Delta\theta)}{N_{\mathrm{exp}}^{\mathrm{yield}}\,(e^-e^- \to e^-e^-)} \cdot \frac{\varepsilon_{\mathrm{geom}}^{e^-e^-}}{\varepsilon_{\mathrm{geom}}^{ed}} \cdot \frac{\varepsilon_{\mathrm{det}}^{e^-e^-}}{\varepsilon_{\mathrm{det}}^{ed}}\right] \left(\frac{d\sigma}{d\Omega}\right)_{e^-e^-}. \tag{10}$$

Right away, the two major sources of systematic uncertainties, N_{beam}^{e} and $N_{\mathrm{tgt}}^{\mathrm{H}}$, in the above ratio which dominated in the previous experiments are simply canceling out in this proposed experiment.

The remaining two sources of systematic uncertainties: the ratio of the geometrical uncertainties $\left(\varepsilon_{\mathrm{geom}}^{e^-e^-}/\varepsilon_{\mathrm{geom}}^{ed}\right)$ and the detection efficiency $\left(\varepsilon_{\mathrm{det}}^{e^-e^-}/\varepsilon_{\mathrm{det}}^{ed}\right)$ will have a different impact on the final systematic uncertainties depending on the selection method of the Møller events. Both scattered electrons from the Møller process will be detected by two GEM detector layers and HyCal, as in the proposed PRad-II experiment. However, the requirement to detect the recoiling deuteron nucleus will introduce a sizable asymmetry in both detection efficiency $\varepsilon_{\mathrm{det}}^{ed}$ and geometrical acceptance $\varepsilon_{\mathrm{geom}}^{ed}$ of the $ed \to ed$ reaction *vs.* Møller. Therefore, these quantities will have contributions from the recoil detector which we plan to determine experimentally during the calibration runs.

3.3 Calibration of the recoil detector

Both detection efficiency $\varepsilon_{\mathrm{det}}^{ed}$ and geometrical acceptance $\varepsilon_{\mathrm{geom}}^{ed}$ of the recoil detector will be measured during special runs with hydrogen gas in the windowless target maintained at the same pressure as the deuterium gas during the production run. The kinematics of the $ep \to ep$ scattering is very similar to the $ed \to ed$ elastic scattering process at these very forward scattering angles. In both cases the proton and deuteron are recoiling with a similar polar angles, very close to 90° (see Figs. 4 and 5).

Fig. 6 shows the similarity of the simulated z-acceptance for both $ep \to ep$ and $ed \to ed$ elastic scattering processes in our setup for a slice of electron scattering angles around 2° at 1.1 GeV beam energy. The active length of the Si-strip detectors is selected to be shorter than the effective and relatively uniform part of the gas flow target in order to include similar target length for both scattering processes and for each

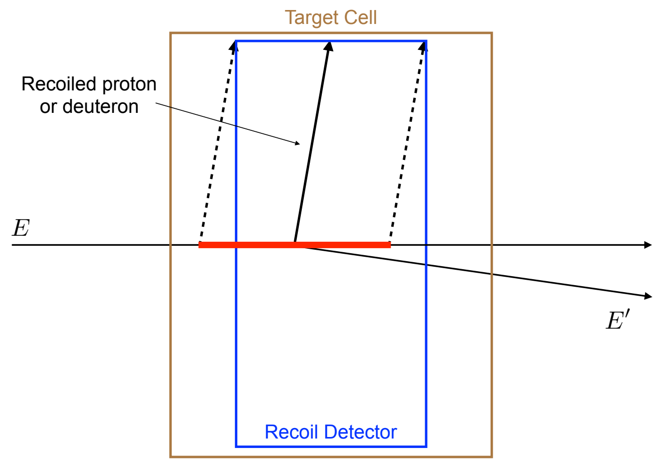

Figure 4: Schematic of the z-acceptance for the $ep \to ep$ and $ed \to ed$ elastic scattering processes.

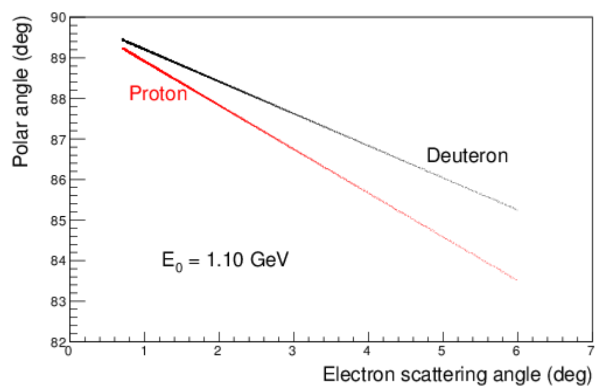

Figure 5: The simulated distribution of the deuteron (black) and proton (red) polar angle *vs.* electron scattering angle for the $ep \to ep$ and $ed \to ed$ elastic scattering processes at $E_0 = 1.1$ GeV.

scattering angle. The simulated density profile of hydrogen gas in the target cell is shown in Fig. 7, the density profile for deuterium should be identical.

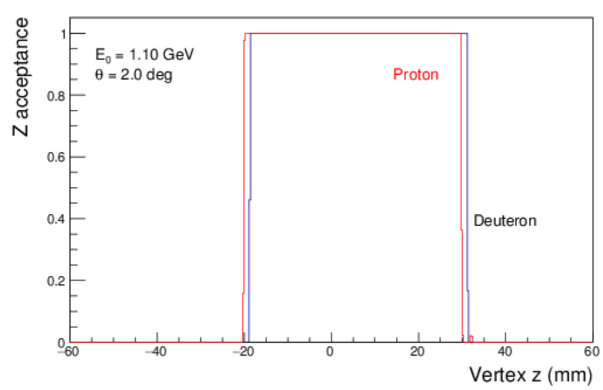

Figure 6: The z-vertex acceptance for $ed \to ed$ and $ep \to ep$ for a slice of electron scattering angles around 2° at $E_0 = 1.1$ GeV.

During the recoil detector calibration run we plan to accumulate experimental data for the $ep \to ep$, and

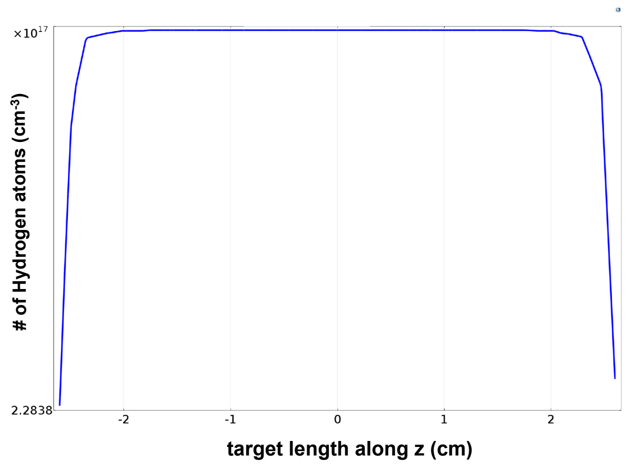

Figure 7: The simulated density distribution along the z-direction for hydrogen gas injected into the target cell (done using the COMSOL package).

simultaneously for the $e^-e^- \to e^-e^-$, with high statistics (similar to the main $ed \to ed$ process, $\sim 0.2\%$ per Q^2 bin). That will allow us to extract a similar ratio as in the Eq. 10, only for the hydrogen target:

$$\left(\frac{d\sigma}{d\Omega}\right)_{ep}(Q_i^2) = \left[\frac{N_{\mathrm{exp}}^{\mathrm{yield}}\,(ep \to ep \text{ in } \theta_i \pm \Delta\theta)}{N_{\mathrm{exp}}^{\mathrm{yield}}\,(e^-e^- \to e^-e^-)} \cdot \frac{\varepsilon_{\mathrm{geom}}^{e^-e^-}}{\varepsilon_{\mathrm{geom}}^{ep}} \cdot \frac{\varepsilon_{\mathrm{det}}^{e^-e^-}}{\varepsilon_{\mathrm{det}}^{ep}}\right]\left(\frac{d\sigma}{d\Omega}\right)_{e^-e^-}. \tag{11}$$

The ratio of the geometric acceptances $\left(\varepsilon_{\mathrm{geom}}^{e^-e^-}/\varepsilon_{\mathrm{geom}}^{ed}\right)$ and the detection efficiencies $\left(\varepsilon_{\mathrm{det}}^{e^-e^-}/\varepsilon_{\mathrm{det}}^{ed}\right)$ needed for the cross section in Eq. 10 can be measured by using the differential cross sections, $\left(\frac{d\sigma}{d\Omega}\right)_{ep}$, measured in the PRad experiment with a high precision.

In addition, we also plan to use the deuteron and proton beams from the Tandem accelerator at TUNL to measure the detector efficiency for deuterons with kinetic energy in the 1 - 15 MeV range and protons with kinetic energy of 1 - 25 MeV. These measurements will be used to form a ratio of the proton to deuteron detection efficiency as a function of energy. During the experiment each $e - D$ run will be interspersed with periodic $e - p$ runs. The $e - p$ runs will be used to monitor the proton detection efficiency of the recoil detector using the over-determined kinematics of $e - p$ scattering. The measured proton detection efficiency along with the ratio of the proton to deuteron detection efficiency measured at TUNL will be used to determine the deuteron detection efficiency. In addition a α-source based system will be used monitor the time dependence of the efficiency.

3.4 Møller event selection methods

We are planning to use three different approaches for the identification of the Møller events to reduce systematics in precise determination of the Møller scattering process.

3.4.1 Single-arm Møller event selection method

The proposed experimental setup (see Sec. 5) is optimized such that both Møller scattered electrons will be detected in the GEM/HyCal for angles $\geq 0.7°$ (see Sec. 6.2.2. However, looking at Eq. 10 for the case when one defines the Møller process inside the same angular $(\theta_i \pm \Delta\theta)$ ring (see Fig. 3) with one of the scattered electrons detected (single-arm Møller method), then we get $\varepsilon_{\mathrm{geom}}^{ed} = \varepsilon_{\mathrm{geom}}^{e^-e^-}$ and $\varepsilon_{\mathrm{det}}^{ed} = \varepsilon_{\mathrm{det}}^{e^-e^-}$ having in mind the different energy values of these electrons. With that, Eq. 10 becomes:

$$\left(\frac{d\sigma}{d\Omega}\right)_{ed}(Q_i^2) = \left[\frac{N_{\text{exp}}^{\text{yield}}\,(ed \to ed \text{ in } \theta_i \pm \Delta\theta)}{N_{\text{exp}}^{\text{yield}}\,(e^-e^- \to e^-e^-)}\right]\left(\frac{d\sigma}{d\Omega}\right)_{e^-e^-} \tag{12}$$

and, therefore, allows for a determination of the ed scattering cross sections essentially without systematic uncertainties related to the experimental apparatus.

Since the $e^-e^- \to e^-e^-$ is a two-body reaction, the experimental scattering angle of one of the electrons, together with the well known incident beam energy $(\Delta E/E = 10^{-4})$), will define the kinematics of the process. With that, the measured energy in the calorimeter (E_{meas}) can be used to select the events in the experiment. Figure 8 demonstrates the the energy resolution of the calorimeter is sufficient for a high level of confidence that this selection criterion alone will allow for an effective selection of events in this low-background experiment. Figure 9 also demonstrates the effective separation of Møller events from the ed elastic scattered events for angles $\theta_e > 0.7°$, planned for this experiment. The Møller event generator includes radiative effects, developed for the PRad experiment [37]. The radiative corrections for the $ed \to ed$ process are being developed based on the formalism for $ep \to ep$ that was implemented for the PRad experiment.

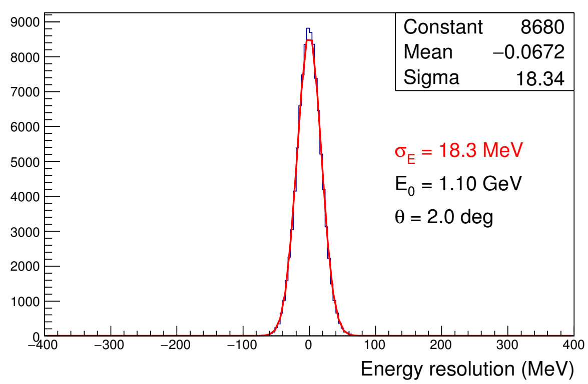

Figure 8: The simulated energy resolution for detecting a single Møller scattered electron in the calorimeter at $E_0 = 1.1$ GeV and $\theta_e = 2°$. The value of the resolution was obtained from the PRad experiment.

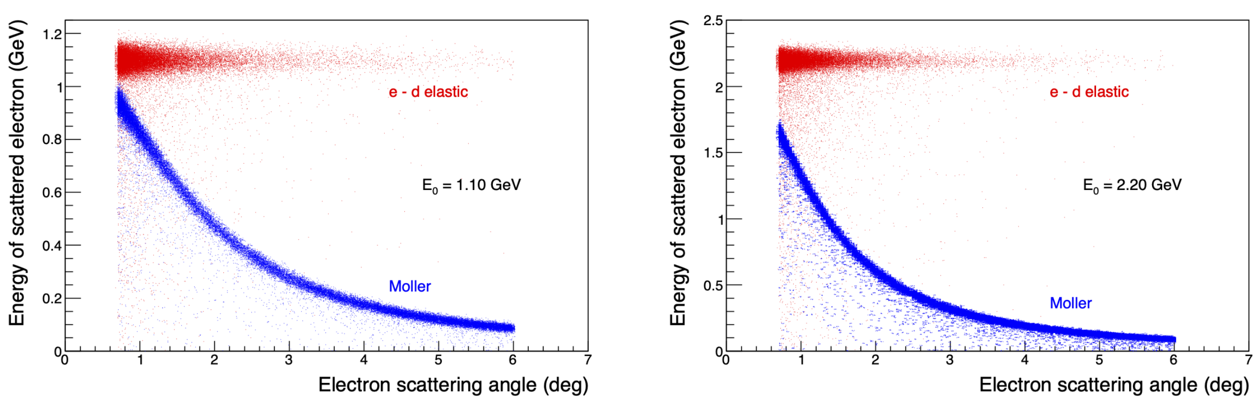

Figure 9: The simulated energy *vs.* scattering angle distribution of $e - d$ elastic and one of the Møller scattered electrons at $E_0 = 1.1$ GeV (left) and at $E_0 = 2.2$ GeV (right). The ed and Møller event generators includes radiative effects, developed for the PRad experiment and the ed process.

3.4.2 Coincident event selection method

As already mentioned above, the proposed experiment is optimized in a way that both electrons from $e^-e^- \to e^-e^-$ will be detected in the calorimeter for angles $\theta_e > 0.7°$. We will also explore the selection of Møller events in coincidence. As illustrated in Fig. 10, this method, in addition to the same Q_i^2 ring $(\theta_i \pm \Delta\theta)$, will introduce a second ring on the calorimeter for the detection of the second Møller scattered electron. As a consequence, it may introduce different geometrical acceptances and detection efficiencies for the particular Q^2. It can be calculated by Monte Carlo simulations and tested by the extracted Møller cross sections.

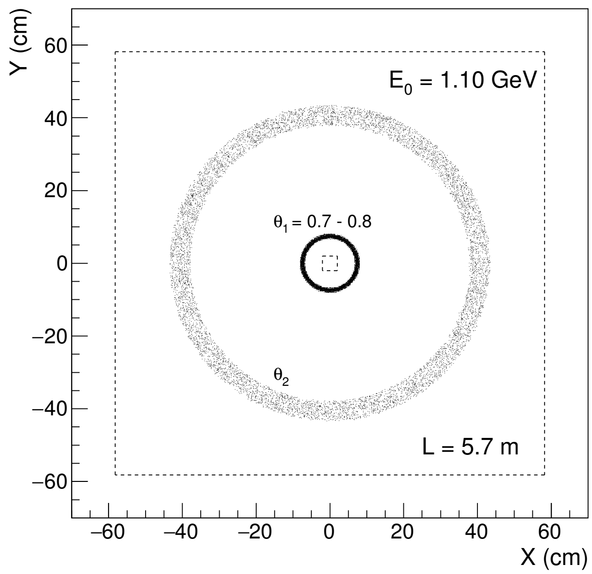

Figure 10: The simulated $X-Y$ position distribution of the two Møller scattered electrons on the HyCal calorimeter at a distance of $\sim$ 5.7 m from the target at an incident beam energy of 1.1 GeV. The distribution of the second electron is shown as the outer ring θ_2 when the first electron is in the range $\theta_1 = 0.7° - 0.8°$. The outside square box is the size of the HyCal calorimeter.

3.4.3 Integrated Møller cross section method

In this case, we will normalize the ed cross sections to the Møller cross sections extracted from the entire fiducial volume of the calorimeter for all Q^2 values. With that, Eq. 10 becomes:

$$\left(\frac{d\sigma}{d\Omega}\right)_{ed}(Q_i^2) = \left[\frac{N_{\rm exp}^{\rm yield}\,(ed,\ \theta_i \pm \Delta\theta)}{N_{\rm exp}^{\rm yield}\,(e^-e^-,\ \text{on PbWO}_4)}\right] \frac{\varepsilon_{\rm geom}^{e^-e^-}(\text{all PbWO}_4)}{\varepsilon_{\rm geom}^{ed}(\theta_i \pm \Delta\theta)} \frac{\varepsilon_{\rm det}^{e^-e^-}(\text{all PbWO}_4)}{\varepsilon_{\rm det}^{ed}(\theta_i \pm \Delta\theta)} \cdot \left(\frac{d\sigma}{d\Omega}\right)_{e^-e^-}, \tag{13}$$

with $\left(\frac{d\sigma}{d\Omega}\right)_{e^-e^-}$ integrated over the HyCal/GEM acceptance.

3.5 Summary

The proposed experiment will measure the $ed \to ed$ elastic cross section with high precision over a wide range of Q^2 ($2 \times 10^{-4} \leq Q^2 \leq 5 \times 10^{-2}$ GeV^2). This experiment will reach the lowest Q^2 measured in electron scattering while at the same time covering a large range in Q^2. It will use a new calorimetric technique that allows normalization to the pure QED process of Møller scattering that is detected simultaneously with the ed elastic scattering process with the same detector acceptance. This technique was successfully demonstrated during the PRad experiment and allows excellent control over systematic uncertainties. The proposed experiment will reuse the PRad setup with two major modifications; a new cylindrical Si-strip recoil detector for ensuring elasticity and a second pair of GEM chambers to improve the vertex and Q^2 resolutions. Given the reliance on the PRad technique and setup, we will discuss some of the key features and the successes of the PRad experiment in the next section.

4 Characteristics of the PRad Experimental Setup

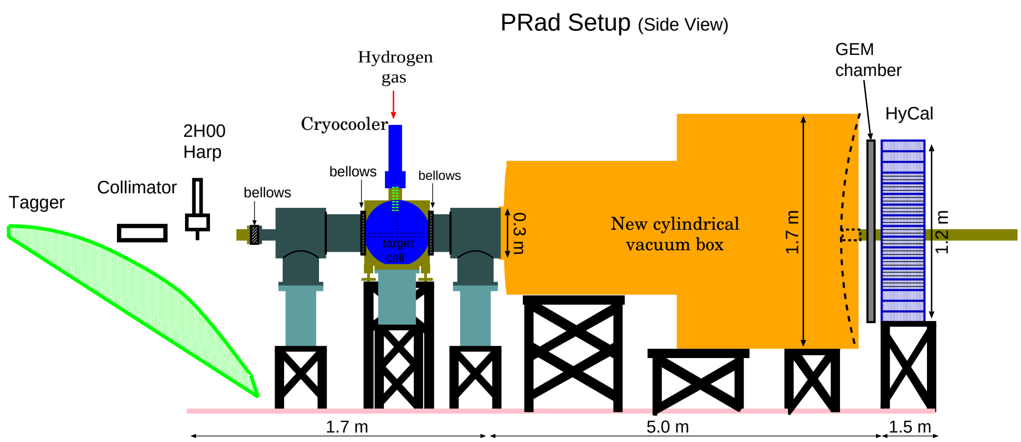

Figure 11: A schematic of the experimental setup used during the PRad experiment.

Last year this collaboration successfully ran the Proton Charge Radius (PRad) experiment at JLab. The PRad experiment was developed and assembled in a short few years since its full approval with "A"rating by PAC40, to measure the proton charge radius with a magnetic-spectrometer-free setup employing a high resolution and large acceptance calorimeter, that allowed for the ep scattering cross section to be normalized to the well known $e^-e^- \to e^-e^-$ Møller QED process. The PRad experiment included (1) a windowless gas flow hydrogen target used for the first time at JLab, (2) a large volume vacuum chamber with a single thin window (3) a pair of large area GEM chambers and (4) a high resolution HyCal calorimeter located about 5.6 m downstream of the target. The PRad ran during May-June 2016 utilizing a 1.1 and 2.2 GeV CW electron beam, with a width of 25μm and a position stability of better than $\pm$ 250 μm. The experiment was able to reach the lowest Q^2 (2.0 $\times$ 10^{-4} GeV^2) of any ep scattering experiment and at the same time covered a large range in Q^2 (2.0$\times 10^{-4}$ - 5$\times$ 10^{-2} GeV^2). A schematic of the experimental setup is shown in Fig. 11 and the major elements are described in the subsections below.

4.1 Windowless gas flow target

The PRad target had a thickness of $\sim 2.5 \times 10^{18}$ hydrogen atoms/cm^2. This high density was reached by flowing cryo-cooled hydrogen gas (at 19.5° K) through the target cell with a 40 mm long and 63 mm diameter cylindrical shape thin copper pipe. The side windows of this cell was covered by a thin (7.5 μm) kapton film with 2 mm holes in the middle for the passage of the electron beam through the target. Four high capacity turbo-pumps was used to keep the pressure in the chamber (outside the cell) on the ~ 2.3 mtorr level while the pressure inside the cell was ~ 470 mtorr.

The target cell was specifically designed to create a large pressure difference between the gas inside the cell and the surrounding beam line vacuum.

Figure 12 (left) is a cut-thru drawing of the PRad target chamber and shows most of its major components. High-purity hydrogen gas (>99.99%) was metered into the target system via a 0–10 slpm mass flow controller. Using a pair of remotely actuated valves, the gas was either directed into the target cell for production data-taking, or into the target chamber for background measurements. Before entering the cell, the gas was cooled to cryogenic temperatures using a two-stage pulse tube cryocooler[1] with a base

[1]Cryomech model PT810

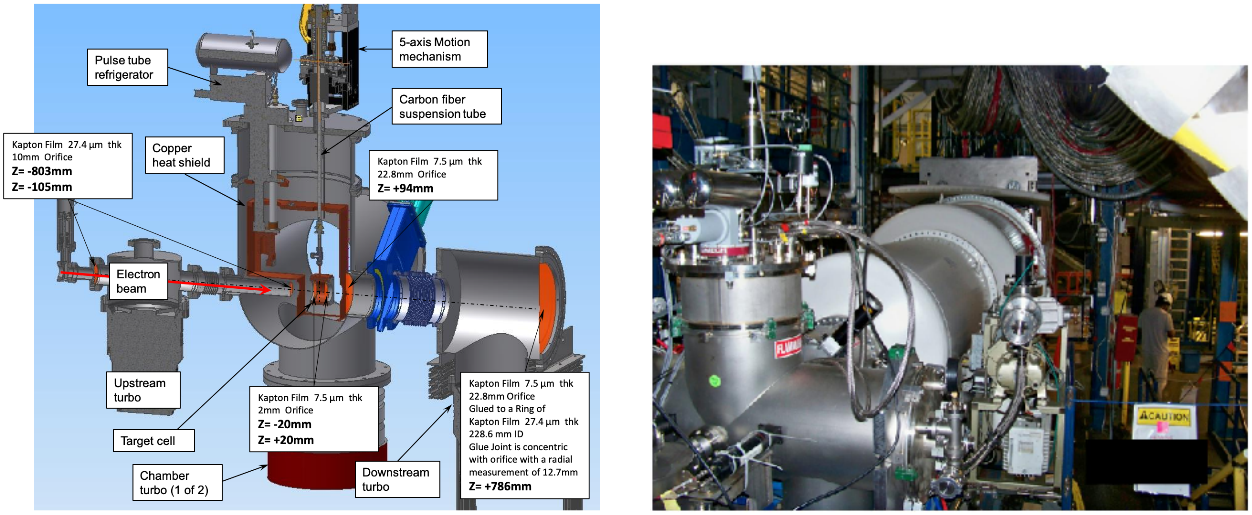

Figure 12: (left)Annotated drawing of the PRad gas flow target indicating most of the target's main components. The location and dimensions of various polyimide pumping orifices are shown, where Z is the distance from target center. The direction of the electron beam is indicated by a red arrow. (right) Downstream view of the PRad target in the beamline.

temperature of 8 K and a cooling power of 20 W at 14 K. The cryocooler's first stage serves two purposes. It cools a tubular, copper heat exchanger that lowers the hydrogen gas to a temperature of approximately 60 K, and it also cools a copper heat shield surrounding the lower temperature components of the target, including the target cell itself. The second stage cools the gas to its final operating temperature and also cools the target cell via a 40 cm long, flexible copper strap. The temperature of the second stage was measured by a calibrated cernox thermometer[2] and stabilized at approximately 20 K using a small cartridge heater and automated temperature controller.

The target cell, shown in Fig. 13, was machined from a single block of C101 copper. Its outer dimensions are 7.5$\times$ 7.5 $\times$ 4.0 cm^3, with a 6.3 cm diameter hole along the axis of the beam line. The hole is covered at both ends by 7.5 μm thick polyimide foils, held in place by aluminum end caps. Cold hydrogen gas flows into the cell at its midpoint and exits via 2 mm holes at the center of either kapton foil. The holes also allow the electron beam to pass through the H_2 gas without interacting with the foils themselves, effectively making this a "windowless" gas target. Compared to a long thin tube, the design of a relatively large target cell with small orifices on both ends has two important advantages. First, it produce a more uniform density profile along the beam path, allowing a better estimate of the gas density based upon its temperature and pressure. Second, it eliminates the possibility of electrons associated with beam halo scattering from the 4 cm long cell walls. Instead, the halo scatters from the 7.5 μm thick polyimide foils. A second calibrated cernox thermometer, suspended inside the cell, provides a direct measure of the gas temperature. The gas pressure was measured by a capacitance manometer located outside the vacuum chamber and connected to the cell by a carbon fiber tube approximately one meter long and 2.5 cm in diameter. The same tube is used to suspend the target cell, in the center of the vacuum chamber, from a motorized 5-axis motion controller. The controller can be used to position the target in the path of the electron beam with a precision of about $\pm$10 μm. It was also used to lift the cell out of the beam for background measurements. Also, two 1 μm thick foils, carbon and aluminum, were attached to the bottom of the copper target cell for additional background and calibration measurements. High-speed turbomolecular pumps were used to evacuate the hydrogen gas as it left the target cell and maintain the surrounding vacuum chamber and beam line at very

[2]Lakeshore Cryotronics

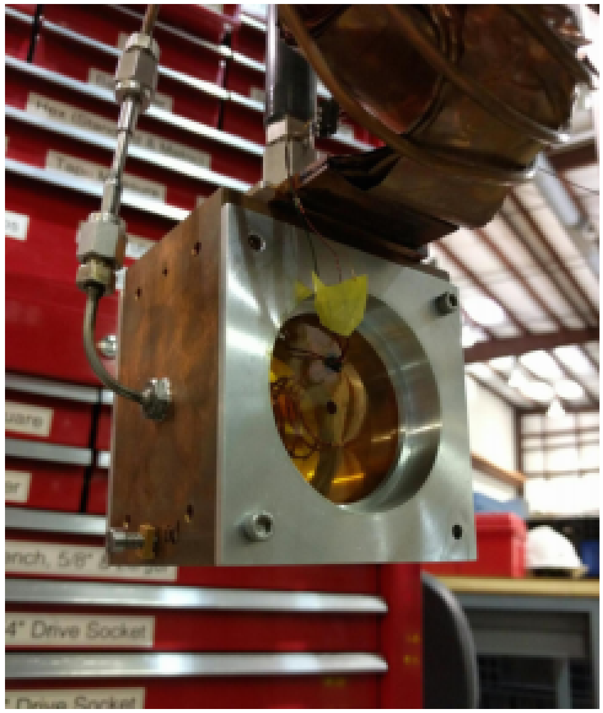

Figure 13: The PRad target cell. Hydrogen gas, cooled by the pulse tube cryocooler, enters the cell via the tube on the left. The cell is cooled by a copper strap attached at the top, and is suspended by the carbon tube directly above the cell. The 2 mm orifice is visible at the center of the polyimide window, as are the wires for a thermometer inside the cell. Two 1 μm solid foils of aluminum and carbon attach to the cell bottom, but are not shown in the photograph.

low pressure. Two pumps, each with a nominal pumping speed of 3000 l/s, were attached directly under the chamber, while pumps with 1400 l/s speed were used on the upstream and downstream portions of the beam line. A second capacitance manometer measured the hydrogen gas pressure inside the target chamber, while cold cathode vacuum gauges were utilized in all other locations.

Polyimide pumping orifices were installed in various locations to limit the extent of high pres- sure gas along the path of the beam. With this design, the density of gas decreases significantly outside the target cell, with 99% of scattering occurring within the 4 cm length of the cell.

4.1.1 Target performance

During the PRad experimet 600 sccm cold H_2 gas was flown through the target cell. Under these conditions, typical pressure and temperature measurements inside the target cell were 0.48 torr and 19.5 K, respectively, resulting in a gas density of 0.83 mg/cm^3. [**?**]. Table 1 gives typical pressure measurements obtained in other regions of the electron beam path. The hydrogen areal density is calculated as the product of the gas number density and the length of the region. In all regions except the target cell, a room temperature of 293 K is assumed when calculating the gas density. The vast majority of the was confined to the 4 cm long target cell, with the majority of the remaining gas being measured in the 5 m long, 1.8 m diameter vacuum chamber just upstream of the calorimeter. Here the achievable vacuum pressure was limited by the conductance between the chamber and its vacuum pump. Two types of background measurements were made. In the first, the H_2 gas flow was main- tained at the same 600 sccm, but the gas was directed into the vacuum chamber rather than the target cell. In this case, the chamber pressure increased slightly to 2.9 mtorr, and the cell

Table 1: Hydrogen gas pressures and areal densities for the PRad beam line. Refer to Fig. 12 (left) for more details.Room temperature gas is assumed in calculating the areal density of all regions except Region 1 (target cell), where a temperature of 19.5 K was used.

Region	Length (cm)	Pressure (torr)	Areal density (atoms/cm^2)	Percentage of total
Target cell	4	0.48	1.9×10^{18}	98.97
Upstream beamline	300	2.2×10^{-5}	2.0×10^{14}	0.02
Upstream chamber	71	5.7×10^{-5}	2.6×10^{13}	0.00
Target chamber	14	2.3×10^{-3}	2.1×10^{15}	0.11
Downstream chamber	71	3.0×10^{-4}	6.1×10^{14}	0.07
Vacuum chamber	400	5.2×10^{-4}	7.2×10^{15}	0.83

temperature warmed to 32 K. For the second type of background measurements, the gas flow was set to zero, in which case both the cell and chamber pressures dropped below 0.001 torr.

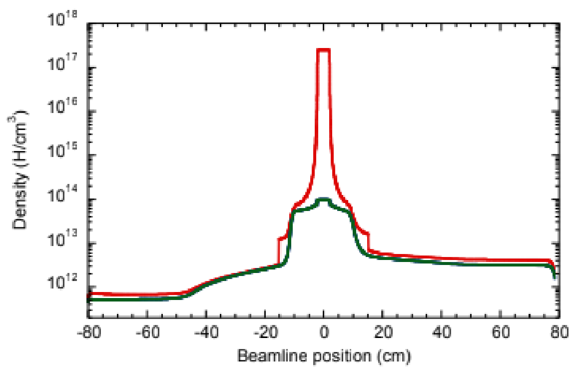

Figure 14: Density profile of hydrogen atoms along the electron beam line. Here, the target cell is centered at 0 cm, and the electron beam transverses the target from negative to positive values. The red line indicates a measurement with 600 sccm of hydrogen flowing into the target cell. The green line indicates a background measurement with the same flow of gas directly into the target vacuum chamber.

The measured temperature values, together with the inlet gas flow rate, pumping speeds of the pumps, and the detailed geometry of the target system were used to simulate the hydrogen density profile in the target using the COMSOL Multiphysics ® simulation package. The average pressure obtained from the simulation agreed with the measured values within 2 mTorr for both the target cell and the target chamber, under the PRad production running conditions. Fig. 14 shows the simulated density profile along the beam path for both the full target cell configuration and the "full chamber" background configuration. During the PRad experiment the target pressure and temperature remained stable throughout. The variation of target pressure and temperature with time is shown in Fig. 15.

4.2 Large volume vacuum chamber

For the PRad experiment a new large ∼5 m long, two stage vacuum chamber was designed and built. It extended from the target to the GEM/HyCal detector system. There was a single 1.7 m diameter, 63 mil thick Al. window at one end of the vacuum chamber, just before the GEM detector. A 2-inch diameter beam pipe was attached using a compression fitting to the center of the thin window. This design ensured that the

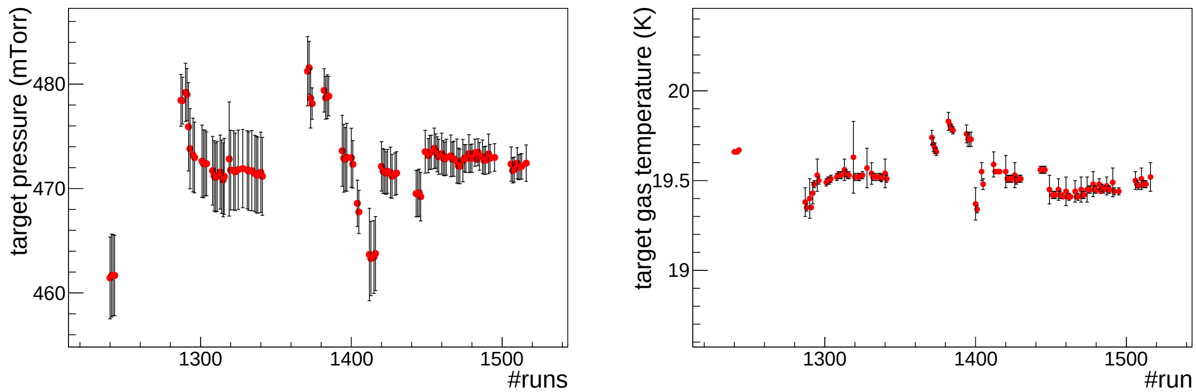

Figure 15: The variation of PRad target pressure and temeperature *vs.* run number. Each run was about 1 hr long.

electron beam did not encounter any additional material other than the hydrogen gas in the target cell, all the way down to the Hall-B beam dump. The vacuum box also helped minimize multiple scattering of the scattered electrons en route to the detectors. A photograph of the vacuum chamber is shown in Fig. 16.

Figure 16: A photograph of the $\sim$5 m long, two stage vacuum chamber used during the PRad experiment (left, please disregard the date on the photograph). A photograph of the 1.7 m diameter thin window at one end of the vacuum chamber (right). Here the GEM and HyCal have been moved downstream for technical service.

4.3 GEM detectors

The PRad experiment used Gas Electron Multiplier (GEM) based coordinate detectors, they consisted of a pair of large area 1.2 m$\times$ 0.6 m three layer ionization chambers, with $\sim$ 100 μm position resolution. The chambers were designed and constructed by the University of Virginia group and are currently the largest such chambers to be used in a nuclear physics experiment. These GEM chambers provided more than a factor of 20 improvement in coordinate resolution and a similar improvement in the Q^2 resolution. They allowed unbiased coordinate reconstruction of hits on the calorimeter, including the transition region of the HyCal calorimeter. The GEM detectors also allowed us to use the lower resolution Pb-glass part of the calorimeter, extending the total Q^2 range covered at a single beam energy setting.

The chambers were mounted to the front face of the HyCal calorimeter using a custom mounting frame. Each chambers had a 2-inch hole to allow the beam pipe to pass through the chambers. A pre-mixed gas of 70% Argon and 30% CO_2 was continuously supplied to the chambers. Photographs of the GEM detectors is shown in Fig. 17.

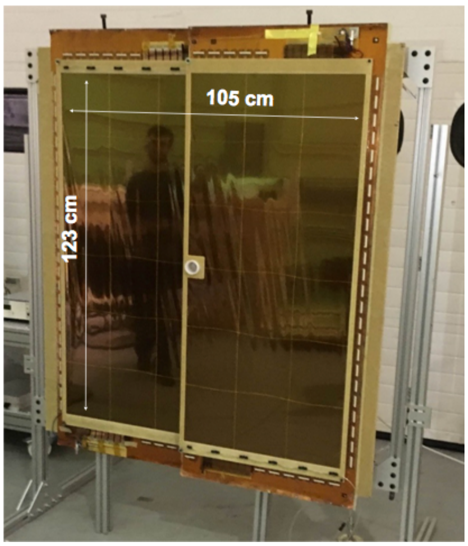

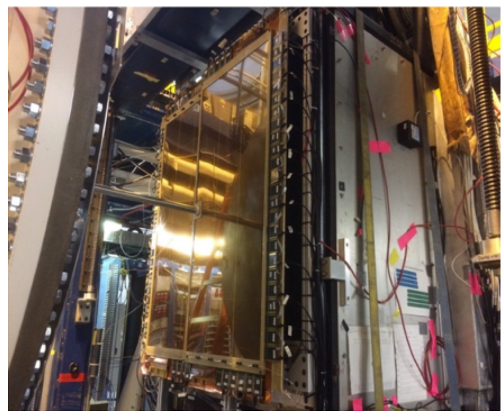

Figure 17: A GEM based coordinate detector used in the PRad experiment (left). A photograph of the GEM chambers mounted to the front of the HyCal calorimeter (right). Here the GEM and HyCal have been moved downstream for technical service.

The PRad GEM detectors were read out using the APV25 chip based Scalable Readout System (SRS) developed at CERN by the RD51 collaboration. The APV25 chip samples 128 channels in parallel at 20 MHz or 40 MHz and stores 192 analog samples, each covering 50 ns or 25 ns, per channel. Following a trigger, up to 30 consecutive samples from the buffer are read-out and transmitted to an ADC unit that de-multiplexes the data from the 128 channels and digitizes the analog information.

The SRS system consists of the following components:

- SRS-APV25 hybrid cards mounted on the detector. These cards contain the 128 channel APV25 chip which reads data from the detector, multiplexes the data, and transmits analog to the ADC card via standard commercial HDMI cables.
- SRS-ADC unit that houses the ADC chips that de-multiplex data and convert into digital format.
- SRS-FEC card which handles the clock and trigger synchronization. A single Front End Card (FEC) and ADC card combination has the capability to read data from up to 16 APV hybrid cards. The data

from the FEC are send either directly to the data acquisition computer (DAQ PC) or to the SRS-SRU via a 10 Gb/sec fiber link.

- SRS-SRU, Scalable Readout Unit, handles communication between multiple (up to 40) FEC cards and the data acquisition computer. It also distributes the clock and trigger synchronization to the FEC cards.
- The data acquisition computer was used as a readout controller and as a part of the larger PRad-DAQ system.

A total of 9216 electronics channels are needed to readout the PRad GEM chambers. This amounts to 72 SRS-APV25 cards (128 channels per card). The SRS-ADC / SRS-FEC card can handle up to 16 SRS-APV25 cards and send data to the SRS-SRU through a newly implemented 10Gb Fiber link. We use 6 SRS-ADC/SRS-FEC cards to read out all 72 SRS-APV25 cards limiting the number of SRS-APV25 card per SRS-FEC to 12. The SRS-FECs cards are connected to 2 SRS-SRU boards (3 SRS-FECs per SRS-SRU). An upgraded firmware allowed the experiment to collect data at $\sim$ 5kHz with a data rate of $\sim$ 400 MB/sec and $\sim$ 90% live time. This was the highest DAQ rate achieved by a APV based system. A schematic of the GEM DAQ system is shown in Fig. 18.

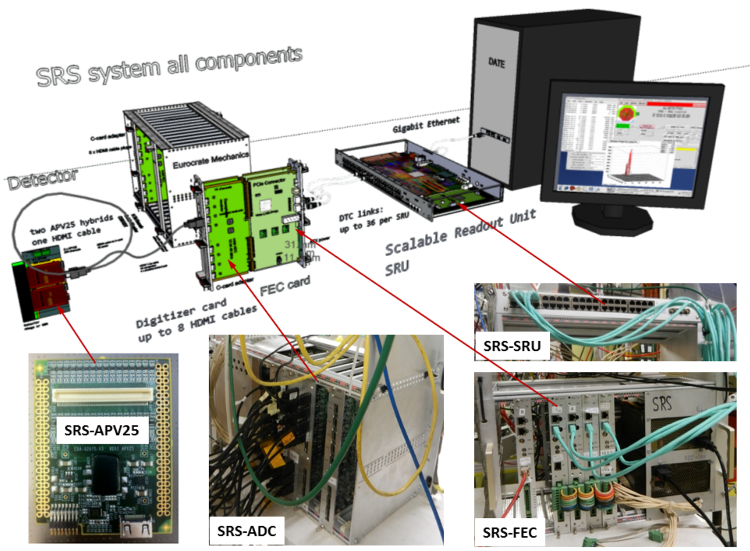

Figure 18: A schematic of the PRad GEM DAQ system.

The PRad GEM based coordinate detector consistently performed well throughout the experiment. The efficiency of the chamber was uniform over the entire chamber as shown in Fig. 19, and it achieved the design resolution of 72 μm, as shown in Fig. 30. A further optimization on the spacers which related to the systematic uncertainty will be discuss in Sec.9.2.2. The performance of the detector remained stable throughout the experiment.

4.4 HyCal electromagnetic calorimeter

The PrimEx Collaboration at JLab, using a previous MRI award constructed a novel state-of-the-art multi-channel electromagnetic hybrid ($PbWO_4$-lead glass) calorimeter (HyCal) [38] to perform a high precision measurement of the neutral pion lifetime via the Primakoff effect [39]. The PRad experiment used the high

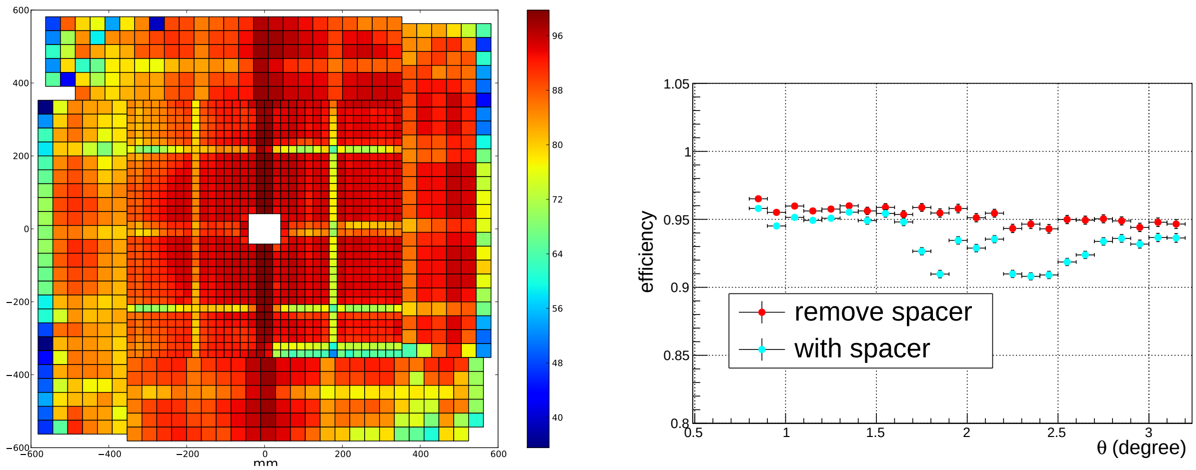

Figure 19: A plot of the GEM efficiency over the X-Y coordinates of the detector (left), and the GEM efficiency over the region overlapping with the $PbWO_4$ crystals of the HyCal calorimeter *vs.* polar angle (right). The drops in efficiency seen in the 2D plot in the left is due to spacers inside the GEM modules. A software cut to remove the spacers yields an efficiency profile uniform to within +/- 1% level as seen by red circles. The cut to remove spacers reduce the available statistics by only about 4.7%.

resolution and large acceptance PrimeEx HyCal electromagnetic calorimeter to detect the scattered electrons from ep and Møller scatterings with high precision.

A single $PbWO_4$ module is 2.05×2.05 cm^2 in cross sectional area and 18.0 cm in length ($20X_0$). The crystal part of the calorimeter consists of 1152 modules arranged in a 34×34 square matrix (70×70 cm^2 in size) with four crystal detectors removed from the central part (4.1×4.1 cm^2 in size) for passage of the incident electron beam. The scintillation light from the electromagnetic shower in the crystals was detected with Hamamatsu R4125HA photomultiplier tubes (PMT) coupled at the back of the crystals with optical grease. Each module is supplied with high voltage and is equipped with readout of dynode and anode signals. Each crystal was first wrapped in $\sim$ 63 μm VM-2000 reflector (from 3M company), then with a 38.1 μm black Tedlar for optical isolation between the blocks. The PMT housings were attached to the crystals with two specially designed brass flanges on the front and back of the crystals, stretched with two 25 μm brass strips. In addition, a LED based light monitoring system is used to deliver a pulse of light to each module via a fiber optic cable. Figure 20 shows the assembled PrimEx HyCal calorimeter before the final installation of the gain monitoring system. The calorimeter will be located at a distance of about 5.7 m from the target which will provide a geometrical acceptance of about 25 msr.

The energy calibration of HyCal was performed by continuously irradiating the calorimeter with the Hall B tagged photon beam at low intensity ($<$ 100 pA). An excellent energy resolution of $\sigma_E/E = 2.6\%/\sqrt{E}$ has been achieved by using a Gaussian fit of the line-shape obtained from the 6×6 array. After subtraction of the beam energy spread due to the finite size of the scintillating fiber, as well as multiple scattering effects in vacuum windows and in air, a level of 1.2% energy resolution was reached for 4 GeV electrons. The impact coordinates of the electrons and photons incident on the crystal array were determined from the energy deposition of the electromagnetic shower in several neighboring counters. Taking into account the photon beam spot size at the calorimeter (σ=3.0 mm), the overall position resolution reached was $\sigma_{x,y} = 2.5 \text{ mm}/\sqrt{E}$ for the crystal part of the calorimeter. The calorimeter performed as designed during the experiment, as shown in Fig. 21, which shows the resolution achieved during the PRad experiment and the energy dependence of the trigger efficiency.

As the light yield of the crystal is highly temperature dependent ($\sim$ 2%/°C at room temperature), a

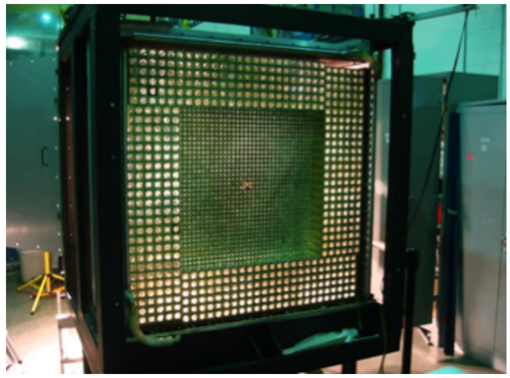

Figure 20: The PrimEx HyCal calorimeter which was developed by the PrimEx collaboration using a previous MRI award shown with all modules of the high performance $PbWO_4$ crystals in place and before installation of the gain monitoring system in front of the calorimeter.

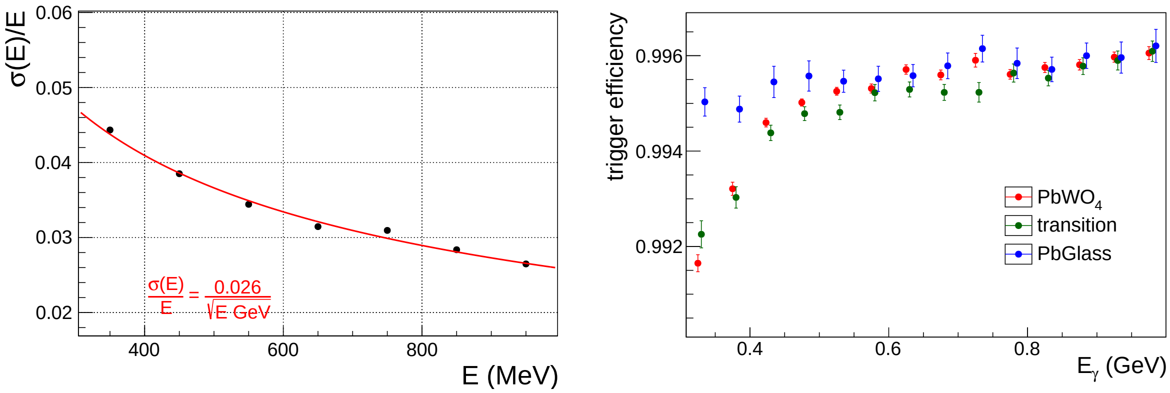

Figure 21: Energy resolution of the $PbWO_4$ crystal part of the HyCal calorimeter (left) and the energy dependence of the trigger efficiency (right). These data are from the PRad experiment.

special frame was developed and constructed to maintain constant temperature inside of the calorimeter with a high temperature stability (± 0.1°C) during the experiments. The trigger in this experiment (total energy deposited in the calorimeter $\geq$ 20% of E_0) allowed for the detection of the Møller events in both single-arm and double-arm modes.

4.5 Summary

The PRad experiment successfully demonstrated the technique of magnetic spectrometer free measurement of ep scattering at small angles using a windowless gas flow target, A GEM detector and a high resolution calorimeter. This technique let the PRad experiment achieve the lowest Q^2 (2.0×10^{-4} GeV^2) of any ep scattering experiment and at the same time cover large range in Q^2 (10^{-4} - 6×10^{-2} GeV^2). It also demonstrated the effectiveness of using the simultaneous detection of Møller and elastic scattering to reduce the systematic uncertainties.

5 Proposed Experimental Setup

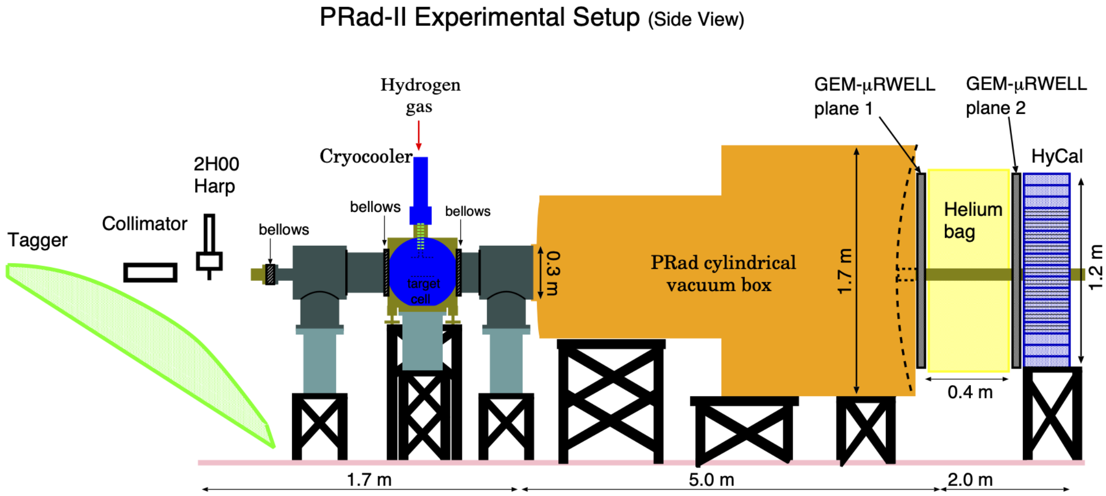

Figure 22: A schematic of the setup for the proposed experiment.

The proposed experiment will reuse the PRad setup with several major changes to adapt it for measuring elastic ed scattering. It will use the PRad windowless gas flow target, with a new target cell redesigned to hold a cylindrical Si-strip recoil detector inside the cell. The large volume vacuum chamber with a single thin window will be reused and the high resolution HyCal calorimeter will be ugraded to a all $PbWO_4$ calorimeter with a fADC based readout. Two planes of GEM chambers separated by 40 cm will be located in front of HyCal. A schematic of the experimental setup is shown in Fig. 22 and the unique elements are described in the subsections below.

5.1 Electron beam

We propose to use the CEBAF beam at two incident beam energies E_0 = 1.1 and 2.2 GeV for this experiment. The beam requirements are listed in Table 2. All of these requirements were achieved during the PRad experiment. A typical beam profile during the PRad experiment is shown in Fig. 23 and the beam X, Y position stability of $\simeq \pm$ 0.1 mm is shown in Fig. 24.

Table 2: Beam parameters for the proposed experiment

Energy (GeV)	current (nA)	polarization (%)	size (mm)	position stability (mm)	beam halo
1.1	30	Non	< 0.1	≤ 0.2	$\sim 10^{-7}$
2.2	70	Non	< 0.1	≤ 0.2	$\sim 10^{-7}$

5.2 Windowless gas flow target

We will use the windowless gas flow target developed for the PRad experiment. A new target cell will be built such that it can accommodate the Si-strip recoil detector inside it. The target cell will be made out copper and will have dimensions of 30×30×5.5 cm^3. It will have thin (7 μm) Kapton foils on the sides

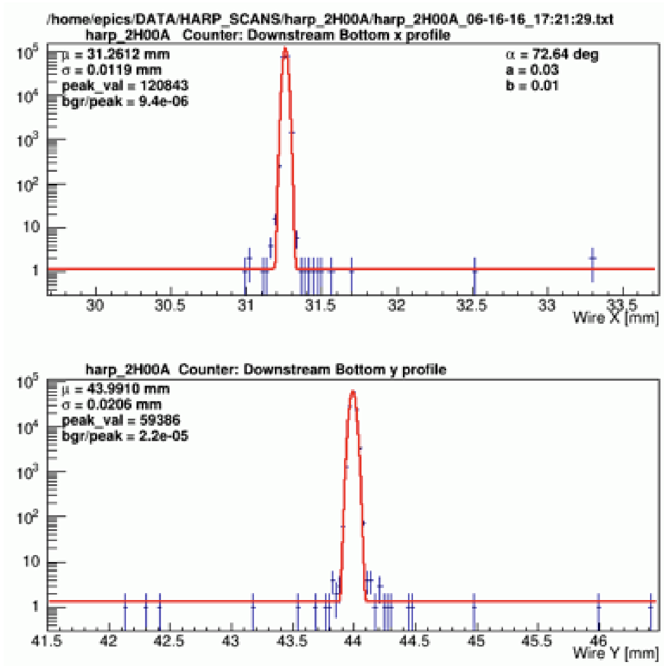

Figure 23: Typical beam profile during the PRad experiment, showing a beam size of $\sigma_x = 0.01$ mm and $\sigma_y = 0.02$ mm.

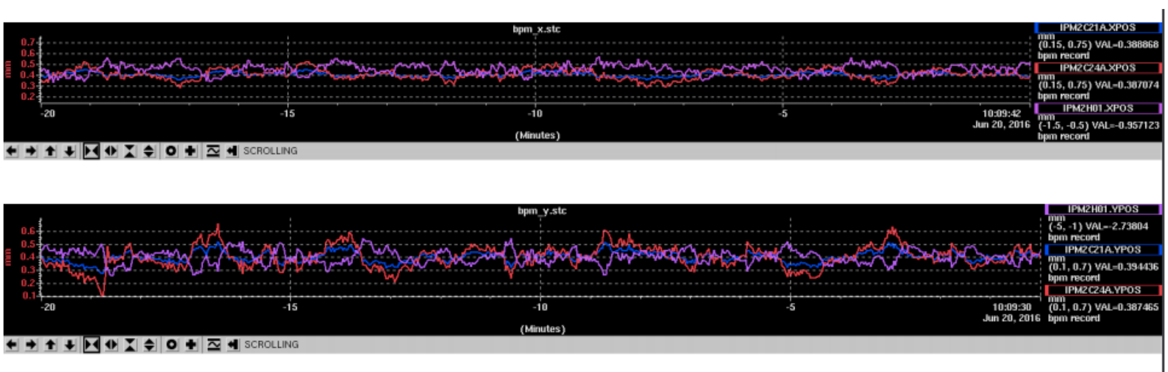

Figure 24: Beam X,Y position stability ($\simeq \pm$ 0.1 mm) during the PRad experiment.

facing the beam with a 4 mm aperture in the center for the beam to pass through. The front and back faces of the target cell will have 20 feedthroughs for the readout electronics of the Si-strip detector.The gas inlet is also modified compared to the cell used in the PRad experiment. It will inject the gas from the top edge of the front and back faces rather than from the top of the cell. Room temperature deuterium gas will be flown through a 25 K heat exchanger attached to a mechanical cryocooler, and accumulated in the copper target cell located within a small (< 1 m^3) differentially pumped vacuum chamber. The target cell will be suspended from the top of the vacuum chamber using a precision, 5-axis motion mechanism. The gas will be pumped out of the chamber using two large turbo molecular vacuum pumps with a combined pumping speed of 5700 l/s. The gas pressure within the cell will be measured by a precision capacitance manometer and is expected to be approximately 0.5 torr during the experiment, giving in an areal density of about 2×10^{18} D/cm^2. Two additional turbo pumps attached to the upstream and downstream ends of the vacuum chamber will help maintain a beamline vacuum of less than 10^{-5} torr. The gas will be metered into the target system using a precision, room-temperature mass flow controller. In order to reduce the systematic uncertainty, a further optimization on the design of the target cell will be discuss in Sec.9.2.6.

5.3 Cylindrical recoil detector

The design of the recoil detector is based on the CLAS12 Barrel Silicon Tracker (BST) [40, 41]. We will enclosed a cylindrical recoil detector within the target cell. It will consist of 20 panels of twin single sided silicon strip detectors. Each panel will be 52 mm long and 42 mm wide arranged as a do-decagon, as shown in Fig. 25. Each panel will consist of a thin, 200 μm sensor and a thick, 300 μm sensor. Each sensor will consist of 256 strips with linearly varying angles of 0° - 3°. This graded angle design minimizes dead zones. The strips will have a constant ϕ pitch of $\sim$ 200 μm ($\sim$1/85°). Fig. 26 shows the strips on the thin inner sensor and the thick outer sensor and also the intersection pattern. This detector will have angular resolution of $\delta\phi \leq 5$ mrad and $\delta\theta \leq$ 10-20 mrad.

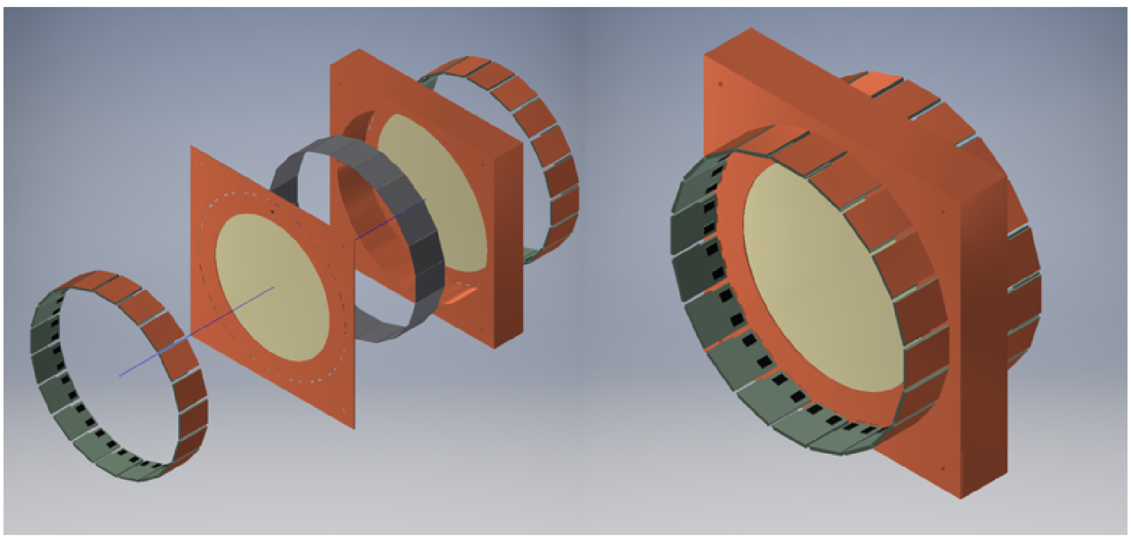

Figure 25: A schematic of the cylindrical recoil detector consisting of 20 silicon strip detector modules, held inside the target cell. All solids are shown as transparent for ease of viewing.

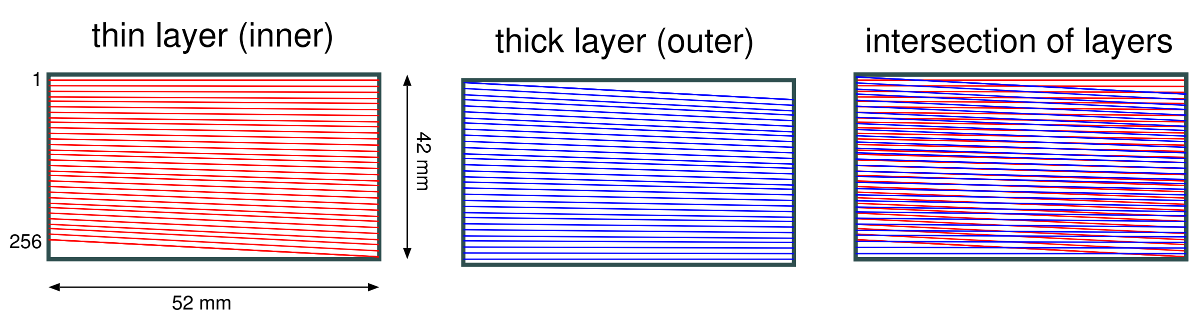

Figure 26: The layout of strips on each side of the sensors and their intersection pattern.

In order to minimize multiple scattering, essential for low momentum tracking, the materials budget will be reduced to <1% radiation length. The sensors will be mounted on a composite backing structure consisting of Rohacell 71 core , bus cable and a carbon fiber skin made from K132C2U fibers oriented in a quasi-isotropic pattern. The bus cable is made from a Kapton sheet with 3μm thick copper traces, which are

0.5 mm wide that provide the high voltage to the sensor on one side while the other side forms the grounding plane for the carbon fiber. The sensors are very similar to the ones used in the BST. The different layers of each detector module is shown in Fig. 27.

The readout system is identical to the one used by the BST in CLAS12 and we expect to use electronics from the spare planes of the BST. The readout is build on FSSR2 ASIC developed and Fermilab and fabricated by Taiwan Semiconductor Manufacturing Company. Each channel of 128 input channel of the FSSR2 chip has a preamplifier, a shaper with adjustable shaping time (50 - 125 ns), a baseline restorer, and a 3-bit ADC. The signals will be read out on the opposite side for each layer using a pitch adapter which matches the 156 μm sensor readout pitch to the 50μm bonding pad pitch of the FSSR2 chips. The signals will be read using a single rigid-flex Hybrid Flex Circuit Board (HFCB) developed at JLab for the BST. The HFCB hosts four FSSR2 chips, two on the top and two on the bottom side. Data is transferred via a flex cable to the level one connect (L1C) board. The L1C has two high density Nanonics connectors for data and control lines, Molex Micro-Fit 9-pin connector for high voltage ($\sim$ 85 V) bias to the sensors, and AMP Mini CT 17 pin connector for low voltage (2.5 V) power to the ASICs. There are 12 layers in rigid part and 6 layers in flex part. Control, data, and clock signals do not cross the ground plane splits. Clock signals are located on a separate layer. Guard traces are routed between output, clock, and power lines. Separate planes are provided for analog and digital power. To reduce noise on these planes, regulators and bypass capacitors are added. High voltage filter circuits and the bridging of high and low voltage return lines are located close to the ASICs.

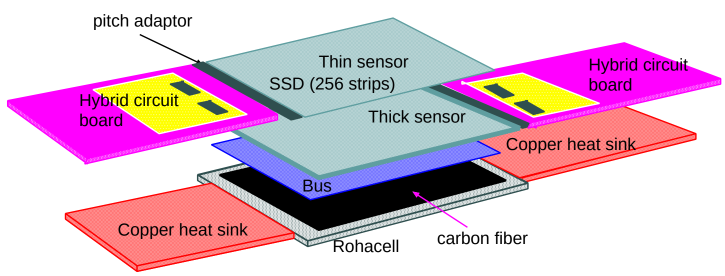

Figure 27: A schematic of the different layers of each detector module.

The period of the clock called beam crossing oscillator (BCO) sets the data acquisition time. If a hit is detected in one of the channels, the core logic transmits pulse amplitude, channel number, and time stamp information to the data output interface. The data output interface accepts data transmitted by the core, serializes it, and transmits it to the data acquisition system. To send the 24-bit readout words one, two, four, or six Low Voltage Differential Signal (LVDS) serial data lines can be used. Both edges of the 70 MHz readout clock are used to clock data, resulting in a maximum output data rate of 840 Mb/s. The readout clock is independent of the acquisition clock. Power consumption is $\leq$ 4 mW per channel. The FSSR2 is radiation hard up to 5 Mrad.

Each of the four FSSR2 ASICs reads out 128 channels of analog signals, digitizes and transmits them to a

VXS-Segment-Collector-Module (VSCM) card developed at Jefferson Lab. The event builder of the VSCM uses the BCO clock timestamp from the data word of each FSSR2 ASIC and matches it to the timestamp of the global system clock, given by the experiment trigger. The event builder buffers data received from all FSSR2 ASICs for a programmable latency time up to $\sim 16\ \mu$ s. The VSCM is set up to extract event data within a programmable lookback window of $\sim 16\ \mu$ s relative to the received trigger.

5.3.1 Calibration of the Si strip recoil detector

We plan to use the deuteron and proton beams from the Tandem accelerator at TUNL to measure the detector efficiency for deuterons with kinetic energy in the 1 - 15 MeV range and protons with kinetic energy of 1 - 25 MeV. These measurements will be used to form a ratio of the proton to deuteron detection efficiency as a function of energy. During the experiment each $e-D$ run will be interspersed with periodic $e-p$ runs. The $e-p$ runs will be used to monitor the proton detection efficiency of the recoil detector given the over-determined kinematics of $e-p$ scattering. The measured proton detection efficiency along with the ratio of the proton to deuteron detection efficiency measured at TUNL will be used to determine the deuteron detection efficiency. In addition a α-source based system will be used monitor the time dependence of the efficiency.

As mentioned before the Si strip recoil detector is based on the Hall-B SVT detector. As a first step to demonstrate the feasibility of this scheme for determining the detector efficiency we had made plans to perform a test using a single SVT module from Hall-B along with proton and deuteron beams at TUNL to characterize the energy dependence of the detector efficiency. We will use Rutherford back scattering of protons and deuterons from a Au foil target to perform these tests. A schematic of the test built around an existing vacuum chamber at TUNL is shown in Fig. 28. A Faraday cup will be used as a beam stop and

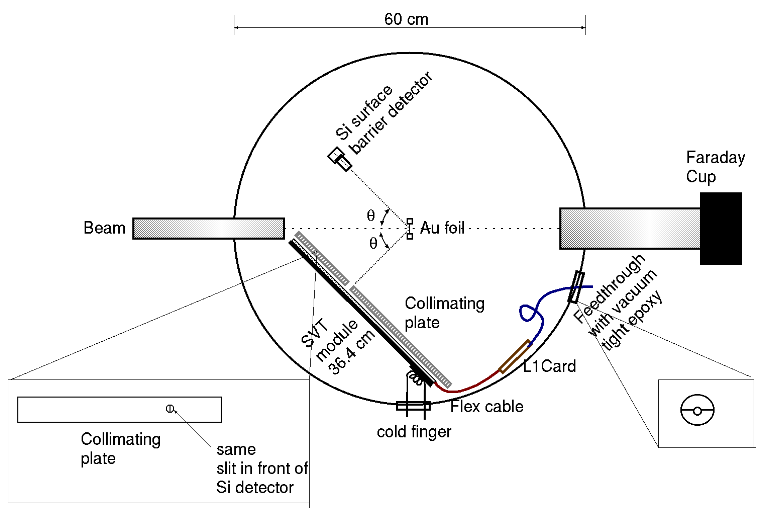

Figure 28: Schematic of one SVT module housed inside the TUNL scattering chamber for the detector test.

to measure the beam intensity with 0.5% precision. The SVT module will be read out using a single JLab VSCM card operated in a VXS crate (to be borrowed from Hall-B).

The SVT module will be attached to a collimating plate using the 3 mounting holes on the SVT module as shown in Fig 28, the detector and plate together will be attached to the rails on the floor of the chamber and located on the right of the beam. Angles are marked for every 0.1 degrees on the floor of the chamber. These marking and the rails will be used to allign the slit on the collimator plate to the desired angle. The collimating plate will block all the scattered protons and deuterons, allowing only particles that pass through a small slit located at large scattering angles (> 135 degrees) with respect to the beam direction (see left inset of Fig. 28. A Si surface barrier detector will be placed at a symmetric angle on the left of the beam along with a collimator and an identical slit, these type of detectors already mounted in the chamber are shown in Fig. 29(c). The surface barrier detector will be used to measure the relative detector efficiency.

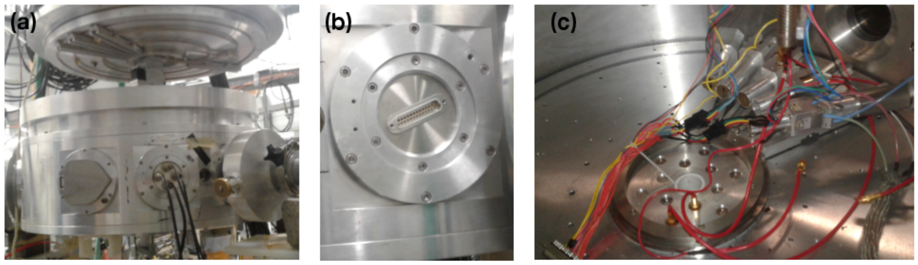

Figure 29: (a)The TUNL vacuum chamber showing one of the electrically isolated feedthrough ports. (b)Close up view of a feedthrough showing the 3-inch Al. disk which must be adapted for any custom feedthrough. (c) The inside floor of the vacuum chamber showing the Si surface barrier detectors with collimators and slits in front of the detector.

At a given beam energy (E) and beam current (I) the ratio of the detector hits normalized to the beam intensity in the strips of the SVT module ($N_{SVT}(I, E)$) exposed to the protons/deuterons to the detector hits also normalized to the beam intensity in the surface barrier detector ($N_{Si}(I, E)$) will be a measure of the rel ative efficiency, $\eta(I, E)$, of the exposed region of the SVT module (see Eq. 14). A higher precision measurement would be possible if the surface barrier detector is read out using a fADC such that one can form coincidences offline. In such a setup a CH_2 target would be preferable to enable pp and dp elastic scattering with the two detectors set at 90° to the beam. We envision performing such a test as a follow-up to this planned test.

$$\eta(I, E) = \frac{N_{SVT}(I, E)}{N_{Si}(I, E)} \tag{14}$$

The beam energy will be varied from 1 - 20 MeV in order to obtain the energy dependence of the detector efficiency. The angle of the surface barrier detector and the corresponding location of the slit on the collimator plate in front of the SVT can be varied to measure the efficiency at multiple locations on the SVT. A 6 MeV proton can pass though the 300 μm thick Si sensor of the SVT module [42], and the energy loss (dE/dx) of protons for 6-20 MeV protons will be large which implies that the signal size from the SVT sensor should be large. It should be relatively easy to detect these signals, For 1-6 MeV protons the signal size will be proportionally smaller but should still be detectable. We expect to make a sub-percent measurement with this setup.

The measurement had been scheduled for May, 2020 however the COVID-19 pandemic has forced us to postpone these measurements to a future date.

5.4 Two Planes of GEM detectors

The pair of GEM detectors used during the PRad experiment performed very well during the entire experiment yielding highly stable operation, high resolution and high efficiency, as highlighted in Fig. 30.

The experience from the PRad experiment showed that having two GEM detector layers will provide high precision track parameters for diagnostics and systematic checks of the experimental setup. Furthermore, the requirement of at least one out of two GEM layer hits for production data yields a GEM hit efficiency of close to 100% throughout the active area of the experiment. The two GEM layers in the proposed experiment will be separated by 40 cm. The new μRWELL based tracking layers will have an identical size and outer design to the PRad GEM detectors. However, new advances in μRWELL detector technology such as spacer-free construction with a smaller materials budget will be incorporated into the new detectors. The biggest advantage of using this new technology for the second tracking layer is that it would allow each detector module to be built without a spacer grid. The presence of the spacer grid in the original GEM detector caused narrow regions of lower efficiency along the spacers. While these efficiencies were measured relative to HyCal and corrected in data analysis, they contributed to the systematic uncertainty of PRad. Having spacer-less detectors as the new tracking plane will eliminate the regions of low efficiency in this new detector. Furthermore, having this spacer-less layer would allow for highly accurate determination of efficiency profile of the original GEM layer. The impact of using two advanced technology coordinate detector layers on the determination of inefficiency profile and the associated uncertainty, as well as the improvement in the vertex reconstruction capabilities was studied using a simulation of the GEM detectors. The improvement in the determination of the efficiency and its uncertainty is shown in Fig. 31. In addition the improvement in the resolution of the reconstructed reaction vertex is shown in Fig. 32.

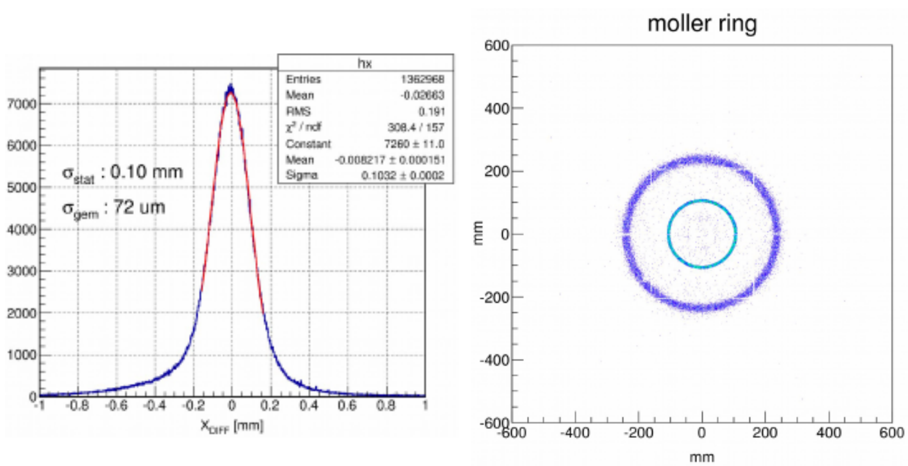

Figure 30: (Left) The position resolution (approximately 72 μm) for GEM detectors achieved during PRad experiment; this represents a factor of 20-40 improvement over the resolution available without the GEM tracker in the setup. (Right) The scattered Møller *ee* pair rings detected by PRad GEM tracker illustrating the high position resolution and accuracy provided by the GEMs. Furthermore, this plot shows the very low background level in the reconstructed GEM hit locations.

The readout of the two GEM μRWELL layers requires approximately 20 k electronic channels. This readout for the proposed experiment will be done by using the high-bandwidth optical link based MPD readout system recently developed for the SBS program in Hall A. This system is currently under rigorous resting. This new system uses the APV-25 chip used in the PRad GEM readout. However, the readout of the digitized data is performed over a high-bandwidth optical link to a Sub-System Processor (SSP) unit in a CODA DAQ setup. Given its 40 MHz sampling rate and the number of multiplexing channels, the limiting trigger rate for the APV chip is 280 KHz in theory. In practice we expect it to be lower and assume a 100 KHz limit. Currently tests are underway by the Jlab electronics group in collaboration with the UVa group to test the SBS GEM readout system to this high trigger rate limit. Given the aggressive R&P program currently in place to reach this goal we do not anticipate any difficulty of reaching the 25 kHz trigger rate assumed for the DRad experiment.

The option for an even faster GEM readout system is now available with the current ongoing work as the pre R&D program for Jefferson Lab Hall A SoLID project. This fast GEM readout system is based on the new VMM chip was developed at BNL for the ATLAS large Micromegas Muon Chamber Upgrade. VMM

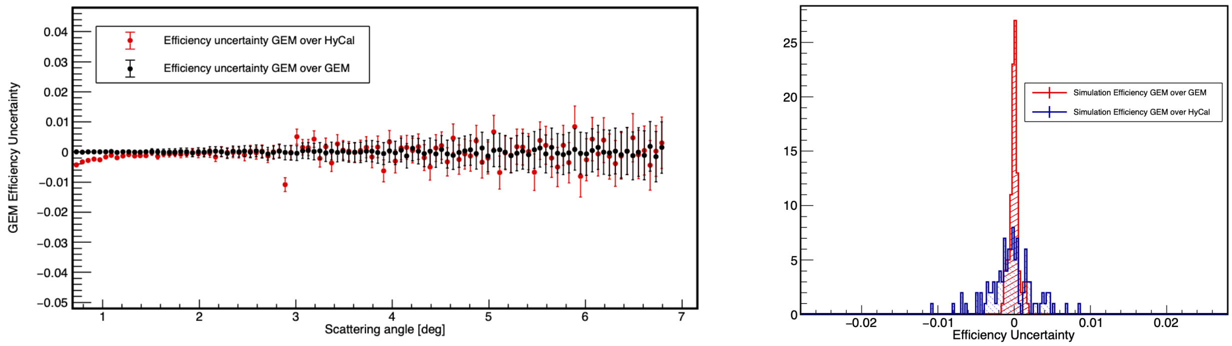

Figure 31: (left) Simulated GEM efficiency uncertainty as a function of scattering angle, when using a single GEM detector plane along with the HyCal compared to when using two spacer-less GEM μRWELL detector planes. (right) The uncertainty in determining the efficiency for single GEMμRWELL vs two GEM μRWELL detector planes.

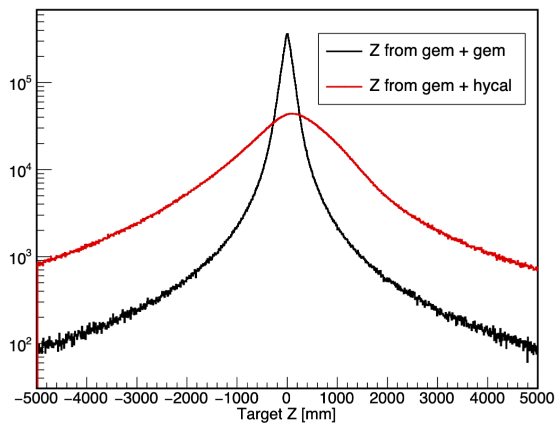

Figure 32: Reconstructed reaction z-vertex when using one GEM plane along with the HyCal vs using two GEM μRWELL detector planes.

chip is an excellent candidate for large area Micro Pattern Gaseous Detectors such as GEM and μRWELL detectors. The VMM is a rad-hard chip with 64 channels with an embedded ADC for each channel. This chip is especially suited for high rate applications and is much more advanced than the 25 year old APV chip. The VMM has an adjustable shaping time which can be set to be as low as 25 ns. In the standard (slower) readout mode, the ADC provides 10-bit resolution, while in the faster, direct readout mode the ADC resolution is limited to 6-bits. The fast direct readout mode has a very short circuit reset time of less than 200 ns following processing of a signal. The VMM chip has already been adapted by the CERN RD-51 collaboration for Micro-Pattern Gas Detectors to replace the APV-25 chip. The electronics working group of the RD-51 collaboration has already created a new version of its Scalable Readout System (SRS) based on the VMM chip. The UVa group, which has extensive expertise operating the APV based SRS readout, recently acquired a 500 channel VMM-SRS system and is testing it in collaboration with the Jlab DAQ group. Furthermore, the as part of the SoLID pre R&D program the UVa electronics group is now developing a GEM readout system capable of running at 300 kHz based on the VMM chip.

The 170 k channel APV based GEM readout for SBS is already acquired and built while as part of the SoLID project a 200+ k channel VMM based readout system will be assembled. Given these very large volume fast readout systems, we do not see any problem acquiring the 20 k channel GEM readout system needed for DRad.

5.5 HyCal calorimeter

The PrimEx HyCal high resolution and large acceptance electromagnetic calorimeter will be used in this experiment. It will be used to detect the scattered electrons from ed elastic and Møller scattering with high precision. For PRad-II and the DRad experiment we are proposing to replace the outer Pb-glass layer with $PbWO_4$modules turning the calorimeter into a fully $PbWO_4$calorimeter.

As described previously in Sec. 4.4, a single $PbWO_4$ module is 2.05×2.05 cm^2 in cross sectional area and 18.0 cm in length ($20X_0$). The crystal part of the calorimeter consists of 1152 modules arranged in a 34×34 square matrix (70×70 cm^2 in size) with four crystal detectors removed from the central part (4.1×4.1 cm^2 in size) for passage of the incident electron beam. The scintillation light from the electromagnetic shower in the crystals was detected with Hamamatsu R4125HA photomultiplier tubes (PMT) coupled at the back of the crystals with optical grease. Each module is supplied with high voltage and is equipped with readout of dynode and anode signals. Each crystal was first wrapped in $\sim$ 63 μm VM-2000 reflector (from 3M company), then with a 38.1 μm black Tedlar for optical isolation between the blocks. The PMT housings were attached to the crystals with two specially designed brass flanges on the front and back of the crystals, stretched with two 25 μm brass strips. In addition, a LED based light monitoring system is used to deliver a pulse of light to each module via a fiber optic cable. The calorimeter will be located at a distance of about 5.5 m from the target which will provide a geometrical acceptance of about 25 msr. The energy calibration of HyCal will be performed by continuously irradiating the calorimeter with the Hall B tagged photon beam at lowest intensity.

As the light yield of the crystal is highly temperature dependent ($\sim$ 2%/°C at room temperature), a special frame was developed and constructed to maintain constant temperature inside of the calorimeter with a high temperature stability ($\pm 0.1^\circ$C) during the experiments.

5.6 Electronics and Trigger

The proposed experiment will read out about 2500 channels of charge and timing information coming from the high resolution calorimeter. These signals will be read out using the JLab designed and built flash-ADC modules (FADC250) that each can read 16 channels. The DAQ system for the calorimeter is thus composed of 160 FADC250 modules that can be placed in about ten 16-slots VXS crates. The major advantages of the flash-ADC based readout are the simultaneous pedestal measurement (or full waveform in the data stream), sub-nanosecond timing resolution, fast readout speed, and the pipeline mode that allows more sophisticated triggering algorithms such as cluster finding. With this electronics the veto counter will not be needed to be installed in front of the HyCal. The timing information will be used for the time-of-flight between the recoil detector and the HyCal calorimeter in the experiment. The fADCs should allow a time-of-flight resolution of 0.5 ns, but, we have assumed a conservative estimate of 1 ns in our simulations described in Sec. 6.

The two GEM and μRWELL coordinate detector planes will be readout using the custom APV-25 cards similar to those used in PRad and a dedicated PCI based CODA DAQ system that was developed for the PRad experiment. Additionally, some VME scalers will read out and periodically inserted into the data stream.

The DAQ system for the proposed experiment is the standard JLab CODA based system utilizing the JLab designed Trigger Supervisor. A big advantage of the CODA/Trigger Supervisor system is the ability to run in fully buffered mode. In this mode, events are buffered in the digitization modules themselves allowing the modules to be "*live*" while being readout. This significantly decreases the deadtime of the experiment. With the upgraded flash-ADC modules we expect to reach the data-taking rate of about 20,000 events per second, which is about 4 times higher than the data-taking rate in PRad experiment. Such a capability of the DAQ system has already been demonstrated by CLAS12 experiments.

A large fraction of the electronics needed for the DRad DAQ and trigger, including the high voltage crates and all necessary cabling for the detectors, are available in Hall B from the PRad experiment. The readout electronics and DAQ for the first pair of GEM chambers and HyCal calorimeter will be exactly same as what was used during the PRad experiment. For the recoil detector readout electronics we plan to use the electronics borrowed from the spare Hall-B SVT detector plane as discussed in Sec. 5.3. The electronics for the new plane of GEM chamber will have to be procured as discussed in Sec. 5.4.

The trigger in this experiment will be set to the total energy deposited in the calorimeter $\geq 20\%$ of E_0. This will allow for the detection of the Møller events in both single-arm and double-arm modes.

We estimate (see Sec. 9) the $ed \rightarrow ed$ rate to be about 200 Hz, the Møller rate to be about 400 Hz and the deuteron electro-disintegration rate to be about 500 Hz. This give a total physics trigger rate of $\sim$1.1 kHz. Given that the energy threshold for the calorimeter will be set to $\geq 20\%$ of E_0, the total trigger rate for the proposed experiment is expected to be at the level of 4 kHz. The PRad DAQ was easily able to handle rates up to $\sim$ 5 kHz and hence the exptected rate is well within the capabilities of the DAQ.

6 Kinematics, Experimental Resolutions and Backgrounds

6.1 Kinematics

Two main processes considered in this proposal, $ed \to ed$ scattering and Møller scattering $e^-e^- \to e^-e^-$ are both two-body reactions. Therefore, a minimum of two kinematical variables are required for the kinematical reconstruction of the reaction. Measuring more than two variables in the experiment will allow to select elastic events from competing physics processes and accidental background.

In this experiment the energy and momentum of the incident electron beam are known with high precision ($\Delta E/E \sim 10^{-4}$, emittance $\epsilon \sim 10^{-3}$ mm-mrad). Since the deuteron is a rather loosely bound nucleus (binding energy ~ 2.2 MeV) in order to insure the elasticity in the measured $ed \to ed$ events, in addition to detection of the scattered electron, we propose to detect the recoiling nucleus in a newly designed cylindrical recoil detector (see section 5.3). Just as in the PRad experiment, the energy and the (x, y) positions of the forward scattered electrons will be measured by the HyCal calorimeter and the GEM chamber attached to the front face of the calorimeter (see section 5.5 and 5.4). The timing information from the fADC based readout of the HyCal calorimeter will fix the arrival time of the scattered electrons to the front of the HyCal calorimeter. We also propose to add a second GEM based position detector located 40 cm in front of the GEM detector attached to the face of HyCal. This will allow not only to improve the position resolution of HyCal by factor of ~ 20 but, it will also significantly improve the reaction vertex reconstruction compared to the PRad experiment. The main requirement to the recoil detector is to measure the time and the azimuthal angle of elastic scattered deuteron and protons from background processes. Both scattered electrons from the Møller events will be detected in the calorimeter with measurement of the energies (E_1, E_2) and the (x, y) positions. In addition, the positions of these electrons will be measured in two GEM detectors with high precision. The incident beam energies and the range of Q^2 together with the electron scattering angle coverage are listed in table 3.

Table 3: Proposed kinematics for the deuteron charge radius measurement with the HyCal calorimeter at 5.6 m from target.

E_{beam} (GeV)	θ_e (deg)	Q^2 $(\text{GeV/c})^2$
1.1	0.7	$1.8 \cdot 10^{-4}$
	6.0	$1.3 \cdot 10^{-2}$
2.2	0.7	$7.2 \cdot 10^{-4}$
	6.0	$5.3 \cdot 10^{-2}$

6.1.1 Kinematics of ed scattering

Since target mass in the $ed \to ed$ elastic scattering process is much larger than the electron mass the forward scattered electron carries most part of the incident beam energy, leading to a virtual photon of only few MeVs (figure 33). For the same reason the recoiling deuteron polar angle is very close to 90 degrees with kinetic energies of a few to ten MeV scale (figures 34 and 35). To extend the Q^2 range and have some overlap between the experimental data sets we plan to run this experiment for two incident electron beam energies, $E_0 = 1.1$ and 2.2 GeV ((figure 36). The choice of calorimetric method, allows detection of smaller scattering angles, and the two incident beam energies allows coverage of a large Q^2 range (from extreme low $1.8 \cdot 10^{-4}$ to $5.3 \cdot 10^{-2}$) in a single experimental setting.

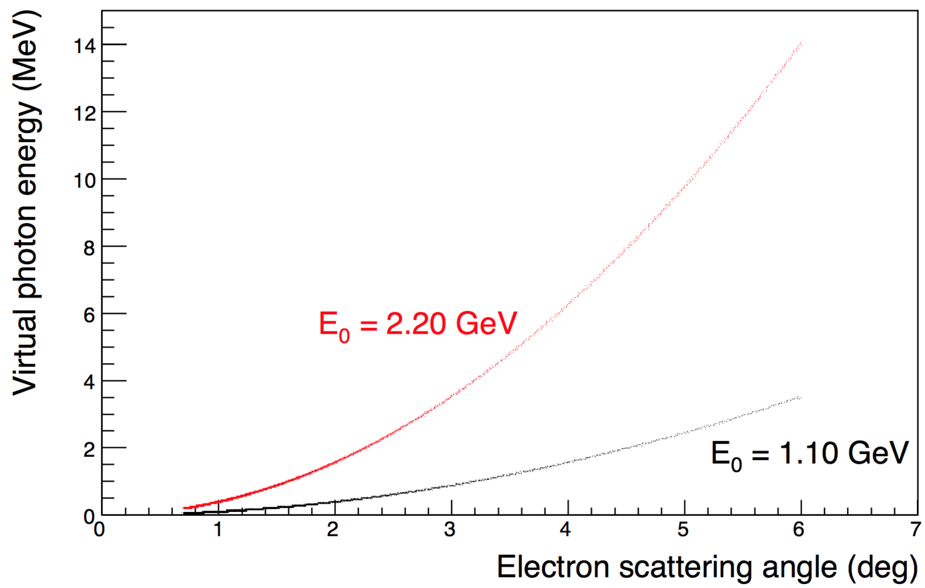

Figure 33: Virtual photon energy in $ed \to ed$ reaction *vs.* the electron scattering angle at incident beam energies of 1.1 GeV (black) and 2.2 GeV (red).

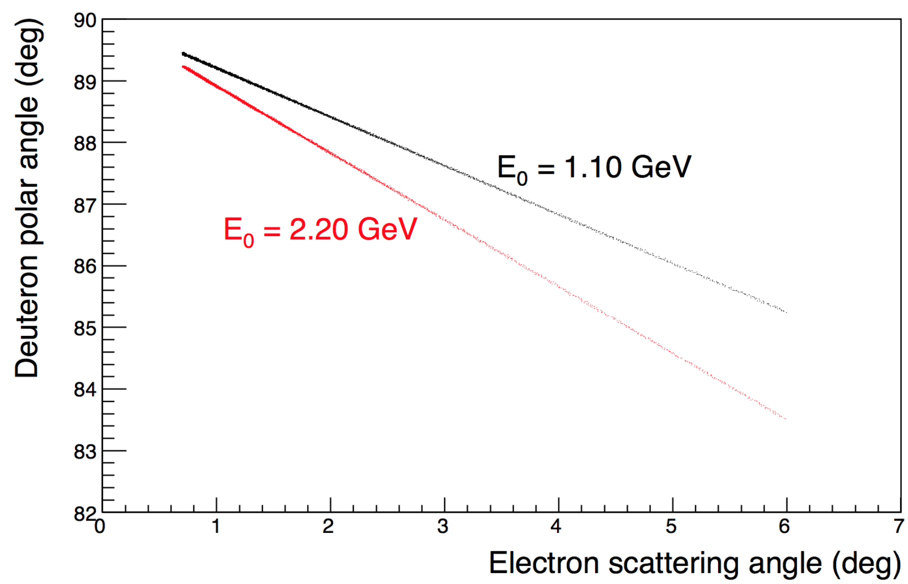

Figure 34: Recoil deuteron polar angle *vs.* the electron scattering angle at incident beam energies of 1.1 GeV (black) and 2.2 GeV (red).

6.1.2 Kinematics of ee scattering (Møller)

As it was described earlier, we will measure the Møller scattering process on atomic electrons simultaneously with the main $ed \to ed$ elastic scattering reaction. The Møller $e^-e^- \to e^-e^-$ differential cross section, at tree level, is getting contributions from the s and t photon exchange channels. In the center-of-mass (CM) system it is given by

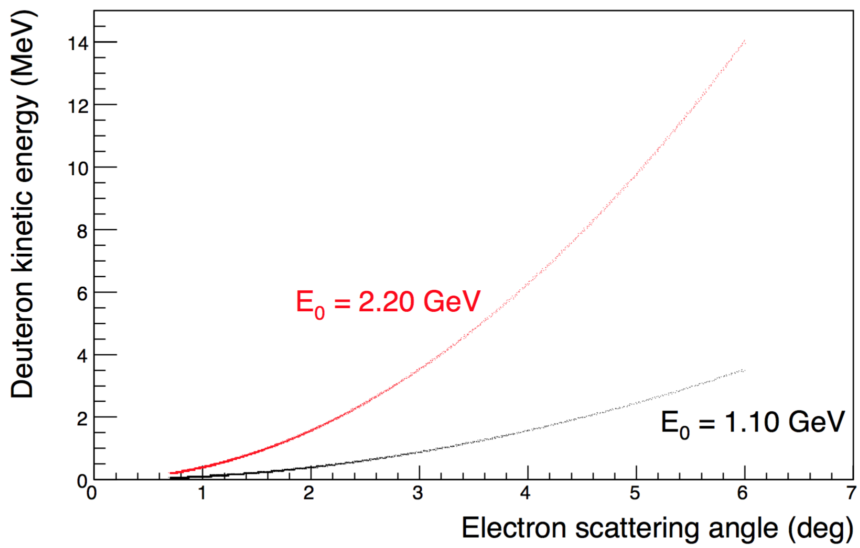

Figure 35: Recoil deuteron kinetic energy *vs.* the electron scattering angle at incident beam energies of 1.1 GeV (black) and 2.2 GeV (red).

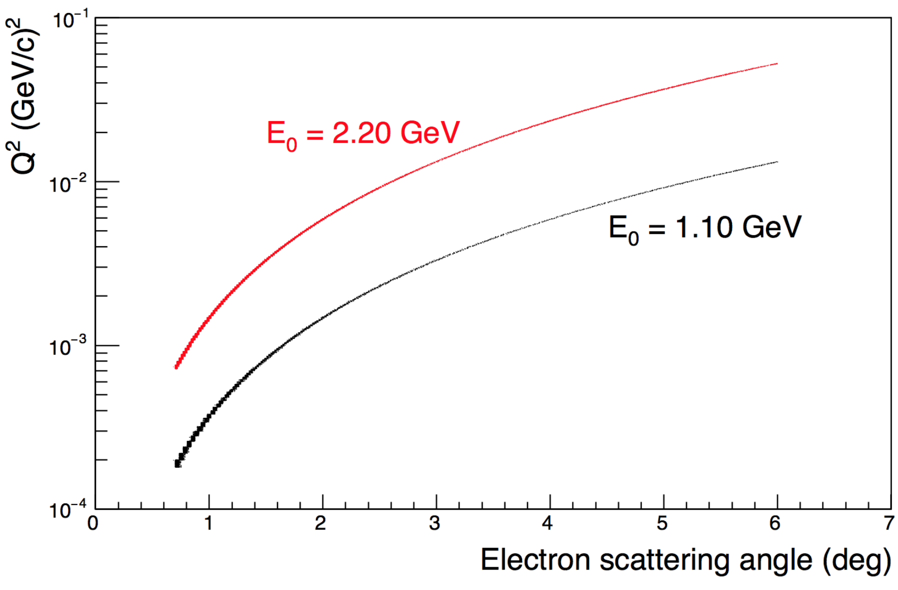

Figure 36: Four-momentum transfer squared (Q^2) in $e - d$ scattering *vs.* the electron scattering angle for both $E_0 = 1.1$ and 2.2 GeV energies.

$$\frac{d\sigma}{d\Omega} = \frac{\alpha^2}{s} \frac{(3 + \cos^2\theta^*)^2}{\sin^4\theta^*} \tag{15}$$

for high energies where the electron mass m_e can be neglected. Here $\alpha = 1/137$ is the fine structure constant, θ^* is the CM system polar scattering angle, and s is the interaction energy squared.

Some obvious features of the Møller scattering can be deduced from Eq. 15.

- The cross section is seen to diverge at $\cos\theta^* = \pm 1$. This is due to the fact that the electron mass was neglected. In a rigorous treatment, where m_e is not neglected, the Møller scattering formula remains finite even at $\cos\theta^* = \pm 1$.
- The magnitude of the cross section decreases as s increases, similar to that of the e^+e^- annihilation process.

In the scattering of two electrons, s may be written in a Lorentz invariant form as

$$s = 2m_e^2 + 2m_e E_{\mathrm{B}} , \tag{16}$$

where E_{B} is the beam energy.

The laboratory momentum of the scattered electron, p_{lab} is given by

$$p_{\mathrm{lab}} = \gamma_{\mathrm{CM}} \sqrt{(E^* + p^* \beta_{\mathrm{CM}} \cos\theta^*)^2 - \frac{m_e^2}{\gamma_{\mathrm{CM}}^2}} , \tag{17}$$

where $p*$, E^* are the momentum and energy of the incident electron in the CM system and γ_{CM} is the Lorentz factor. The relation between the laboratory scattering angle θ_{lab} and the CM scattering angle θ^* is given by

$$\tan\theta_{\mathrm{lab}} = \frac{1}{\gamma_{\mathrm{CM}}} \cdot \frac{\sin\theta^*}{\beta_{\mathrm{CM}}/\beta^* + \cos\theta^*} , \tag{18}$$

where β_{CM} is the velocity of the CM system and β^* is the velocity of the electron in the CM system.

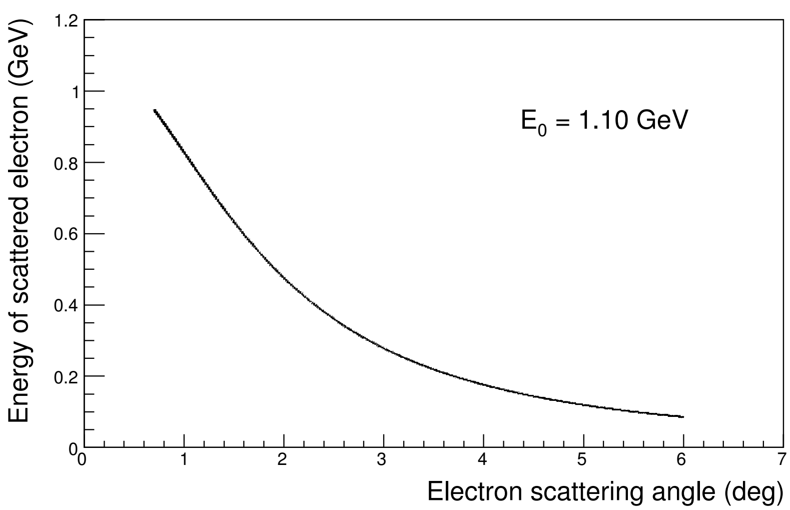

Figure 37: Energy of one of the electrons in Møller scattering *vs.* the laboratory scattering angle at an incident beam energy of 1.1 GeV.

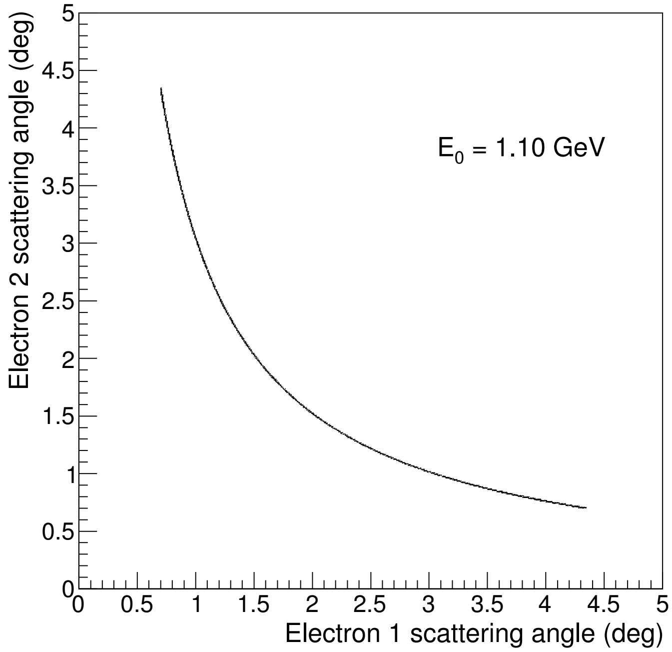

Figure 38: Angular correlation of the two electrons in Møller scattering in the laboratory system at an incident beam energy of 1.1 GeV (red) and 2.2 GeV (blue).

In the CM system of the Møller scattering, the momentum and energy of the incident electron are expressed by:

$$\begin{aligned} p^* &= \sqrt{\frac{m_e(E_\mathrm{B} - m_e)}{2}} \quad \text{and} \\ E^* &= \sqrt{\frac{m_e(E_\mathrm{B} + m_e)}{2}} \, . \end{aligned} \tag{19}$$

From Eqs. 16-19 it follows that

$$p_\mathrm{lab} = \frac{p_\mathrm{B}}{2}\,(1 + \cos\theta^*) \tag{20}$$

so that the laboratory momentum of the scattered electron does not depend on the CM total energy, but only on the beam energy and the CM scattering angle. From Eq. 18 one obtains the expression:

$$\tan^2\theta_\mathrm{lab} = \frac{2m_e}{E_\mathrm{B} + m_e} \cdot \frac{1 - \cos\theta^*}{1 + \cos\theta^*} \, . \tag{21}$$

The minimum opening angle in the laboratory system between the two electrons in the Møller scattering is when $\theta^* = \pi/2$:

$$\tan^2\theta_\mathrm{lab} = \frac{2m_e}{E_\mathrm{B} + m_e} \, . \tag{22}$$

Figure 37 shows one of the Møller scattered electrons' energy *vs.* its angle. The angular correlation between the two scattered electrons in the laboratory system as a function of beam energy are shown in Figs. 38.

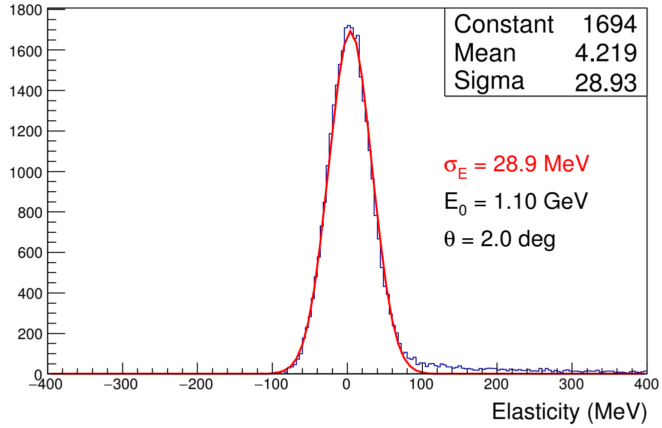

Figure 39: The *"elasticity"*, $(E_0 - E_{HyCal})$, distribution of detecting the electrons in $e-d$ elastic scattering at $E_0 = 1.1$ GeV and $\theta_e = 2°$.

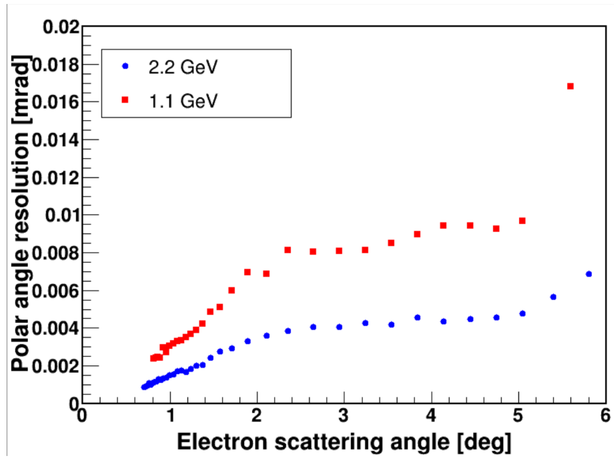

Figure 40: The polar angle resolution of detecting the scattered electrons with the GEM detectors.

6.2 Experimental Resolutions

In this experiment, just as in the PRad experiment, the scattered electrons from ed elastic and Møller scatterings will be detected with the high resolution, large acceptance HyCal electromagnetic calorimeter and GEM detectors.. The central part of the HyCal calorimeter ($PbWO_4$crystals) has good energy and position resolutions:

$$
\begin{aligned}
\sigma_E/E &= 2.6\%/\sqrt{E}\,, \\
\sigma_{x,y} &= 2.5\ \mathrm{mm}/\sqrt{E}\,.
\end{aligned}
$$

These numbers are a factor of two larger for the outside part of the calorimeter containing Pb-glass Cherenkov detectors [43].

In the PRad experiment we implemented one plane of GEM detectors with an excellent position resolution, ($\sim$ 72 μm) and very good electron detection efficiency ($\sim$ 93%). That dramatically improved the angular resolutions of the scattered electrons and, consequently, the resolutions in Q^2. However, the combination of one GEM and HyCal detectors did not provide a sufficient Z-vertex resolution for the effective rejection of background events from the beam line residual gas. For this experiment we are proposing to add the second GEM detector plane with a separation of $\sim$ 40 cm from the first GEM plane. Finally, we are

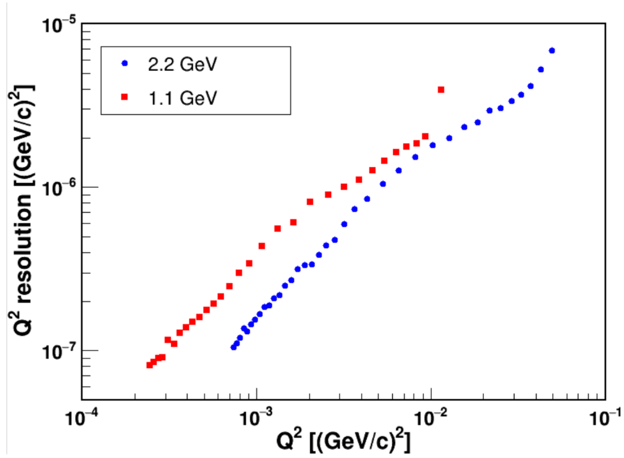

Figure 41: The Q^2 resolution for ed elastic scattering at $E_0 = 1.1$ GeV (red) and 2.2 GeV (blue).

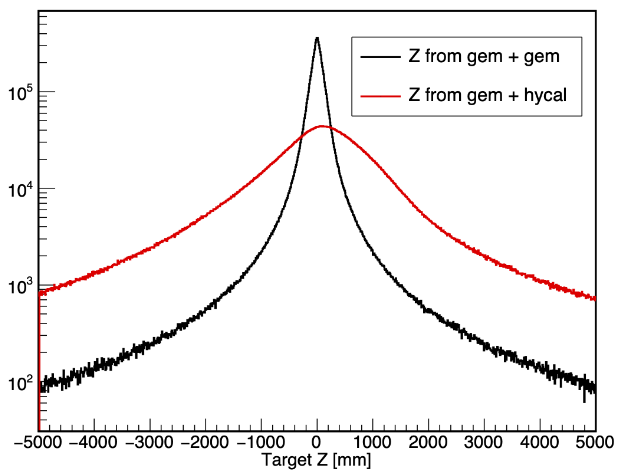

Figure 42: Reconstructed reaction z-vertex when using one GEM plane along with the HyCal vs using two GEM μRWELL detector planes.

proposing to add a Si-strip cylindrical recoil detector in the gas flow target chamber for the detection and identification of elastic $ed \to ed$ events from the deuteron breakup background processes (Sec. 5.3)

Detailed Monte Carlo simulations based on the GEANT4 package, were carried out for ed elastic and Møller scattering. These simulations were used to study the energy and position resolutions of detecting the scattered electrons and the recoiling deuterons together with the breakup protons over the full acceptance of the experimental setup.

6.2.1 Resolutions for the ed scattering process

Since the recoil nucleus has a kinetic energy of ~ 1 MeV at forward electron scattering angles, the difference between the incident beam energy and the detected energy in HyCal (the so called *"elasticity"*) will still be the first criterion in selecting the elastic events. Figure 39 shows the *"elasticity"*, $(E_0 - E_{HyCal})$, distribution in ed elastic scattering. A good energy resolution of $\sigma_E = 27$ MeV is seen at $E_0 = 1.1$ GeV.

The scattered electron polar angle will be measured by the high resolution GEM detectors (Fig. 40) providing an excellent resolution of $\sigma_{\theta_e} = 0.01^\circ$ at this forward angles. An important consideration in this type of experiments, performed at extreme forward direction, is the Q^2 resolution. Two GEM detectors, proposed in this experiment, together with the high precision of the CEBAF beam energy ($\sim 10^{-4}$), will provide a

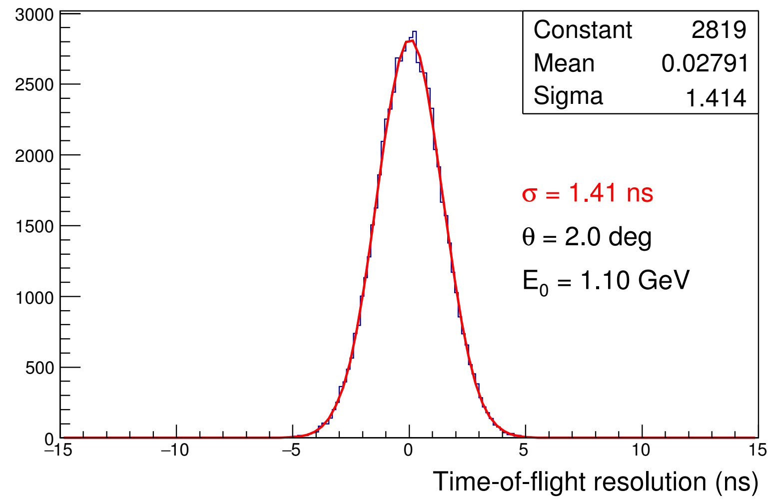

Figure 43: Time-of-flight resolution between the HyCal and the Si-strip recoil detector. The resolution is about the same for the $E_0 = 2.2$ GeV energy.

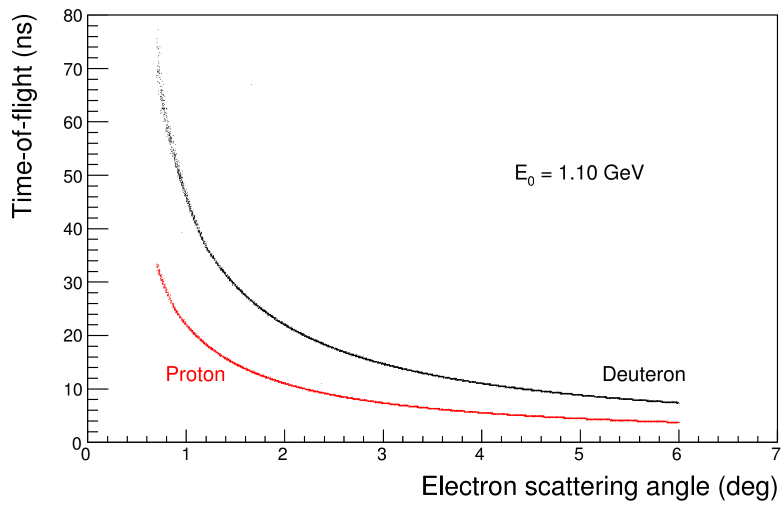

Figure 44: Time-of-flight *vs.* scattering angle for elastic $ed \to ed$ and $ep \to ep$ processes at an incident beam energy of 1.1 GeV. (ed and ep scattering are shown together for comparison only).

percent level resolution in Q^2 (Figure 41). The combination of two GEM detectors will also dramatically improve the reaction vertex resolution as demonstrated in Figure 42. This will allow an effective subtraction of background events from the residual gas in the upstream part of the beam line. Which was the largest background in the PRad experiment, especially at very small scattering angles.

As it is stated above, we propose to have cylindrical Si-strip sensors surrounding the gas flowing in the target area, to detect the recoiling deuterons to ensure elasticity in the ed scattering events. One of the major criteria in this event selection process will be time-of-flight difference between the Hycal calorimeter and the recoil detector. The time-of-flight resolution shown in Figure 43 assumes 1 ns time resolution for the Si-detectors and for the fADC based timing information from the HyCal. Knowing the position of the scattered electrons from the GEM detectors, one can easily improve the resolution to $\simeq 0.5$ ns.

Figures 44 and 45 show the time-of-flight differences between elastically scattered deuteron from $e-d$ process and elastic protons from $e-p$ for both energies of the incident beam. As it is seen, even with

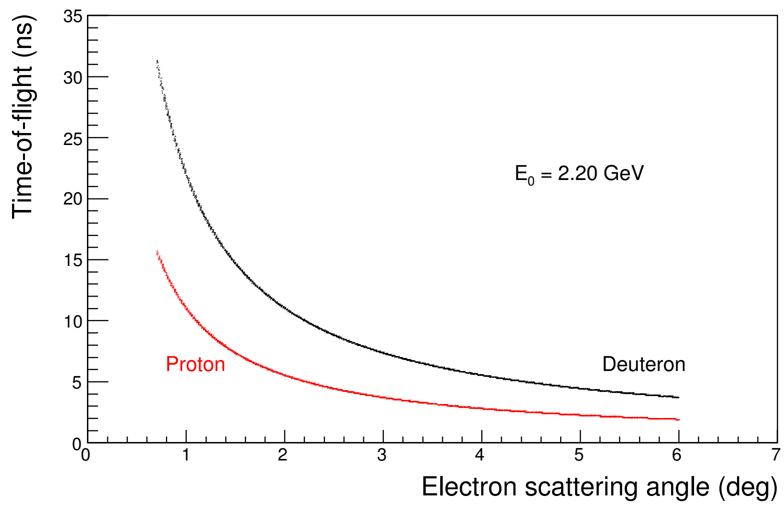

Figure 45: Time-of-flight *vs.* scattering angle for elastic $ed \to ed$ and $ep \to ep$ processes at an incident beam energy of 2.2 GeV. (ed and ep scattering are shown together for comparison only)

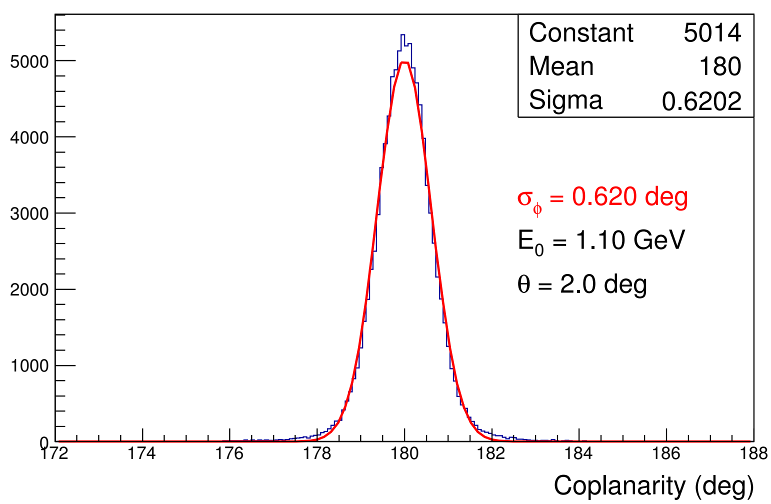

Figure 46: The simulated coplanarity distribution in the azimuthal direction, $\varphi_{e_1} - \varphi_{e_2}$, of the two electrons in Møller scattering at $E_0 = 1.1$ GeV. The minimum scattering angle cut implemented is $\theta_e \geq 0.7°$.

this conservative time resolution these two elastic processes can be safely separated within the projected scattered angular range.

6.2.2 Resolutions for the Møller scattering

Similar to $ed \to ed$ scattering, the *"elasticity"* $(E_0 - (E_1 + E_2))$ is the number one criterion for the Møller scattering event selection. Since the energy of both of the scattered electrons will be measured by the HyCal calorimeter, the resolution in this quantity is practically the same as that for the ed scattering (Figures 39 and 40).

The co-planarity of two scattered electrons (ignoring the radiative effects) $(\varphi_{e_1} - \varphi_{e_2} = \pi)$ is another important criterion for the Møller event selection process. Figure 46 shows an excellent resolution in the co-planarity of the two scattered electrons measured by the two GEM detectors.

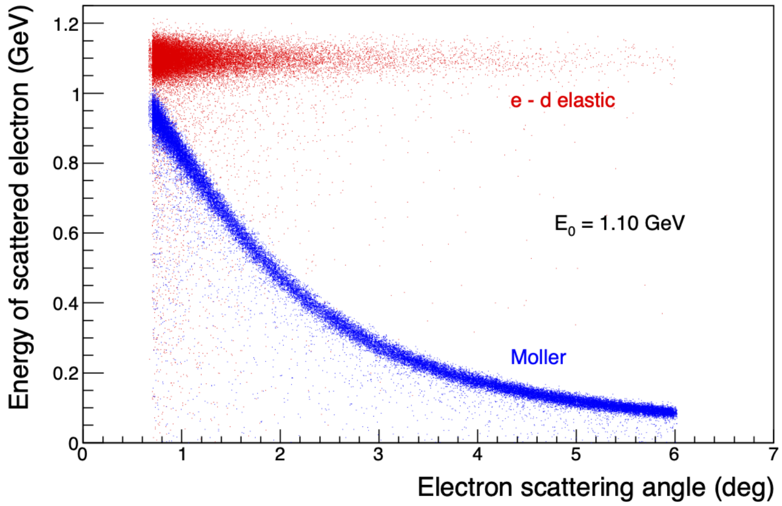

Figure 47: The simulated energy *vs.* scattering angle distribution of ed elastic and Møller scattered electrons at $E_0 = 1.1$ GeV. Internal and external radiative events have been included for both ed and Møller scattering. For the 1.1 GeV case the electrons from the two processes can be clearly identified starting from $\theta_e = 0.7°$.

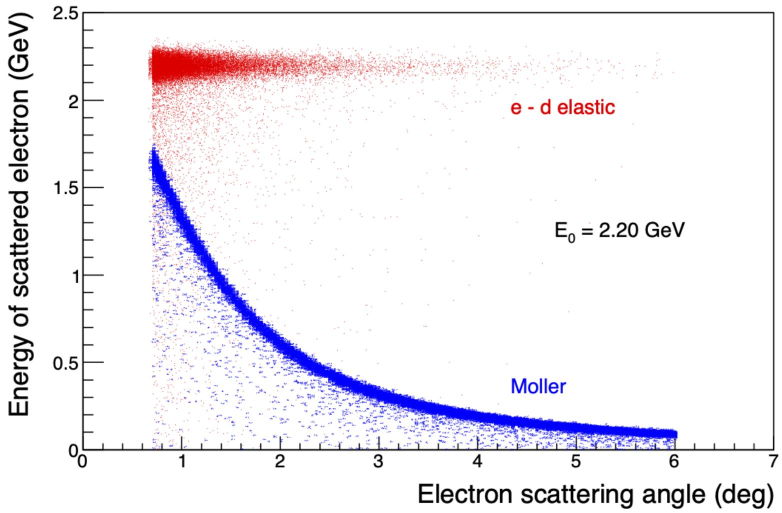

Figure 48: The simulated energy *vs.* scattering angle distribution of ed elastic and Møller scattered electrons at $E_0 = 2.2$ GeV. Internal and external radiative events have been included for both ed and Møller scattering. For the 2.2 GeV case, no minimum scattering angle cut on θ_e (inside the HyCal acceptance) is required here to clearly identify the electrons from the two processes.

A clear identification of the ed elastic scattering electrons from the Møller electrons requires that the tails of their energy distribution do not have any significant overlap. This condition can be achieved by requiring that the polar scattering angles of the electrons are above a certain minimum value. Figure 47 shows that above $\theta_e = 0.7°$ the electrons from the two processes can be cleanly separated for $E_0 = 1.1$ GeV. A similar plot for $E_0 = 2.2$ GeV is shown in Fig. 48. Here, the ed elastic scattered electrons are separated from the Møller scattered electrons for all polar angles accepted by the HyCal calorimeter ($\theta_e > 0.5°$). We have used the event generators, developed for the PRad experiment, that includes radiative effects for the Møller scattering and the $ep \to ep$ processes [37] and adapted them to include radiative effects for the $ed \to ed$ process. These generators were used in the GEANT4 based comprehensive simulation of the experiment. The particle identification and background studies described below were conducted with this comprehensive simulation.

6.3 Backgrounds and particle identification

The following background channels were studied for the DRad experiment.

6.3.1 Electro-disintegration

The electro-disintegration of the target deuterons ($ed \to epn$ inelastic breakup reaction) will constitute the major part of the background in this experiment.

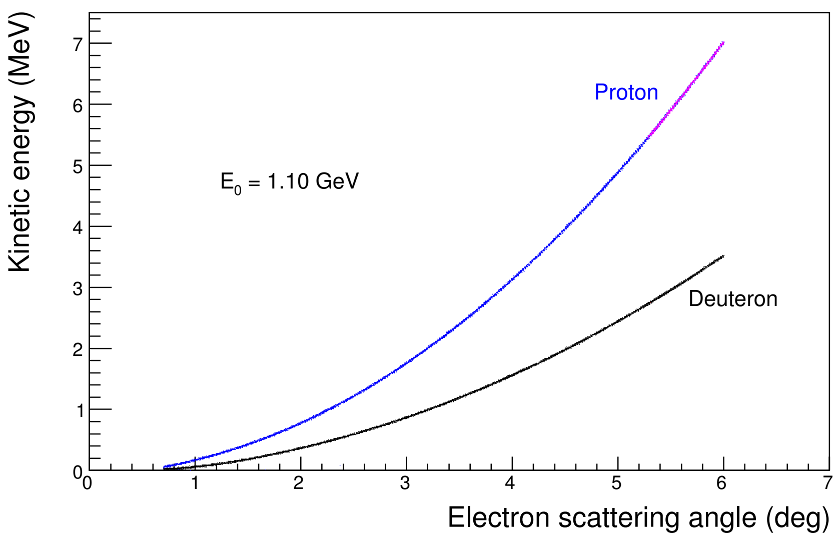

Figure 49: The simulated kinetic energy *vs.* electron scattering angle distribution of deuterons from ed elastic scattering and protons from ep elastic scattering at $E_0 = 1.1$ GeV. The protons that pass through the thin Si sensor are shown in magenta for protons. None of the deuterons can pass through the thin sensor. (ed and ep scattering are shown together for comparison only)

The kinetic energies of the recoil deuterons from the elastic ed scattering and the recoil protons from ep elastic scattering are shown in Fig. 49 for electron beam energy of 1.1 GeV and Fig. 50 for 2.2 GeV. The protons from the electro-disintegration of deuterons have a similar range in energy. The highest energy protons and deuterons that can pass through the thin Si layer into the thick Si layer are also shown in magenta for the protons and red for the deuterons. At 1.1 GeV none of the deuterons can pass through the thin Si layer. A Geant4 based Monte Carlo simulation of the experiment (detailed in Sec. 6.2) was used to simulate the energy deposited in the two layers of the recoil detector (described in Sec. 5.3).

The deuteron electro-disintegration was also simulated along with the ed elastic and ep elastic scattering processes. The rate of electro-disintegrated protons was approximated as;

$$N(ed \to enp) \simeq N_{\gamma *} \times \Delta\sigma(\gamma d \to np) \times N_{target},$$

where $N_{\gamma *}$ is the number of virtual photons, which for this thin target ($\sim 10^{-7}$ r.l.) can be calculated as $N_{\gamma *} \simeq 0.02 \times N_e$, where N_e is the number of electrons. The the integrated photo-disintegration cross

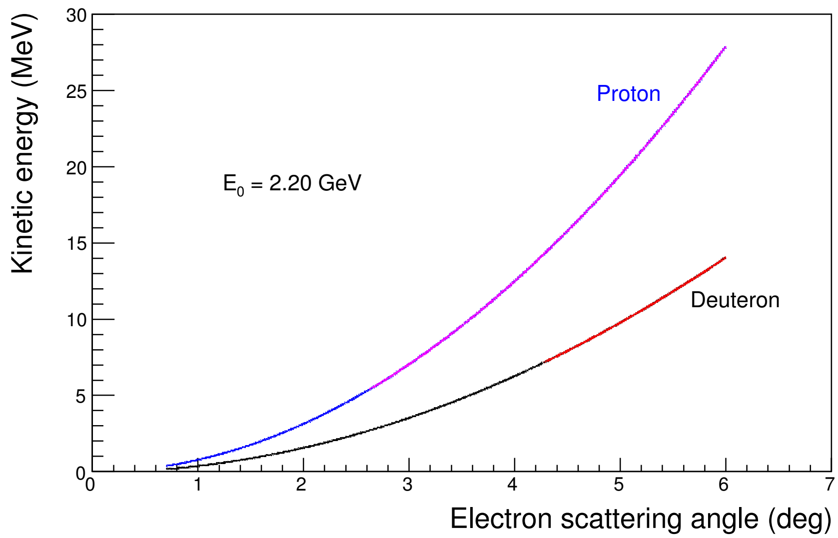

Figure 50: The simulated kinetic energy *vs.* electron scattering angle distribution of deuterons from ed elastic scattering and protons from ep elastic scattering at $E_0 = 2.2$ GeV. The protons that pass through the thin Si sensor are shown in magenta for protons and red for deuterons. (ed and ep scattering are shown together for comparison only)

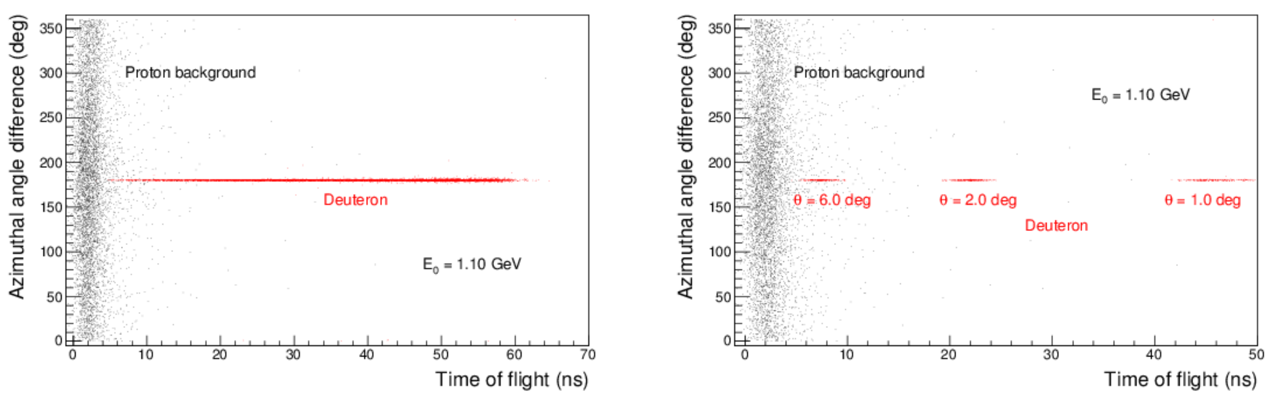

Figure 51: The distribution of $\Delta\phi$ angle from the GEM and the recoil detectors *vs.* time-of-flight difference between the recoil detector and the veto counters, for the deuterons from ed elastic scattering (red) and protons from deuteron disintegration (black) for $E_0 = 1.1$ GeV. All events with electron scattering angles between 0.7° and 6°(left) and events with electron scattering angles of 1°, 2° and 6° (right) are shown.

section $\Delta\sigma(\gamma d \to np)$ at forward angles ($\theta_e = 0.7° - 6.0°$), accepted by the setupcross section, is taken to be 4 mb. With that;

$$N(ed \to enp) \simeq 0.02 \times 6.25 \times 10^{10} \times 4 \times 10^{-27} \times 2 \times 10^{18} = 10 \text{ events/s}$$

As shown in Sec. 9.1, the rate for elastic $ed \to ed$ events is expected to be $\simeq 173$ events/s.

In the Monte Carlo simulation the outgoing angle of the proton and the neutron is generated uniformly over the full angular phase space. The relative energy of the np system after disintegration is defined as $E_{np} = W - m_p - m_n$, where W is the invariant mass of the final state. E_{np} is generated uniformly from 0 up to 100 MeV. The distribution of azimuthal angle difference $\Delta\phi$ as measured by the GEM and the recoil

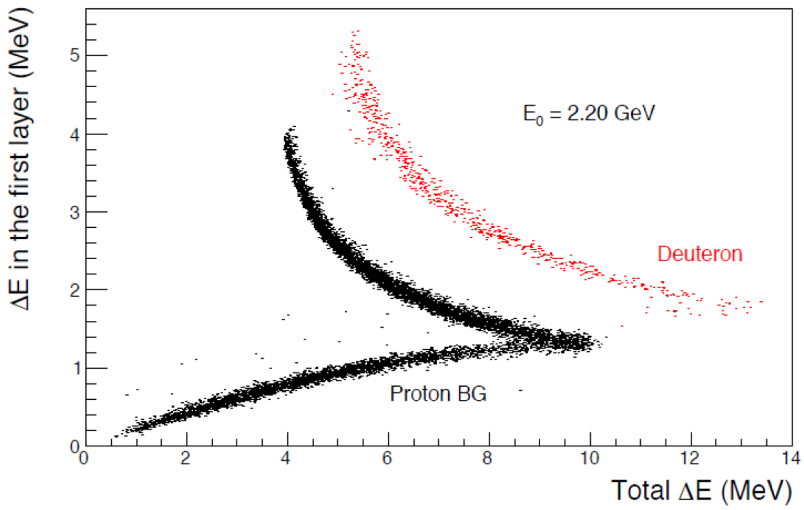

Figure 52: The energy loss in the first(thin) Si detector *vs.* the total energy deposition in the two Si detectors for deuterons from ed elastic scattering and protons from electro-disintegration of the deuteron at $E_0 = 2.2$ GeV.

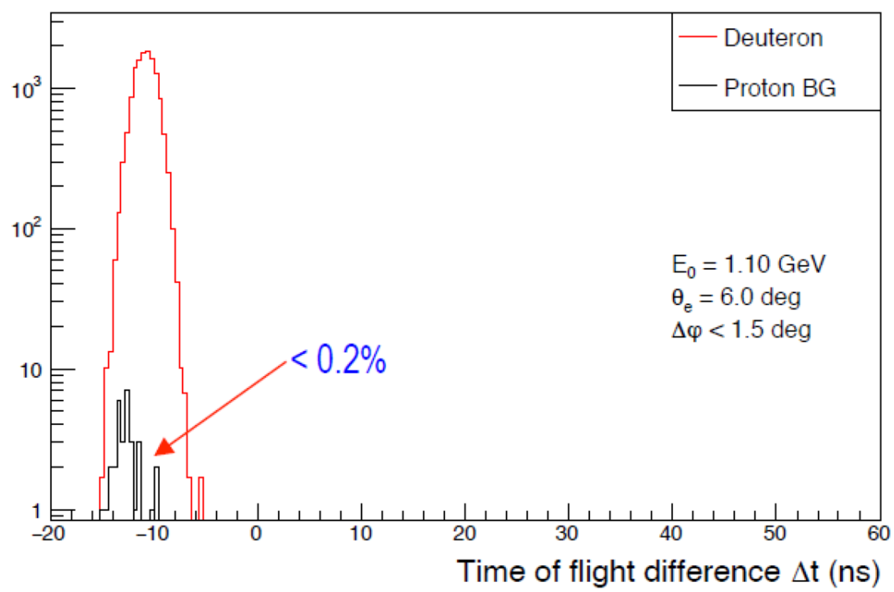

Figure 53: The time-of-flight different at $E_0 = 1.1$ GeV and $\theta_e = 6.0°$.

detectors *vs.* time-of-flight difference between the recoil detector and the veto counters, for the deuterons from ed elastic scattering (red) and protons from deuteron disintegration (black) for $E_0 = 1.1$ GeV, are shown in Fig. 51. The left panel is for all angles, while the right panel is for 1°, 2° and 6° angles only. A time-of-flight resolution of 1 ns is sufficient to distinguish the deuterons from the protons produced by the deuteron break-up reaction, for all angles except for the highest angles.

We will also select events by the ΔE detected in the first layer (thin Si sensor) and the total ΔE detected by the two layers (see Fig. 52). Combination of these two criteria will clearly separate the ed elastic events from the deuteron breakup process.

Under our study, at $E_0 = 2.2$ GeV, a cut on ΔE in the first layer and the total ΔE in the Si-strip detectors alone is already very effective for the particle identification. At $E_0 = 1.1$ GeV, applying the above two cuts removes the proton background for most angles, except for $\theta_e = 6.0°$. As shown in Fig. 53, when $\theta_e = 6.0°$, the background level is less than 0.2%.

6.3.2 Quasi-inelastic process

Except for the above process, one should also consider a scenario, where the electron interacts inelastically with the proton or neutron inside the deuteron. Let us show some details on how we treat such a process in what follows.

Quasi-inelastic generator Based on the Christy 2018 model for the ep inelastic process [72] and the nucleon Fermi momentum distribution inside the deuteron, we developed a quasi-inelastic generator for ed scattering to study the process $e + d \to e' + X$, where the virtual photon couple with the nucleons inside the deuteron, and X is the inelastic final states. Here we assume the effects of the proton and the neutron are the same. The only difference between them is the mass. The algorithm of the created generator is discussed below:

A. To simulate the Fermi motion, we randomly generate the momentum of the nucleon p_{Fermi} by following the Hulthen distribution [73], and then uniformly generate the polar angle $\theta_{Fermi} \in (0, \pi)$ and azimuthal angle $\phi_{Fermi} \in (0, 2\pi)$.

B. The Christy model returns the differential cross-section value $\frac{d\sigma}{d\Omega d\nu}(\theta, \nu)$, where $\nu = E - E'$ is the energy transfer, and θ is the polar angle of the scattered electron in the proton rest frame. To sample the events under different Fermi momenta, we fill a 2-D cross-section table in the lab frame each time by performing the following steps:

(i) Loop over the polar angle θ_e and the energy E'_e of the scattered electron in the lab frame in the following range: $\theta_e \in (\theta_{min}, \theta_{max})$ and $E'_e \in (0, E_e)$, where E_e is the beam energy.

(ii) Boost both the initial 4-momentum $(E_e, \vec{p}_e)$ and the final 4-momentum $(E'_e, \vec{p}'_e)$ from the lab frame to the nucleon (proton or neutron) rest frame, in order to obtain $(E_{rf}, \vec{p}_{rf})$ and $(E'_{rf}, \vec{p}'_{rf})$ respectively. Here the subscript rf stands for "rest frame", and θ_{rf} is defined as the angle between the initial and final momenta of the electron in the nucleon rest frame.

(iii) For the reaction $e + d \to e' + X$, the invariant mass of X can be calculated. In order to make sure the energy is conserved, we require $m_X > m_p$.

(iv) The value of the differential cross-section is calculated by $xs \equiv \frac{d\sigma}{d\Omega d\nu}(\theta_{rf}, \nu = E_{rf} - E'_{rf})$.

(v) Fill a 2-D table of θ_e and E'_e, which is the angle and the energy of the scattered electron in the lab frame, with a weight factor xs.

C. Use the 2-D table to generate the θ_e and E'_e values with the given weight, and uniformly generate $\phi_e \in (0, 2\pi)$, where ϕ_e is the azimuthal angle of the scattered electron in the lab frame.

The normalization To compare the quasi-inelastic process with the elastic process, we need to scale their distribution of the counts to the same integrated luminosity L, where $L = N/\sigma_{tot}$. Here N is the number of the generated events and σ_{tot} is the total cross-section.

For the elastic process, the total cross-section is calculated by the integration of the differential cross-section to the solid angle in the range of θ_e and ϕ_e that is used for calculations.For the quasi-inelastic process, the total cross-section calculation is combined for the Fermi motion and the beam energy dependence of the cross-section in the nucleon rest frame. For a specific Fermi 4-momentum $(E_{Fermi}, \vec{p}_{Fermi})$ with the magnitude of the Fermi momentum is p_{Fermi}, the Hulthen weight is defined as $H = f_{Hulthen}(p_{Fermi})$, where $f_{Hulthen}(p_{Fermi})$ is the probability distribution of the Fermi momentum values. Since $\frac{d\sigma}{d\Omega d\nu}(\theta_{rf}, \nu = E_{rf} - E'_{rf})$ is a value from the fit rather than a function, we can calculate the integrated cross-section in the nucleon rest frame by doing the following summation:

$$\begin{aligned}
\sigma_0 &= \int_0^{E_{rf}} \int_0^{2\pi} \int_{\theta_{rf_{min}}}^{\theta_{rf_{max}}} \frac{d\sigma}{d\Omega d\nu}(\theta_{rf}, \nu = E_{rf} - E'_{rf})\, sin\theta\, d\theta\, d\phi\, dE'_{rf} \\
&= \sum_{j=0}^{M} (E'_{j+1} - E'_j)[S(E'_j) + S(E'_{j+1})]/2 \\
S(E'_j) &= \int_{\theta_{rf_{min}}}^{\theta_{rf_{max}}} \frac{d\sigma}{d\Omega d\nu}(\theta_{rf}, \nu = E_{rf} - E'_j)\, sin\theta\, d\theta\, d\phi \\
&= \sum_{i=0}^{N} 2\pi(\theta_{i+1} - \theta_i) \left[sin\theta_i \frac{d\sigma}{d\Omega d\nu}(\theta_i, \nu = E_{rf} - E'_j) + sin\theta_{i+1} \frac{d\sigma}{d\Omega d\nu}(\theta_{i+1}, \nu = E_{rf} - E'_j) \right] /2
\end{aligned} \tag{23}$$

We define the total weight:

$$W = \sigma_0 \times H \tag{24}$$

which is different for various Fermi momenta.

The total cross-section of $\gamma p \to X$ or $\gamma n \to X$ taking into account the Fermi motion is:

$$\sigma_{p/n} = \frac{\int W(\vec{p}_{Fermi})\, d\vec{p}_{Fermi}}{\int f_{Hulthen}(\vec{p}_{Fermi})\, d\vec{p}_{Fermi}} \tag{25}$$

In summation, the total cross-section of the quasi-inelastic process is:

$$\sigma_{tot} = \sigma_p + \sigma_n \tag{26}$$

Results and the further suppression of the background

When the beam energy is 1.1 GeV, the result is shown in Fig. 54(left). After applying the energy cut, the normalized contamination rate from the quasi-elastic process is no more than 0.13%. When the beam energy is 2.2 GeV, the result is shown in Fig. 54 (right).

To further suppress the quasi-inelastic process, we can study the kinematics of the final particle system X. In this experiment, we use the recoil detector to detect the charged particles. In the end, only the final states that include the protons will be the background in our experiment:

(i) Assume X consists of a proton and some other particles Y $(X = p + Y)$. Since the 4-momentum of X $(E_X, \vec{p}_X)$ is known from the simulation, we can calculate the 4-momentum of the proton.

(ii) In the X rest frame, the energy of the proton is $E_{pr} = \frac{m_X^2 + m_p^2 - m_Y^2}{2m_X}$. The lightest hadron is π^0, so that $m_Y > m_{\pi^0}$.

(iii) Uniformly generate the given quantities in the following ranges: $E_{pr} \in (m_p, \frac{m_X^2 + m_p^2 - m_{\pi^0}^2}{2m_{\pi^0}})$, $\theta_{pr} \in (0, \pi)$, $\phi_{pr} \in (0, 2\pi)$ and obtain the 4-momentum of the proton $(E_{pr}, \vec{p}_{pr})$ in the X rest frame.

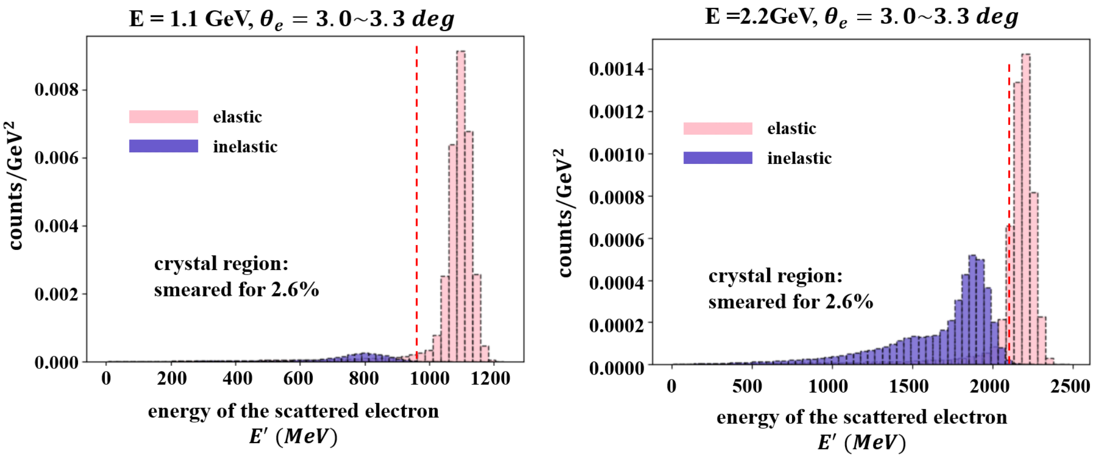

Figure 54: Comparison between the elastic and inelastic processes at 1.1 GeV (left) and 2.2 GeV (right) beam energies, at $\theta_e \sim 3.0 - 3.3°$, with E' smeared b 2.6%. The energy cut can be applied without a great loss of the signal.

(iv) Boost $(E_{pr}, \vec{p}_{pr})$ to the lab frame, and calculate the polar angle θ_p of the proton in the lab frame. Considering the geometrical acceptance of the recoil detector, we require $83.5° < \theta_p < 89.5°$.

Following the above steps, we find the acceptance that the proton can be detected by the recoil detector is less than 0.32%, while the acceptance of the elastic process is more than 99%. The normalized contamination rate is less than 0.02% at 2.2 GeV and 0.0017% at 1.1GeV.

Moreover, as discussed in Sec. 6.3.1 and shown in Fig.52, when the beam energy is 2.2 GeV, the deuteron have enough kinetic energy to be detected by the recoil detector. Since the energy deposition is only related to the detected particles and to the thickness of the silicon strips in the detector, a 2-D cut on the energy deposition (in the first layer) versus the total energy deposition is very effective for particle identification.

In summary, at 1.1 GeV, we need to apply the cut on the energy of the scattered electron and use the signal in the recoil detector to reject the quasi-inelastic background. When $\theta_e < 1.1°$, due to the passive layer on the Si detector, there is no signal from the proton or the deuteron, so we need to use the energy of the scattered electron to remove the background. When $\theta_e > 1.1°$, we can use the information in the recoil detector to reject the background. At 2.2 GeV, we can use the energy deposition in the recoil detector to cleanly separate the proton background from the deuteron signal. Assuming the 2-D cut on the energy depositions can reject more than 90% of the proton background, the normalized contamination rate at 2.2 GeV is less than 0.002%. In the end, the influence on the deuteron radius is less than 0.017%.

6.3.3 Coherent pion production process

The other possible background comes from the coherent pion production process ($ed \to ed\pi^0$). In order to study this process, its kinematics should be considered first. Assuming that the 4-momentum of the pion $(E_{\pi^0}, \vec{p}_{\pi^0})$, the polar angle θ_e and the azimuthal angle ϕ_e of the scattered electron are known, the energy of the scattered electron will be given by

$$E' = \frac{2m_d E - m_{\pi^0}^2 + 2(E\, p_{\pi_z^0} - p_{\pi^0}^2) - 2E_{\pi^0}(E + m_d - E_{\pi^0})}{2m_d + 4E\, sin^2(\theta_e/2) - 2E_{\pi^0} + 2(sin\theta_e\, cos\phi_e\, p_{\pi_x^0} + sin\theta_e\, sin\phi_e\, p_{\pi_y^0} + cos\theta_e\, p_{\pi_z^0})} \tag{27}$$

where E is the beam energy. The momentum vector of the pion can be represented by $\vec{p}_{\pi^0} = (p_{\pi_x^0},\, p_{\pi_y^0},\, p_{\pi_z^0}) = (p_{\pi^0}\, sin\theta_{\pi^0}\, cos\phi_{\pi^0},\; p_{\pi^0}\, sin\theta_{\pi^0}\, sin\phi_{\pi^0},\; p_{\pi^0}\, cos\theta_{\pi^0})$.

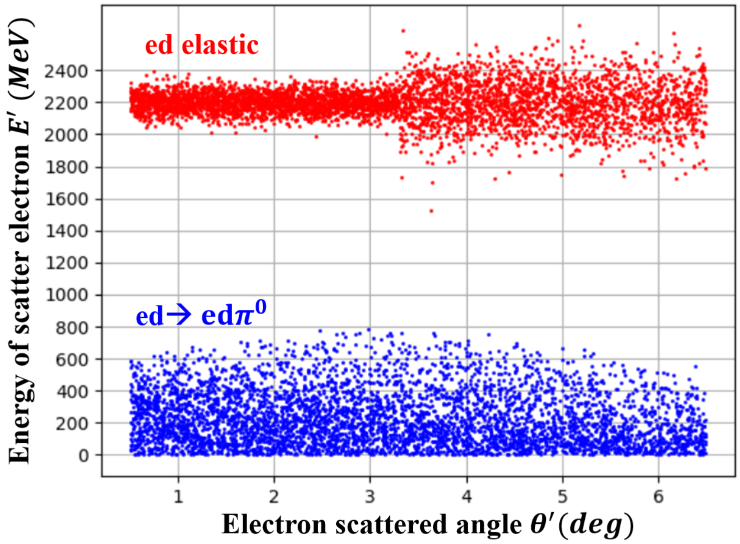

Figure 55: The energy of the scattered electron for the ed elastic process and pion production process, obtained at 2.2 GeV beam energy, with a cut on the polar angle of the recoiled deuteron. To mimic the detection effect (energy resolution of the Hycal), at $\theta_e < 3.3°$, E' is smeared for 2.6%; at $\theta_e > 3.3°$, E' is smeared for 6.5%.

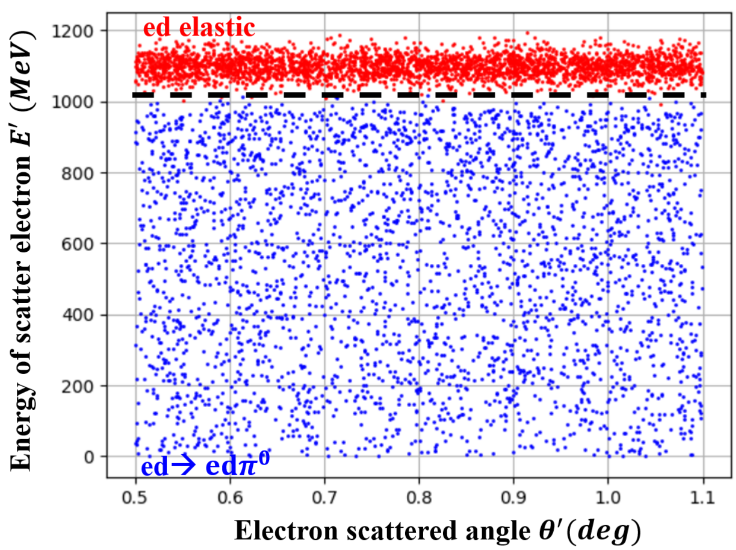

Figure 56: The energy of the scattered electron for the ed elastic process and pion production process, obtained at 1.1 GeV beam energy, without a cut on the polar angle of the recoiled deuteron. To mimic the detection effect (energy resolution of the Hycal), E' is smeared for 2.6%.

To calculate the range of validity of E', the following steps should be fulfilled:

(i) Randomly generate θ_{π^0}, ϕ_{π^0}, p_{π^0}, θ_e and ϕ_e, and then calculate E' by Eq. (27).

(ii) Require $E' > 0$ and the energy of the recoiled deuteron to be $E_d = E + m_d - E' - E_{\pi^0} > m_d$.

(iii) Considering the geometrical acceptance of the recoil detector, select only those events for which the polar angle of the deuteron satisfies $83.5° < \theta_d < 89.5°$.

Following this procedure, the result for 2.2 GeV beam energy is shown in Fig. 55. We can separate the pion production process from the ed elastic process by applying a cut on the scattered electron energy.

At 1.1 GeV beam energy, no events from the pion production process is in acceptance of the recoil detector. Then we can reject this background by looking at the signal on the recoil detector at $\theta_e > 1.1°$. Also, at $\theta_e < 1.1°$, there is no signal from the elastic process in the detector. The energy distribution without a cut on the polar angle of the recoiled deuteron is shown in Fig. 56. At $\theta_e < 1.1°$, we can use a cut on the scattered electron energy to reject the background. In summary, the contribution from this process will be negligible in our experiment.

7 Advanced Extraction of Deuteron Charge Radius

7.1 The fitting procedure

At very low but experimentally accessible Q^2 such as $\sim\ 10^{-4}$ $(\mathrm{GeV/c})^2$ and small θ, the contributions from G_Q^d and G_M^d to the scattering process are negligible. Consequently, in order to extract the deuteron root-mean-square (RMS) charge radius from e-d scattering data, as discussed in Sec.2.1, one should find G_C^d as a function of Q^2 according to

$$R_d \equiv R_{d,RMS} \equiv \sqrt{\langle R^2 \rangle} = \left(-6 \left. \frac{\mathrm{d}G_C^d(Q^2)}{\mathrm{d}Q^2} \right|_{Q^2=0} \right)^{1/2} . \tag{28}$$

Then the radius can be obtained by fitting G_C ($G_C^d \equiv G_C$) to the experimental data as a function of Q^2, and calculating the slope of this function at $Q^2 = 0$.

Ref. [44] gives a general framework with input form factor functions and various fitting functions, in order to find functional forms that allow for a robust extraction of the input charge radius of the proton, R_p, for the PRad experiment. Analogously, we can use a similar framework for extracting input R_d. In the fitting procedure, depending on a fitting function, different bias and variance will be obtained. The bias is calculated by taking the difference between the fitted radius mean value, and the input radius value from a model: $R_d[\text{bias}] = R_d[\text{mean fit}] - R_d[\text{input}]$. The fitted radius mean value is the central value, and the variance is the fitting uncertainty (σ) represented by the RMS value of a set of $R_d[\text{fit}]$ results.

There are various well-developed electric form factor models for the proton. Most of the models have been fitted with experimental data in higher Q^2 ranges compared to the PRad Q^2 range. Meanwhile, these models have different kinds of extrapolation in a lower Q^2 range (like the PRad Q^2 range). The robustness of a fitter when extracting the RMS proton charge radius in a lower Q^2 (PRad) range can be tested by fitting pseudo-data generated by different models in that range [44]. To control the total uncertainty, the number of free parameters in a fitting function should not be too large. Otherwise, the variance from the fitting will be very large. If the variance coming out from a given fit is small and the bias is within this variance, then the corresponding fitter is considered to be robust. To compare the goodness between different robust fitters, the quantity called Root Mean Square Error (RMSE) is used:

$$\mathrm{RMSE} = \sqrt{\mathrm{bias}^2 + \sigma^2}\,. \tag{29}$$

The smaller the RMSE is, the better the corresponding fitter is. However, if we consider the G_C models to use for DRad, then in this case there are only two contemporary deuteron charge form factor models that one can use [46]. We can use the fitting procedure of [44] for extracting the deuteron radius, nevertheless, limited by the number of G_C models, we can not exactly imitate different kinds of extrapolation in a lower Q^2 (which one can do for the proton models) when studying fitters for R_d. This situation requires a more comprehensive method for testing the robustness of DRad fitters.

The studies of Ref. [44] showed that the function Rational (1,1) is robust and the best one for extraction of R_p for PRad, which is given by

$$f_{\mathrm{Rational\,(1,1)}}(Q^2) \equiv \mathrm{Rational}\ (1,1) = p_0\, G_E(Q^2) = p_0 \frac{1 + p_1^{(a)} Q^2}{1 + p_1^{(b)} Q^2}\,, \tag{30}$$

where p_0 is a floating normalization parameter, $p_1^{(a)}$ and $p_1^{(b)}$ are two free fitting parameters. The radius is determined by $R_p = \sqrt{6\left(p_1^{(b)} - p_1^{(a)}\right)}$.

For the DRad experiment, we will test this function and compare different functions with a newly developed method to test the robustness of the fitters.

7.2 Method and Test

7.2.1 Pseudo-data generation and statistical fluctuations

A.Generator There are two generators for DRad for generating G_C values at given Q^2. They are two parameterizations based on the available experimental data. For simplicity we name them as Abbott1 and Abbott2 models.

Parameterization I (Abbott1 model) [46]:

$$G_C(Q^2) = G_{C,0} \cdot \left[1 - \left(\frac{Q}{Q_C^0}\right)^2\right] \cdot \left[1 + \sum_{i=1}^{5} a_{Ci}\, Q^{2i}\right]^{-1}, \tag{31}$$

where $G_{C,0}$ is a normalized factor fixed by the deuteron static moment, Q_C^0 and a_{Ci} are all together six free parameters, which can be found on the website of [46].

Parameterization II (Abbott2 model) [46, 47]:

$$G_C(Q^2) = \frac{G^2(Q^2)}{(2\tau+1)}\left[\left(1 - \frac{2}{3}\tau\right) g_{00}^{+} + \frac{8}{3}\sqrt{2\tau}\, g_{+0}^{+} + \frac{2}{3}\,(2\tau - 1)\, g_{+-}^{+}\right], \tag{32}$$

where

$$g_{00}^{+} = \sum_{i=1}^{n} \frac{a_i}{\alpha_i^2 + Q^2}, \quad g_{+0}^{+} = Q\sum_{i=1}^{n} \frac{b_i}{\beta_i^2 + Q^2}, \quad g_{+-}^{+} = Q^2\sum_{i=1}^{n} \frac{c_i}{\gamma_i^2 + Q^2}. \tag{33}$$

$G(Q^2)$ in Eq. (32) is a dipole form factor expressed as

$$G(Q^2) = \left(1 + \frac{Q^2}{\delta^2}\right)^{-2}, \tag{34}$$

where δ is some parameter of the order of nucleon mass.

The twenty four parameters $a_i, b_i, c_i, \alpha_i^2, \beta_i^2, \gamma_i^2$ can also be found on the website of [46]. They are constrained by the following twelve relations:

$$\begin{aligned}
&\sum_{i=1}^{n} \frac{a_i}{\alpha_i^2} = 1, \qquad &&\sum_{i=1}^{n} b_i = 0, \qquad &&\sum_{i=1}^{n} \frac{b_i}{\beta_i^2} = \frac{2 - \mu_M^d}{2\sqrt{2}M_d},\\
&\sum_{i=1}^{n} c_i = 0, &&\sum_{i=1}^{n} c_i\gamma_i^2 = 0, &&\sum_{i=1}^{n} \frac{c_i}{\gamma_i^2} = \frac{1 - \mu_M^d - \mu_Q^d}{4M_d^2},\\
&\alpha_n^2 = 2M_d\,\mu^{(\alpha)}, &&\alpha_i^2 = \alpha_1^2 + \frac{\alpha_n^2 - \alpha_1^2}{n-1}(i-1), &&i = 1, ..., n.
\end{aligned} \tag{35}$$

where $\mu^{(\alpha)}$ has the dimension of energy and is of the order of Λ_{QCD}. In total, there are twelve free parameters in this model.

B. Fluctuation adder and pseudo-data generation procedure The binning choice in this study is based on the PRad binning. Since the acceptance for DRad apparatus is different from that of PRad, there are thirty bins from 0.8° to 6.0° at 1.1 GeV beam energy, and thirty seven bins from 0.7° to 6.0° at 2.2 GeV.

To mimic the bin-by-bin statistical fluctuation of the data, the G_C pseudo-data statistical uncertainty is smeared by adding the G_C in each Q^2 bin with a random number following the Gaussian distribution, $\mathcal{N}(\mu, \sigma_g^2)$, given by

$$\mathcal{N}(\mu,\, \sigma_g^2) = \frac{1}{\sqrt{2\pi\sigma_g^2}}\, e^{-\frac{(G_C-\mu)^2}{2\sigma_g^2}} \,. \tag{36}$$

In this work we take $\mu = 0$ and $\sigma_g = \delta G_C$, where δG_C comes from the statistical uncertainty of simulated e-d elastic scattering data. Let us now give some more details on data generation and fitting procedure:

(i) Thirty G_C pseudo-data points at 1.1 GeV and thirty seven G_C pseudo-data points at 2.2 GeV are generated from the two deuteron models in Eqs. (31) or (32);

(ii) To add the statistical fluctuation, totally sixty seven pseudo-data points generated in (i) are added with sixty seven different random numbers following Eq. (36);

(iii) A set of pseudo-data is fitted by a specific fitter $f_E(Q^2)$. In this procedure the data points at 1.1 GeV and 2.2 GeV are combined and fitted by a fitter with two different floating normalization parameters corresponding to two different energy beams. The other fitting parameters in the fitter are required to be the same for the two energies;

(iv) The fitted radius is calculated from the fitted function in (iii), with

$$R_d[\text{fit}] = \left(-6\, \frac{\mathrm{d}f_E(Q^2)}{\mathrm{d}Q^2}\bigg|_{Q^2=0} \right)^{1/2} \,; \tag{37}$$

(v) The above step is repeated 10,000 times for obtaining 10,000 sets of G_C pseudo-data, diluted by Eq. (36), and 10,000 $R_d[\text{fit}]$ values are calculated too;

(vi) $R_d[\text{mean fit}]$ is the mean value of the 10,000 $R_d[\text{fit}]$ values, and the variance σ is the RMS value of this $R_d[\text{fit}]$ distribution.

If a fitter has uncertainties in its fixed parameters, we will consider these uncertainties when calculating the RMS value by varying those parameters and following a uniform distribution in their 1σ uncertainty range. Then one can use the fitter function with different fixed parameters to fit 10,000 sets of pseudo-data generated from the above procedure. This step will be repeated for 100 times, after which we use the largest value as the RMS value. Based on our test, the 100 RMS values given by functions with different fixed parameters in their 1σ uncertainty range are very similar.

7.2.2 Searching for the robust fitter candidate

To minimize the bias, we propose a data-driven method to search for the new robust fitter candidate. Based on the experimental data given at the points of (Q^2, G_C, δG_C) shown in the table 1 from Ref. [46], we can consider fitters with four free parameters and one floating normalization parameter that can be fitted with the high-Q^2 data set given in that table. Besides, in order to control the variance when extracting the radius, at first, two parameters out of those four should be fixed in a fitter, and then it can be used to fit the pseudo-data at low-Q^2 DRad range.

Rational (1,3) is a function with four free parameters that has often been use in the fitting procedure. The fitter function is expressed as

$$f_{\text{Rational}\,(1,3)}(Q^2) \equiv \text{Rational}\,(1,3) = p_0 \frac{1 + a_1 Q^2}{1 + b_1 Q^2 + b_2 Q^4 + b_3 Q^6} \,, \tag{38}$$

where a_1, b_1, b_2, b_3 are free parameters, p_0 is a floating normalization parameter. The Rational (1,3) was used in [48] to fit the proton charge form factor. Compared to the Rational (1,1), it has a good asymptotic behavior not only at $Q^2 \to 0$ but also $Q^2 \to \infty$.

Using this function to fit the data at high-Q^2 region, we determine $b_2 = 0.0416 \pm 0.0152$ and $b_3 = 0.00474 \pm 0.000892$. Then fixing these values for fitting the function in the low-Q^2 DRad range we find

$$\begin{aligned} f_{\text{Fixed\_Rational}\,(1,3)}(Q^2) &\equiv \text{Fixed Rational}\,(1,3) = \\ &= p_0 \frac{1 + a_1 Q^2}{1 + b_1 Q^2 + (0.0416 \pm 0.0152) Q^4 + (0.00474 \pm 0.000892) Q^6}, \end{aligned} \tag{39}$$

where the uncertainties in the fixed parameters are also considered when we calculate the bias in the data-driven method[3]

Now, in order to compare the difference between the Rational (1,1) and FixedRational (1,3) in another range like the Abbott range (from 3×10^{-2} to $1.5\ (\mathrm{GeV/c})^2$) [46],both functions are plotted in the Abbott ranges, where the parameters in these two different fitters are determined by fitting the pseudo-data generated from the two models independently, in the DRad range.

As shown in Fig. 57, both Rational (1,1) and FixedRational (1,3) describe the two Abbott models quite well in the low-Q^2 range. However, at high-Q^2 range, the FixedRational (1,3) describes the models much better than Rational (1,1), which means that FixedRational (1,3) has a better asymptotic behavior in high-Q^2 range.

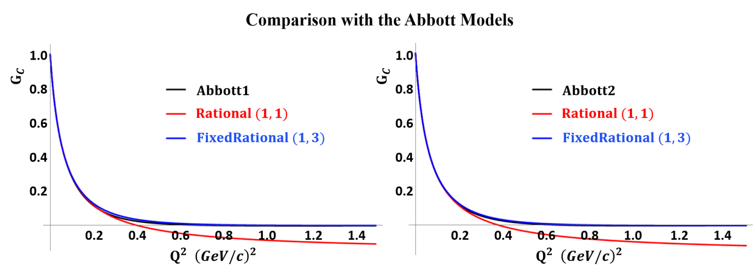

Figure 57: The comparison between the fitters Rational (1,1) and FixedRational (1,3) for the two Abbott deuteron G_C models [46, 47]. Both models are given by the black curve, the Rational (1,1) is given by the red curve, the FixedRational (1,1) is given by the blue curve.

Except for the FixedRational(1,3) function, we had also studied a new functional form which has similar behaviors as the FixedRational(1,3). A detailed study is attached in the Appendix.

7.2.3 Test of the robustness

Smearing procedure After the candidate fitters are found, the robustness for the radius extraction needs to be tested. To mimic different extrapolations in the low-Q^2 region, the parameters in the form factor models can be smeared. Once they are smeared, the functional forms describing the models will be different, and then they will perform different kinds of extrapolation in the low-Q^2 region. Overall, this test is based on a χ^2 test, which consists of the following steps:

A) Smearing of the parameters and calculation of χ^2: First, we smear all the parameters for $\pm 10\%$, following a uniform distribution in Eq. (31) or Eq. (32). Then we generate the corresponding G'_C with respect to its value at the same Q^2 in the (Q^2, G_C, δG_C) data set from the table 1 of Ref. [46]. The

[3]In Eq. (39), the method to consider uncertainties in the fixed parameters is discussed in sections 7.2.1 and A.1.3.

data generation process is the same as in section 7.2.1, but the statistical uncertainty is not added here. Afterwards, we calculate χ^2 by

$$\chi^2 = \sum \frac{(G_C - G'_C)^2}{\delta G_C} \,. \tag{40}$$

B) Checking of the acceptable region: The definition of an acceptable χ^2 region is that the probability of the calculated χ^2 (after the parameters are smeared) with a specific degree of freedom is “acceptable" when it is larger than 99.95% in the χ^2 probability distribution. This requirement restricts the value of χ^2, which means that the smeared model should not be far away from the real experimental data. With the specific degree of freedom ν^2, the χ^2 probability distribution is defined as

$$f(\chi^2) = \frac{1}{2^{\nu/2}\Gamma(\nu/2)} e^{(-\chi^2/2)}(\chi^2)^{(\nu/2)-1} \,. \tag{41}$$

Integrating the function in Eq. (41), from 0 to χ_0^2, will give us the probability for χ_0^2.

For Abbott1 model there are six parameters and twenty two data points used. The degree of freedom is sixteen. 99.95% of χ^2 should be smaller than 41.31. For Abbott2 model there are twelve parameters and nineteen data points used. The degree of freedom is seven. 99.95% of χ^2 should be smaller than 26.02.

If the calculated χ^2 is smaller than the above number for each smeared model, then we keep this smeared model and go to the next step. For each smeared model, there is a new $R_d[\text{input}]$, which is calculated by Eq. (28) with the slope of a smeared model at $Q^2 = 0$. If χ^2 is larger, then we should go to the first step and re-smear the parameters in a given model.

C) Generating pseudo-data: If the smeared models pass the step B), then these models are utilized to generate sets of pseudo-data in the DRad Q^2 range using the binning discussed in section 7.2.1.

D) Fitting and calculating the bias: After the pseudo-data is generated, we use the fitter to fit and obtain $R_d[\text{mean fit}]$.

E) Repeating and obtaining the largest relative bias: In this step the above procedure is repeated 10,000 times to get 10,000 values of relative bias.

To verify that the method discussed in the previous section is applicable and valid, which means that smearing of the parameters can mimic the extrapolation behavior from different deuteron models, the proton form factor G_E models can be used for an additional testing. The studies will be discussed in the appendix.

Fitter		Abbott1	
	RMS (fm)	Bias (fm)	RMSE (fm)
Rational (1,1)	0.00239	0.00287	0.00374
Fixed Rational (1,3)	0.00246	0.00370	0.00445
Fitter		Abbott2	
	RMS (fm)	Bias (fm)	RMSE (fm)
Rational (1,1)	0.00236	0.00352	0.00424
Fixed Rational (1,3)	0.00243	0.00407	0.00474

Table 4: The RMSE obtained from fitting with the pseudo-data generated by the two smeared Abbott deuteron models.

Fitter	Abbott1		
	upper bound	mean	RMS
Rational (1,1)	0.137%	0.109%	0.010%
Fixed Rational (1,3)	0.177%	0.107%	0.021%
Fitter	Abbott2		
	upper bound	mean	RMS
Rational (1,1)	0.169%	0.088%	0.029%
Fixed Rational (1,3)	0.195%	0.091%	0.031%

Table 5: The mean and RMS of the relative bias obtained from fitting with the pseudo-data generated by the two smeared Abbott deuteron models.

7.3 Results and discussion

In Table 15 we have the RMS, bias and RMSE values for using different functions to fit the pseudo-data sets generated from the two deuteron models. The bias is obtained from fitting with pseudo-data generated by following the procedure in section 7.2.3. For the Rational (1,1), we use its fitter function to fit the 10,000 sets of pseudo-data generated by the two smeared Abbott models. For the Fixed Rational (1,3), the values of the parameters are varied in each fit in their 1σ range, following a uniform distribution. Here we use each function with the varied parameters to fit one set of pseudo-data from the 10,000 sets of pseudo-data that we generate in section 7.2.3, and then use the function with different varied parameters to fit another set of the pseudo-data. In total, there will be 10,000 $R_d[fit]$s from this process.

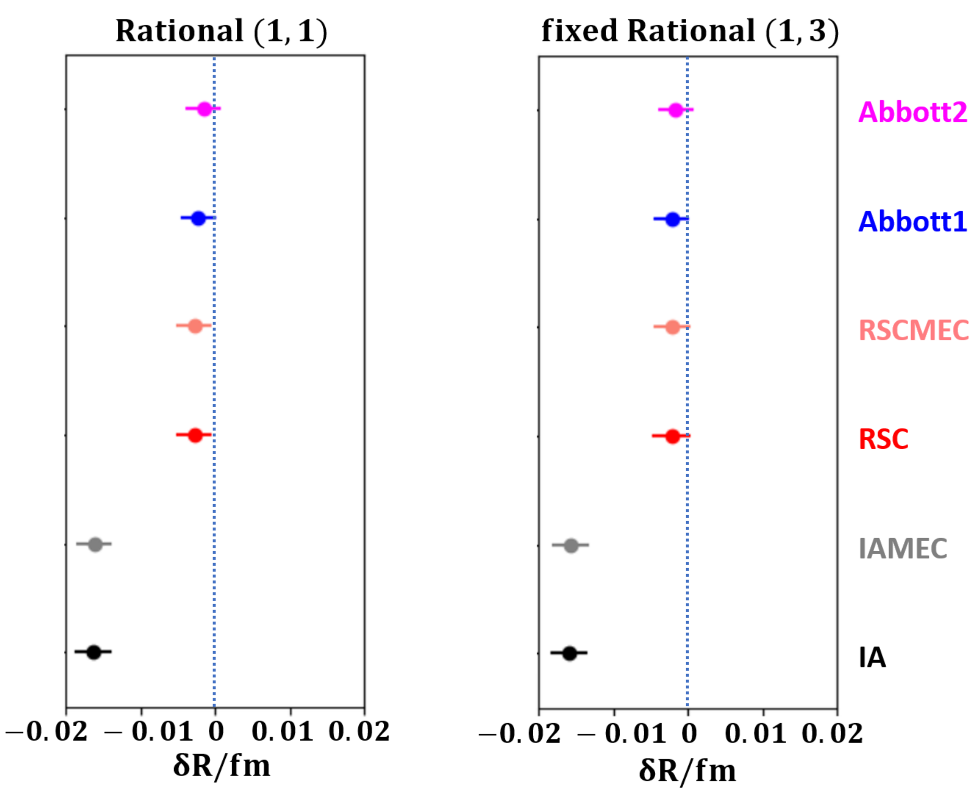

Figure 58: The mean bias and the RMS obtained from fitting the fitters with the pseudo-data (including statistical fluctuations) generated by the six different deuteron models.

The bias in Table 15 is the upper bound in our study. To study the distribution of the bias and determine the effect of the bias in the fitting procedure which related to the systematic uncertainty estimation, the central value and the RMS value of bias distribution is shown in Table 5. From the table, we take the number 0.195% as a conservative upper limit when using the Fixed Rational(1,3) as the fitter. The combination of the mean and RMS value gives us an 1σ range. For example, when we use Fixed Rational(1,3) function to fit the smeared Abbott2 data sets, 68.27% of the bias is within the range 0.060% to 0.122%. As a result, the 1σ range corresponds to 0.062% and the upper bound 0.195% corresponds to a 3σ uncertainty. In the estimation of the effect from the bias in the fitting procedure, we will use 0.65% as the relative systematic uncertainty when we use the Fixed Ratioanal(1,3) function as our primary fitter. Except for the two Abbott's models (the most contemporary parameterizations), we also tested the two fitters with four more models from [74]. As shown in Fig. 58, the two fitters can fit the two Abbott's models and two RSC models quite well, but not the two IA models. Since they are naive models, we do not draw our conclusion based on this result.

8 Radiative corrections for deuteron radius measurements in the DRad setup

In order to reach a high precision in the DRad experiment, in addition to a tight control of systematic uncertainties and a precise knowledge of backgrounds associated with the experiment, a careful calculation of radiative corrections (RC) is necessary. Since in the DRad setup both elastic $e-d$ and Møller $e-e$ scattering events will be taken simultaneously during the experiment, the integrated luminosity is canceled out in the ratio between the two differential cross sections since it is the same for both reaction channels. However, one also needs to take into account that an experimental differential cross section cannot be used directly for a form factor extraction, as it contains radiative effects. To obtain the Born level differential cross section at a particular angle, one needs to apply a precisely calculated RC to the cross section, or approximately calculated/estimated RC as a systematic uncertainty to the cross section. There is a plan to calculate the complete next-to-leading order (NLO) RC in unpolarized elastic $e-d$ scattering [58] beyond ultrarelativistic limit, for which a new $e-d$ event generator will also be made, which will replace the current existing event generator that is based on the soft photon approximation [59].

We refer to the PRad-II proposal where we give more details on the current status of radiative corrections in Møller $e-e$ scatterings for the PRad experimental setup. Here we wish to emphasize that there is also another plan to calculate the NLO and NNLO RC in $e-e$ scattering processes beyond ultrarelativistic limit. These calculations will be based upon a new method, which is under development [60][4]. New results on $e-e$ NLO RC, which will be coming from such a new and independent method, shall be compared with the corresponding results from [61], in order to make sure in robustness of the method before proceeding to calculations of Møller NNLO RC contributions to the cross section.

One should also note that the RC calculations carried out in small scattering angles give radiative correction results that can be quite smaller than corrections obtained from larger angles. Consequently, small angle scattering experiments like DRad/PRad, in this respect have an advantage as compared to larger angle scattering experiments. In [61] such calculations have been performed for a very small scattering angle range of PRad, at $\theta_e = 0.8^\circ - 3.8^\circ$, which corresponds to the Q^2 range of $2 \cdot 10^{-4}$ $(\mathrm{GeV/c})^2 \le Q^2 \le 2 \cdot 10^{-2}$ $(\mathrm{GeV/c})^2$. For DRad, the planned calculations will be carried out at very low scattering angles as well, $\theta_e = 0.7^\circ - 6.0^\circ$, corresponding to $2 \cdot 10^{-4}$ $(\mathrm{GeV/c})^2 \le Q^2 \le 5 \cdot 10^{-2}$ $(\mathrm{GeV/c})^2$.

The common systematic uncertainty of the PRad r_p result from [12, 62] is dominated by the Q^2-dependent uncertainties. In particular, it is dominated by those uncertainties that primarily affect the low Q^2 data points, such as those stemming from the Møller scatterings. These uncertainties include the Møller RC, Møller event selection, beam energy, detector positions, etc. They are introduced into the cross section measurements by the use of the bin-by-bin method, in which one obtains the $e-p$ to $e-e$ ratio by taking the $e-p$ and $e-e$ counts from the same angular bin. In other words, the $e-p$ count in each angular bin gets a different normalization factor from that of the Møller $e-e$ count.

On the other hand, the r_p result is insensitive to the normalization uncertainties, which may shift all data points up or down at the same time. The Q^2-dependent systematic uncertainties on r_p can be eliminated by introducing a floating parameter in the radius extracting fitter. The studies in [44] have already shown that the effect on r_p is nearly zero, even with a normalization uncertainty that is as larger as 5% (ten times larger than the typical normalization uncertainties for PRad). Thus, in order to reduce the systematic uncertainties on r_p, one can rely more on the integrated Møller method rather than on the bin-by-bin method. In this case, one would integrate the Møller counts in a fixed angular range, and use it as a common normalization factor to the $e-p$ counts from all angular bins. This will turn all systematic uncertainties from the Møller into normalization uncertainties on the cross section, and thus completely eliminate any possible effect on r_p. An example is illustrated in Fig. 59, where the $e-p$ to $e-e$ ratios from simulations with different

[4] The current status of the method will be reported in CFNS Ad-Hoc workshop "Radiative Corrections", July 9-10 (2020) at Stony Brook University, NY.

beam energies are plotted relative to those obtained with the nominal beam energy. For the upper plot, the results with scattering angles less than 1.6° are obtained with the bin-by-bin method, while the results with larger scattering angles are obtained with the integrated Møller method. There is a clear Q^2-dependent systematic uncertainty caused by the bin-by-bin method in the forward angular region. On the other hand, for the bottom plot the integrated Møller method is applied for all angular ranges. In this case, the beam energy affects mostly the normalization of the data points. The effect on the extracted r_p will be significantly smaller.

While the integrated Møller method is excellent in eliminating systematic effects on r_p due to the Møller, one would need to correct for the GEM efficiency as well, which can be cancelled by using the bin-by-bin method. This is the reason why the integrated Møller method has not been applied for the full angular range in the PRad case, since the GEM efficiency was very difficult to measure precisely in the forward angular region. This is mostly due to the HyCal finite resolution effect. In the case of PRad there was only effectively a single GEM plane. When measuring the GEM efficiency, the incident angle of the electron was measured by HyCal, the position resolution of which (on the order of 1 mm or worse) was not good enough to resolve various dead areas on the GEM detectors (such as those caused by the GEM spacers). However, if there were the second GEM plane (which is planned to be used by PRad-II and DRad), the incident angle would be determined by it, the position resolution of which is over twenty times better than that of HyCal. This would reduce significantly the finite resolution effect.

Thereby, the procedure described above will be applicable to the DRad experiment as well (by having $e-d$ counts instead of $e-p$ counts), which will give us almost zero RC systematic uncertainty on r_d from the Møller scattering, however, it would be very relevant to obtain such a result from the theory side as well. Given that we wish to obtain total systematic uncertainty 0.25% (or less) for a new planned deuteron radius measurement, one of our priority goals, along with using a zero RC systematic uncertainty on r_d from the integrated Møller method, is to calculate exactly the NLO and NNLO RC in Møller $e-e$ scatterings beyond ultrarelativistic limit, when the electron mass will be taken into account at PRad-II and at DRad beam energies. In this case we will have the Møller radiatively corrected cross sections with both NLO and NNLO RC included. Based upon such new calculations we will also modify the event generator of [63], which has been used in the analysis of the PRad data. Its new version will be used in the analysis of the DRad data, along with the aforementioned new $e-d$ event generator.

It will be an outstanding problem to calculate the corresponding one-loop and two-loop Feynman diagrams systematically. In general, it is highly desirable to develop methods for numerical semi-analytic evaluation of such diagram functions, like Feynman integrals. The problem of studying these integrals is a classic one, on which many papers have been written. However, some very basic questions still remain unanswered. For example, even in the one-loop case the precise representation of fundamental group of the base by a multi-valued function defined by a Feynman integral is unknown [64]. There has been tremendous number of research works accomplished on supersymmetric amplitudes on mass shell, with one of the landmark papers being Ref. [65]. However, it is known that not all amplitudes evaluate to polylogarithms, therefore the subject of elliptic polylogarithms is being intensely studied [66]. On the mathematical side, the structures of flat bundles defined by the Gauss-Manin connection are actively studied [67]. For generic values of parameters, it is known that the Gamma-series are a known tool to construct convergent expansions [68].

However, despite this great progress, these techniques have not been applied to the problem at hand, namely on-shell amplitudes relevant to $e-e$ scatterings. One of the difficulties stems from the fact that these amplitudes need to be evaluated on the mass shell, and thus they are infrared divergent. Also, one needs to have a systematic mapping of the space of kinematic invariants and convergent expansions in a covering of this space by open cylinder domains. Besides, there is a need for a new method to expand dimensionally regulated integrals away from singularties, as well as obtain the asymptotic expansion near the singular locus. Our new method will be based on identification of small parameters in the corresponding domain,

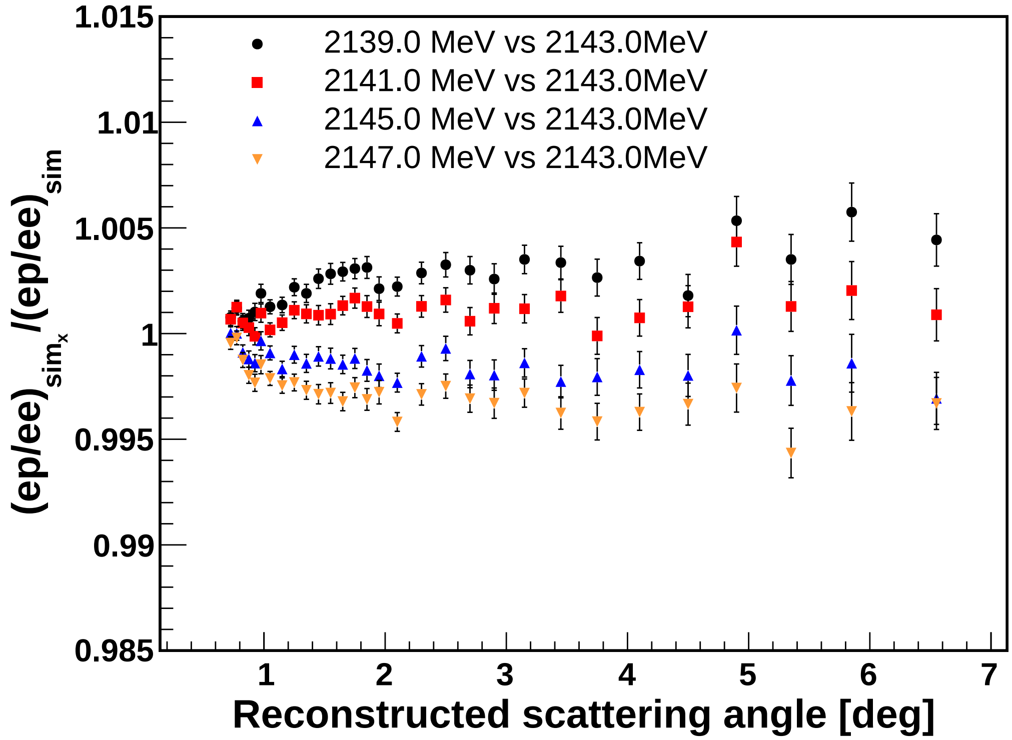

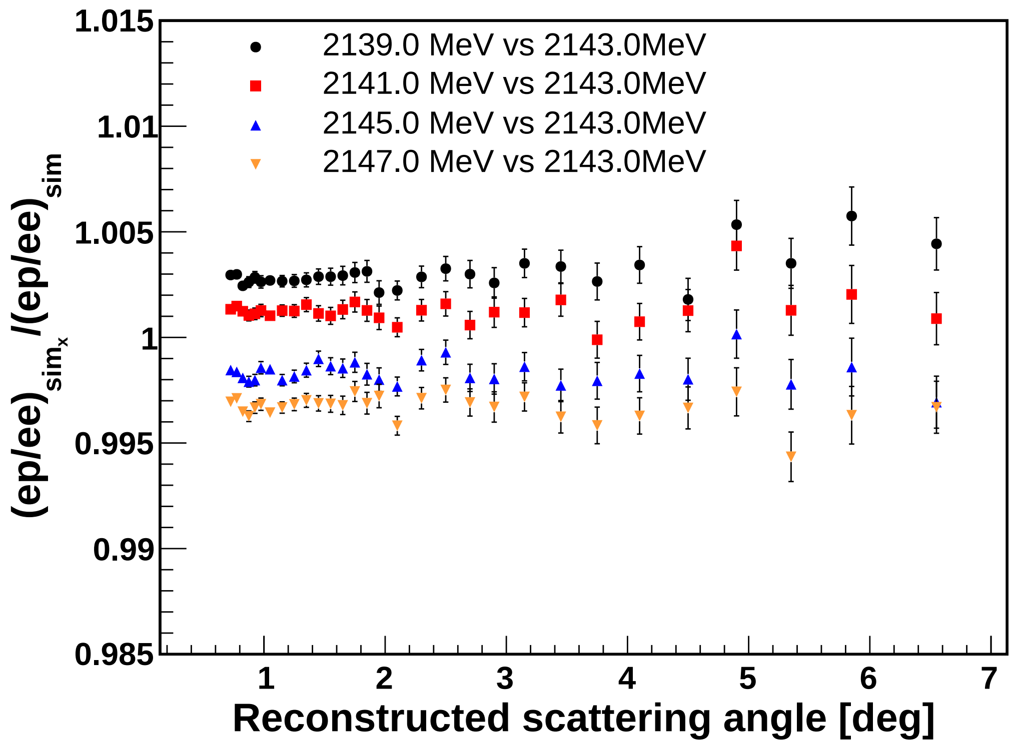

Figure 59: The $e-p$ to $e-e$ ratios from simulations with different beam energies (labeled as sim_x) are plotted relative to those obtained with the nominal beam energy (labeled as sim), for the 2.2 GeV setting. In the upper plot the integrated Møller method is applied for all angular bins above 1.6°. In the lower plot the integrated Møller method is applied for all angular bins.

and on expansion of the integrand into series that are convergent on the chain of integration. The calculated results, namely amplitudes or cross sections, can be represented as power series, for the coefficients of which recursive relations in mathematical literature are available. Infrared regulators will show up as overall factors and will be represented by off-shellness of lines.

9 Rates, beam time, projected uncertainties and results

The full Monte Carlo event sampling program was used to estimate the statistics and event rates for this proposal. As mentioned earlier this program samples both $ed \to ed$ and $e^-e^- \to e^-e^-$ processes according to their differential cross sections and traces the events through the target, vacuum scattering chamber, two GEM detectors and the HyCal calorimeter. The positions and energies of the secondary particles were sampled in GEM and HyCal according to their experimental resolutions described in Secs. 5.4, 5.5.

The deuterium gas target in this experiment will be very similar to the hydrogen gas flow target successfully commissioned and used in the PRad experiment last year. The projected thickness of the target is: $N_{\rm tgt} = 2 \cdot 10^{18}$ deuterium atoms/cm^2. The choice of beam current is based on the expected maximum data rate allowed by the new GEM detector DAQ (25 kHz), the expected trigger rate for the calorimeter and maximum power allowed on the Hall-B Faraday cup (160 W). The Faraday cup is essential for the background subtraction using the empty target data. For the beam energy of 1.1 GeV we plan to use an incident electron beam intensity of $I_{\rm beam} = 30$ nA ($N_e = 1.875 \cdot 10^{11}\ e^-/{\rm s}$). The rates for the $ed \to ed$ elastic events in the experimental setup can be estimated by:

$$N_{ed} = N_e \cdot N_{\rm tgt} \cdot \Delta\sigma \cdot \varepsilon_{\rm geom} \cdot \varepsilon_{\rm det}\ ,$$

where $\Delta\sigma$ is the integrated elastic cross section at forward angles ($\theta_e = 0.7^\circ - 6.0^\circ$), accepted by the setup (1.38×10^{-27} cm^2); $\varepsilon_{\rm geom}$ is the geometrical acceptance of the setup. For these calculations, as a simplification, we assumed that the detection efficiency is $\varepsilon_{\rm det} \approx 1$ and $\varepsilon_{\rm geom} \approx 1$. With all that, the integrated rate of events from the $ed \to ed$ process is:

$$\begin{aligned} N_{ed} &= 1.875 \cdot 10^{11} \cdot 2 \cdot 10^{18} \cdot 1.38 \cdot 10^{-27}\ events/{\rm s} \\ &\simeq 519\ events/{\rm s} \\ &\simeq 44.7{\rm M}\ events/{\rm day}\ . \end{aligned}$$

This is a high integrated statistics per day for the forward angles. However, due to $\sim 1/\sin^4(\theta/2)$ nature of the scattering process, as well as the deuteron form factors, most of these events will be populated in the extreme forward angles ($\theta_e \sim 0.7^\circ$) of our acceptance range. Therefore, in order to achieve a sub-percent level ($\simeq 0.5\%$) statistical uncertainty even for the last Q^2 bin ($\theta_e = 5.95^\circ - 6.00^\circ$), we have to run for 8 days at this $E_0 = 1.1$ GeV energy setting: Therefore, with $I_{\rm beam} = 30$ nA and $N_{\rm tgt} = 2 \cdot 10^{18}$ deuterium atoms/cm^2, eight days of run time will be sufficient to get the required high statistics ($< 0.5\%$) for all Q^2 points including the very last bin, $Q^2 = 1.311 \pm 0.011 \cdot 10^{-2}$ (GeV/c)^2.

$$\begin{aligned} N_{ed}(\theta_e = 5.95^\circ - 6.00^\circ) &= 1.875 \cdot 10^{11} \cdot 2 \cdot 10^{18} \cdot 1.83 \cdot 10^{-31}\ events/{\rm s} \\ &\simeq 0.069\ events/{\rm s} \\ &\simeq 47,490\ events/8\ {\rm days}\ . \end{aligned}$$

The $e^-e^- \to e^-e^-$ Møller cross section is significantly higher than the $ed \to ed$ cross section for the same incident beam energies. Under same experimental conditions (beam intensity and target thickness) the event rate for this process will be:

$$\begin{aligned} N_{e^-e^-}({\rm coin.}) &= 1.875 \cdot 10^{11} \cdot 2 \cdot 10^{18} \cdot 0.68 \cdot 10^{-24} \cdot 0.0048\ e^-e^-/{\rm s} \\ &\simeq 1200\ e^-e^-/{\rm s} \\ &\simeq 103.8{\rm M}\ e^-e^-/{\rm day}\ . \end{aligned}$$

As it was stated earlier, we also request to have a separate run with $E_0 = 2.2$ GeV beam energy to increase the Q^2 range for a more stable fit of the G_{Cd} *vs.* Q^2 to extract the deuteron charge radius. The

Møller cross section is inversely proportional to the beam energy, so we will have twice less cross section with the $E_0 = 2.2$ GeV beam. On the other hand, the geometrical acceptance of the $e^-e^- \rightarrow e^-e^-$ reaction also increases with the energy. With all that, the Møller rate at $E_0 = 2.2$ GeV will be of the same order as for the first energy. For the $ed \rightarrow ed$ elastic scattering process the cross section drops as $1/E^2$ and, therefore, all rates for the 2.2 GeV run will be about four times less than for those at 1.1 GeV. However, the beam current can be increased to 70 nA, the maximum allowed by the power limit on the Hall-B Faraday cup (160 W). Considering all these factors and optimizing the requested beam time, we request 16 days of run time for the $E_0 = 2.2$ GeV beam. This will provide ($< 0.5\%$) statistics even at the highest Q^2 bin.

At the forward electron scattering angles of this experiment, the estimated π^+/e ratio is less than $\sim 10^{-3}$ [69]. For these low hadronic rates the HyCal electromagnetic calorimeter, which has a π/e rejection capability of $\sim 10^{-2}$, makes the hadronic background negligible. Thess estimated were confirmed during the PRad experiment.

Table 6: Beam time request.

	Time (days)
Setup checkout, tests and calibration	3.5
Recoil detector commissioning	2
Recoil detector calibration with hydrogen gas	3
Statistics at 1.1 GeV	8
Energy change	0.5
Statistics at 2.2 GeV	16
Empty target runs	7
Total	40

In summary, we are requesting 8 days of run time for the $E_0 = 1.1$ GeV beam and 16 days for the $E_0 = 2.2$ GeV beam to provide sufficient statistics for the precision extraction of the deuteron charge radius. We will need 3.5 more days for experimental setup checkout, tests and calibration of the GEM/HyCal detectors, 2 days for commissioning and integration of the new Si-strip cylindrical recoil detector. For the calibration of this new recoil detector we need 3 days with hydrogen gas in the target. The energy change from one-pass to two-pass typically requires about half-a-day. To control the experimental background originated from electron beam halo hitting the outside engineering structure of the gas flow target and exclude the background events from the residual beam line gas, we will also need total of 7 days of empty target runs. These runs will be periodically performed during the entire time of the experiment. With that, we are requesting a total of 40 days to perform this experiment and extract the deuteron charge radius with a sub-percent precision.

9.1 Statistical uncertainty

These two processes, $ed \rightarrow ed$ and $e^-e^- \rightarrow e^-e^-$ Møller, that we are aiming to measure simultaneously in this proposed experiment, are the most probable two electromagnetic processes at these very forward angles. Based on the rates estimated in Sec. 9, we expect to have enough statistics within the requested beam time, to provide statistical uncertainties on the level of 0.2% for each Q^2 bin, on average. For the lower Q^2 bins, this number would be significantly less than 0.2%. The statistical uncertainty on the radius is estimated to be 0.11%. With that, the major concern for this type of experiment, is the control of the systematic uncertainties, and their contribution to the final uncertainty of the extracted deuteron charge radius.

9.2 Systematic uncertainties

The estimation of the systematic uncertainty is based on the studies of the PRad experiment, and the simulation with the DRad experimental setup. The combination of the two GEM chambers and the recoil detector can reject most of the beam-line backgrounds, and suppress some dominant systematic items in PRad.

The systematic uncertainties on the radius include all of those that can affect the cross section results, and the assumption about G_M^d and G_Q^d during the extraction of G_C^d which will be discussed in Sec.9.2.1.

A Monte-Carlo technique is used to evaluate the effects of these systematic uncertainties on the radius result. First of all, 10,000 data sets are generated based on the projected DRad cross section results. Then the data points are smeared by the systematic uncertainty sources at once, and a set of G_C^d data points is extracted from each set of the smeared cross section data. Then the extracted G_C^d data sets are fitted separately and a R_d value is extracted from each of these data sets. Lastly, the RMSE value (Eq. 29) of these extracted R_d values was assigned as the systematic uncertainty, where the bias in this calculation is the difference between the mean value R_{sys} obtained from these extracted radius results, and the mean value $R_{central}$ obtained from the extracted radius results including only statistical uncertainties. The relative systematic uncertainty on the radius is $|R_{sys} - R_{central}|/R_{central}$.

9.2.1 The G_M^d and G_Q^d parameterization

In the very low Q^2 region, the e-d elastic scattering cross section is dominated by the charge form factor G_C^d. To verify this assumption, and study the effects due to the selection of different models when extracting G_C^d, one can compare the difference of the radius by selecting different magnetic dipole (G_M^d), and electric quadrupole (G_Q^d), form factors models. By selecting the two deuteron models in [46], we found the model-dependent effects due to the G_M^d and G_Q^d parameterization are negligible.

9.2.2 GEM efficiency

The GEM efficiency is determined from the simulation. The events of interest are first identified using the HyCal and one of the GEM chambers (reference GEM), and the number of events of interest is N_1 (when the first GEM is the reference GEM) or N_2 (when the second GEM is the reference GEM). Then one would search if there are matching hits on the other GEM. If there are, then the hits are counted, and are included in "coincident counts N_{coin}". All the event selection cuts such as the energy of the scattered electron, and the geometrical acceptance of the HyCal are applied in this study.

When there are two GEM chambers, the efficiency of the first GEM chamber is $\epsilon_1 = N_{1coin}/N_2$ and the efficiency of the second GEM chamber is $\epsilon_2 = N_{2coin}/N_1$. The total GEM efficiency is calculated by:

$$\epsilon_{tot} = \epsilon_1 \times \epsilon_2 \tag{42}$$

Statistical uncertainty of the GEM efficiency Assuming that the event selection can be considered as a binomial process, with efficiency ϵ, the statistical uncertainty can be calculated by:

$$\delta\epsilon = \sqrt{\frac{\epsilon(1-\epsilon)}{N}} \tag{43}$$

where N is the number of events of interest in each bin (N_1 or N_2 mentioned above).

By error propagation, the total statistical uncertainty of the GEM efficiency is:

$$\delta\epsilon_{tot} = \epsilon_{tot} \times \sqrt{(\frac{\delta\epsilon_1}{\epsilon_1})^2 + (\frac{\delta\epsilon_2}{\epsilon_2})^2} \tag{44}$$

Based on the study of PRad, after the background subtraction, the statistical uncertainty of the GEM efficiency is 1.1 times larger than the original number. After taking this factor into consideration, at 1.1 GeV beam energy, $\delta\epsilon_{tot}$ in each bin is at the level of 0.02% for θ_e less than 2.1° and up to 0.10% in the last bin; at 2.2 GeV beam energy, $\delta\epsilon_{tot}$ in each bin is smaller than 0.02% when $\theta_e < 2.3°$ and reach 0.10% in the last four bins. Aftering smearing the DRad cross section data sets by these numbers, the effects on the radius is 0.03%.

GEM efficiency correction uncertainty To prevent the GEM foils from direct contact with each other, multiple dielectric spacers are placed in between them. Due to these spacers, there will be "miscounts" on both the two GEM chambers and introduce an uncertainty when calculating the correction of the GEM efficiency. As a result, there will be uncertainty in the reconstructed cross section.

Based on the simulation, when the positions of the spacers on the two GEM chambers are the same, the uncertainty on the reconstructed cross section is as large as 4.4%, which will have a large contribution to the uncertainty on the radius. If the positions of the spacers on one of the GEM chambers shift for X = 50 mm and Y = 40 mm, the result is shown in Fig.60. The fluctuation ratio in the figure represents the expected GEM efficiency correction uncertainty on the cross section. At 1.1 GeV beam energy, the uncertainty on the cross-section in each bin is from 0.04% to 0.14% for θ_e less than 2.6°, and is from 0.002% to 0.03% in larger angular bins; at 2.2 GeV beam energy, the uncertainty on the cross-section in each bin is from 0.001% to 0.05% for θ_e less than $1.8°$, and is from 0.06% to 0.11% in larger angular bins. The GEM efficiency correction uncertainty on the radius is estimated to be 0.075%.

In the PRad experiment, the GEM efficiency is calibrated by HyCal, the precision of the GEM efficiency is limited by the HyCal finite resolution. As shown in Fig.61, when there is only one GEM chamber, the GEM efficiency can only be calibrated by the HyCal, the correction uncertainties in very forward angular bins are very large. Then only the bin-by-bin Møller method can be used in order to cancel these uncertainties when calculating the reconstructed cross section. If the GEM efficiency is calibrated by a second GEM chamber, the precision is greatly improved. In this case, the integrated Møller method is applicable for the full angular range with high precision GEM efficiency measurement. Then those Q^2 dependent uncertainties from the Møller part in other systematic items will only affect the normalization.

Combined the two issues when calculating the effect from the GEM efficiency uncertainty, the influence on the radius is estimated to be 0.08%. According to the latest development of the GEM detector, we may be able to build a new spacerless GEM chamber. In that case, the uncertainty from the GEM efficiency correction will be negligible and the total influence on the radius can be reduced to 0.03%.

9.2.3 Event selection

A series of cuts will be used in the analysis to select the elastic e-d and e-e events, such as the kinematic cuts for both reaction channels, and the coplanarity and vertex-z cuts for the e-e events. The sizes of the cuts applied in the analysis to select the events will induce variations on the cross section.

According to the studies of PRad, the uncertainties for the event selection are dominated by those cuts related to the HyCal reconstructed energy, such as the kinematic cuts. The variation of the kinematic cut leads to changes in the extracted cross section of about 0.1%, on average, and is typically within $\pm 0.15\%$, except for the last few bins in the large angular region. For the co-planarity and vertex-z cuts, the variations are negligible compared to those from the energy cuts.

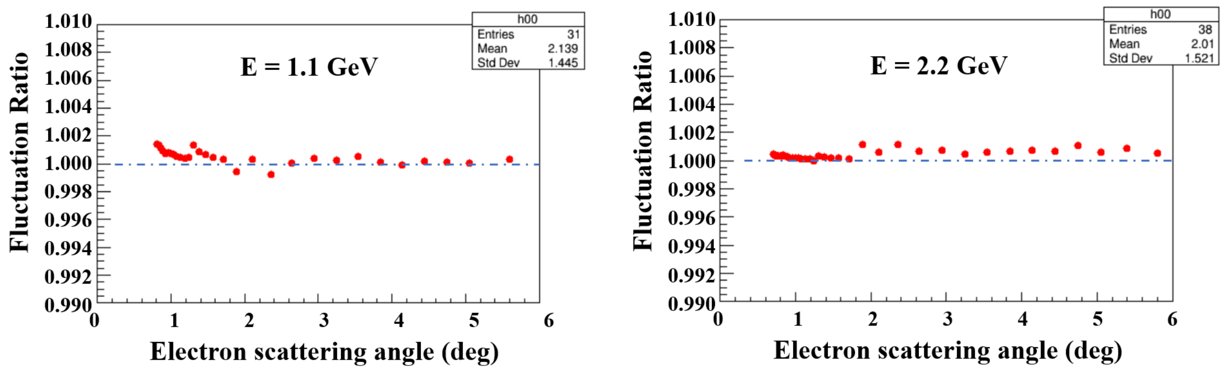

Figure 60: The expected GEM efficiency correction uncertainty on the cross-section when a second GEM chamber is used. At 1.1 GeV beam energy, the uncertainty on the cross-section in each bin is from 0.04% to 0.14% for θ_e less than $2.6°$, and is from 0.002% to 0.03% in larger angular bins; at 2.2 GeV beam energy, the uncertainty on the cross-section in each bin is from 0.001% to 0.05% for θ_e less than $1.8°$, and is from 0.06% to 0.11% in larger angular bins.

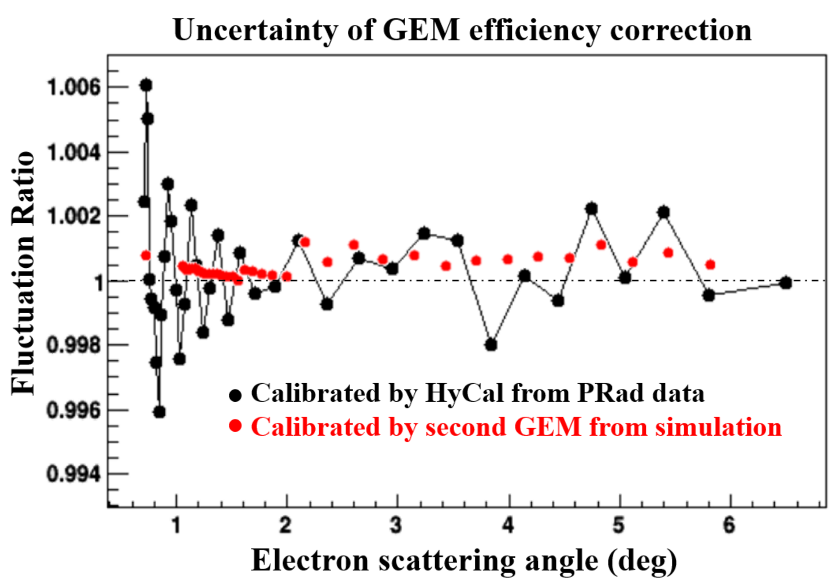

Figure 61: The GEM efficiency correction uncertainty with different calibration methods. When there is only one GEM chamber, the GEM efficiency is calibrated by the HyCal, the correction uncertainties in very forward angular bins are large. If the GEM efficiency is calibrated by a second GEM chamber, the precision is greatly improved.

Based on the above estimations, we assume the effect from the event selection on the DRad cross section is similar to the effect on the PRad cross section in the same angular bin. Also, by the study of the GEM efficiency in Sec.9.2.2, the integrated Møller method is applicable in all the angular range, then the Q^2 dependent uncertainty from the Møller part is removed. The uncertainty from the event selection on the radius is estimated to be 0.11%.

9.2.4 Radiative correction

The radiative correction for both elastic *e-d* and Møller *e-e* scattering is dicussed in Sec. 8. Here we assume that the radiative correction in the e-d elastic scattering is similar to the effect in the e-p elastic scattering. Again, since the integrated Møller method is applicable in all the angular range, the radiative correction from the Møller part will only affect the normalization, but not the radius result. The uncertainty from the radiative correction on the radius is estimated to be 0.09%.

9.2.5 HyCal response

This item is mainly related to the HyCal energy response for an incident particle with different energies (non-linearity). There are a number of factors that can affect the nonlinear behavior of a module, such as the light attenuation, pedestal cuts, back scattering of secondary particles and so on. Still, we assume the uncertainty on the DRad cross section is similar to the uncertainty on the PRad cross section in the same angular bin. Then the effects on the radius is estimated to be 0.09%.

9.2.6 Geometric acceptance

There are two items related to the geometric acceptance:

Detector position This item includes the uncertainties in the detector positions and the beam position. Based on the studies in PRad, for data points obtained using the integrated Møller method, the shifts in the GEM positions mostly just affect the normalization of the data points, at around $\pm 0.05\%$. For the HyCal position, the effect is rather negligible since the HyCal reconstructed coordinates are eventually replaced by the GEM coordinates after matching. Also, the systematic uncertainties related to the tilting angles of the detectors are found to be negligible. Similarly, for the systematic uncertainties due to the beam position is also shown to be negligible. In the end, the systematic uncertainty on radius due to detector position is estimated to be 0.008%.

Acceptance of the recoil detector In this experiment, we have a windowless gas flow target. Since the gas will leak through the 4mm diameter aperture, there will be a gas tail out of the target cell. When the distribution of the gas is not uniform, an uncertainty due to the acceptance of the recoil detector is introduced.

A gas profile based of the study of the PRad experiment is used to simulate a uniform gas distribution inside the target cell, and a distribution of the gas tail out of the target cell. This study compares the radius result $R_{uniform}$ from the simulation with only a uniform gas distribution inside the target cell(which is the perfect case) and the radius result R_{tail} from the simulation with the gas tail distribution. The uncertainty on the radius is the difference between the two results, where the relative uncertainty is calculated by:

$$\frac{\delta R}{R_{uniform}} = \frac{|R_{uniform} - R_{tail}|}{R_{uniform}} \tag{45}$$

Through simulations with different designs of the target cell, we found if the position of the aperture is within the geometric coverage of the recoil detector, the distribution of the gas tail will greatly influence the acceptance and introduce a large uncertainty on the radius. The relative uncertainty on the radius is as large as 0.19%.

By optimization of the target cell, where we extended the length of the target cell to 7.2 cm and moved the recoil detector 1.0 cm downstream, the uncertainty on the radius can be smaller than 0.02%.

9.2.7 Beam energy

In the PRad experiment, the measured beam energy for the 1.1 GeV data set is 1101.0 MeV $\pm$ 0.5 MeV, and 2143.0 MeV $\pm$ 1.5 MeV for the 2.2 GeV data set. The effects due to these systematic uncertainties are determined by running multiple simulations with different beam energies. Here, we also assume the uncertainty on the DRad cross section is similar to the uncertainty on the PRad cross section in the same angular bin. The effect on the deuteron radius is 0.008%.

9.2.8 Inelastic process

The estimation of the uncertainty on the cross section is discussed in Sec. 6.3. After the projected DRad cross section data sets are smeared with those uncertainty values, the uncertainty on the radius due to the contamination of the inelastic process is smaller than 0.024%.

9.2.9 Bias from the fitter

The uncertainty estimation on the radius of this item is discussed in Appendix A.

9.2.10 Recoil detector efficiency

The Si strip recoil detector efficiency will be determined using the deuteron and proton beams from the Tandem accelerator at TUNL. These measurements will be used to form a ratio of the proton to deuteron detection efficiency as a function of energy. During the DRad experiment each $e-D$ run will be interspersed with $e-p$ runs. The $e-p$ runs will be used to monitor the proton detection efficiency of the recoil detector given the over-determined kinematics of $e-p$ scattering. The measured proton detection efficiency along with the ratio of the proton to deuteron detection efficiency measured at TUNL will be used to determine the deuteron detection efficiency. It is projected that the detector efficiency can be determined with 0.15% uncertainty.

9.2.11 Projected uncertainty table

Table 8 is summarizing the estimated relative uncertainties on the radius in this proposed experiment together with the total expected uncertainty of 0.22%. The correlation between event selection, radiative correction, HyCal response, geometric acceptance and beam energy has been studied in the PRad experiment, the combined effect of these terms is determined by smearing all those effects at the same time to extract the radius. The other terms are added in quadrature to obtained the total uncertainty.

Item	Uncertainty (%)
Event selection	0.110
Radiative correction	0.090
HyCal response	0.043
Geometric acceptance	0.022
Beam energy	0.008
Total correlated terms	0.13

Table 7: Projected relative uncertainties on the radius based on the PRad studies.

Item	Uncertainty (%)
Statistical uncertainty	0.05
Total correlated terms	0.13
GEM efficiency	0.03
Inelastic e-d process	0.024
Bias from the fitter	0.065
Efficiency of recoil detector	0.15
Total	0.22

Table 8: Total projected relative uncertainty on the radius.

9.3 Projected Results

Mock data was generated and analyzed as described in Sec. 7 to extract r_D. The projected r_D from the DRad experiment along with other measurements and the CODATA values are shown in Fig. 62.

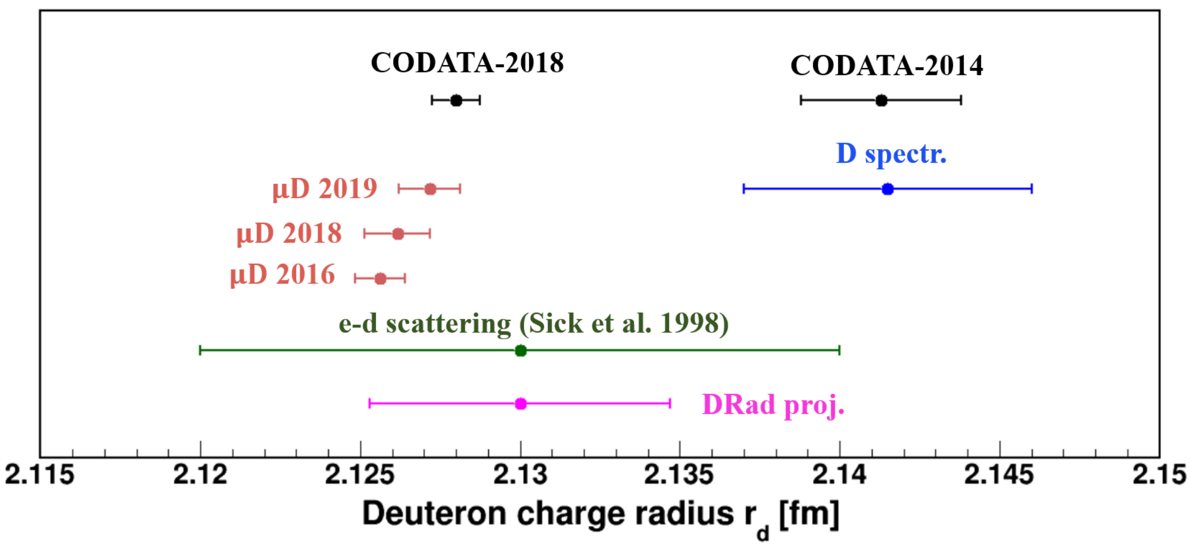

Figure 62: The projected DRad result along with CODATA values and other measurements as described in Fig. 1

10 Related Experiments

In 2014 a new deuteron form factor measurement was carried out at MAMI by the A1 collaboration [70]. This is a magnetic spectrometer based experiment using a liquid deuterium target and covered a Q^2 range of 2.3×10^{-3} - 0.3 $(\mathrm{GeV/c})^2$. The data were collected for 200 different kinematic points over this Q^2 range. The data are still being analyzed and the radius extraction will take place in the near future. A typical missing energy spectrum for this experiment is shown in Fig. 63. The events beyond $\Delta E' = 2.2$ MeV are from deuteron breakup while the events at $\Delta E' < 0$ are from the target cell wall.

The proposed experiment has several advantages compared to MAMI experiment; (1) it will access a value of Q^2 that is one order of magnitude smaller; (2) it will use a windowless gas flow target which avoids large contributions from the cell wall; (3) the detection of the recoil deuteron will help eliminate background from the deuteron breakup; (4) the cross section will be calibrated against a well known QED process. Note that access to the lowest Q^2 achievable is even more critical for the deuteron radius extraction than for the proton.

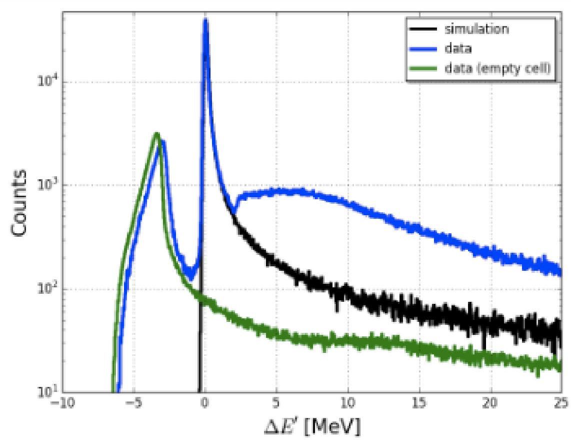

Figure 63: Distribution of elastic ed scattering data (blue) as a function of the $\Delta E' = E'(\theta_e) - E'$, along with simulation (black) and empty target events (green) for $E_e = 315$ MeV and $\theta_e = 23.6°$. The events beyond $\Delta E' = 2.2$ MeV are from deuteron breakup while the events at $\Delta E' < 0$ are from the target cell wall. The figure is reproduced from Ref. [70].

There are also plans at MAMI to build a new "Universal Detector" consisting of a time projection chamber filled with hydrogen or other gaseous light nuclei and a forward tracking detector that can detect recoil fragments in the final state. A research program to measure the cross-section of elastic electron-light-nuclei scattering at low Q^2 with the simultaneous detection of the recoil fragment and the scattered electron with this new Universal Detector was submitted in a letter of intent to the MAMI PAC in 2016 [71]. However, the initial effort will be focused on measuring the electron-proton scattering cross section.

In summary, currently to the best of our knowledge, there are no other experiments planning to measure the deuteron radius at this time.

11 Summary

After about ten years of intense theoretical and experimental efforts there has been remarkable progress towards resolving the well-known *"proton charge radius puzzle"*, but a new controversy has arisen within electron scattering. In addition to this, the same CREMA collaboration at PSI has succeeded in performing new high precision measurements of the deuteron rms charge radius using spectroscopy of muonic deuterium atoms, which demonstrated about 6 σ discrepancy with the radius obtained from spectroscopy of ordinary deuterium atoms and the CODATA-2014 world-average value. This fact created a new *"deuteron charge radius puzzle"* in nuclear and hadronic physics, and the puzzle remains unresolved even after the recent revision of CODATA-2018 world average, which is essentially determined by the muonic result with its unprecedented precision.

We propose to perform a new high precision $ed \rightarrow ed$ elastic cross section measurement at very low scattering angles, $\theta_e = 0.7^\circ - 6.0^\circ$, using the PRad method using the proposed PRad-II experimental setup, to extract the deuteron charge radius with high precision. The proposed experiment will have one major modification compared to PRad-II:

(1) To ensure the elasticity in the ed-scattering process we will add a low energy Si-based cylindrical recoil detector inside the windowless gas flow target cell;

Similar to PRad, in this new experiment the systematic uncertainties in the extracted deuteron charge radius (0.22%) will be controlled by: (1) normalizing the ed cross sections to a well known QED process - Møller scattering; (2) reaching very forward scattering angles for the first time in ed experiments while covering a large enough Q^2 range ($2 \cdot 10^{-4} - 5 \cdot 10^{-2}$ $(\mathrm{GeV/c})^2$) for the extraction of the slope in deuteron charge form factor - G_{Cd}; (3) measuring the cross section over the large Q^2 range in a single setting of the experimental setup; (4) reducing the experimental background typical for all previous $ed \rightarrow ed$ experiments by using a windowless, low density deuterium gas flow target, together with a new cylindrical Si-strip recoil detector.

With that, we request 40 days of beam time in Hall B to extract the deuteron charge radius with a 0.22% total uncertainty to address the *"deuteron charge radius puzzle"* in nuclear and hadronic physics.

References

[1] P. J. Mohr, B. N. Taylor, D. B. Newell, Rev. Mod. Phys. **84**, 1527 (2012).

[2] R. Pohl, *et al.*, Nature **466**, 213 (2010).

[3] A. Antognini, *et al*, Science **339**, 417 (2011).

[4] R. Pohl, *et al.*, Science **353**, 669 (2016).

[5] R. Phol, R. Gilman, G. A. Miller, K. Pachucki, Ann. Rev. Nuc. Part. Sci. **63**, 175 (2013).

[6] C. E. Carlson, Prog. Part. Nucl. Phys. **82**, 59 (2015).

[7] A. Huber, *et al.*, Phys. Rev. Lett. **80**, 468 (1998).

[8] C. G. Parthey, *et al.*, Phys. Rev. Lett. **104**, 233001 (2010).

[9] U. D. Jentschura, *et al.*, Phys. Rev. A **83**, 042505 (2011).

[10] R. Pohl, *et al.* Metrologia **54**, L1 (2017).[arXiv:1607.03165].

[11] I. Sick and D. Trautmann, Nucl. Phys. A **637**, 559 (1998).

[12] W. Xiong *et al.*, Nature **575**, 147 (2019).

[13] C. W. Wang Int. Jour. Mod. Phys. E **3**, 821 (1994).

[14] D. Dricky and L. Hand, Phys. Rev. Lett. **9**, 521 (1962).

[15] M. .N. Rosenbluth, Phys. Rev. **79**, 615 (1950).

[16] V. Z. Jankus, Phys. Rev. **102**, 1586 (1956).

[17] M. Gourdin, Nuo. Cim. **28**, 533 (1963); **32**, 493 (1964).

[18] J. A. McIntyre and S. Dhar, Phys. Rev. **106**, 1074 (1957).

[19] G. H ohler *et al.*, Nucl. Phys. B **114**, 505 (1976).

[20] G. G. Simon, Ch. Schmitt and V. H. Walther, Nucl. Phys. A **364**, 285 (1981).

[21] L. Koester, W. Nistler and W. Waschkowski, Phys. Rev. Lett. **36**, 1021 (1976).

[22] R. W. Berard *et al.*, Phys. Lett. B **47**, 355 (1973).

[23] S. Platchkov *et al.*, Nucl. Phys. A **510**, 740 (1990).

[24] G. G. Simon, Ch. Schmitt, F. Borkowski and V. H. Walther, Nucl. Phys. A **333**, 381 (1980).

[25] A. Bachmann, H. Henning and P. U. Sauer, Few Body Syst. **21**, 149 (1996).

[26] T. Herrmann and R. Rosenfelder, Eur. Phys. J. A**2**, 29 (1998).

[27] B. Desplanques, Phys. Lett. B **203**, 200 (1988).

[28] I. Sick and D. Trautmann, Phys. Lett. B **375**, 16 (1996).

[29] J. L. Friar, J. Martorell and D. W. L. Sprung, Phys. Rev. A **56**, 5173 (1997).

[30] K. Pachucki *et al.*, J. Phys. B **29**, 177 (1996).

[31] G. W. Erickson and D. R. Yennie, Ann. Phys. **35**, 271 (1965).

[32] T. Udem, Ph.D. thesis, *Ludwig-Maximilians Universit at*, Munich, Germany (1997).

[33] M. Weitz, F. Schmidt-Kaler and T. W. H ansch, Phys. Rev. Lett. **68**, 1120 (1992).

[34] A. Huber, *et al.*, Phys. Rev. Lett. **80**, 468 (1998).

[35] C. G. Parthey, *et al.*, Phys. Rev. Lett. **104**, 233001 (2010).

[36] U. D. Jentschura *et al.*, Phys. Rev. A **83**, 042505 (2011).

[37] I. Akushevich, H. Gao, A. Ilyichev and M. Meziane, EPJA **51**, 1 (2015).

[38] PrimEx Conceptual Design Report, 2000 (`http://www.jlab.org/primex/`).

[39] I. Larin *et al.*, (PRIMEX Collaboration), Phys. Rev. Lett. **106**, 162303 (2011).

[40] CLAS12 Technical Design Report, 2008 (`https://www.jlab.org/Hall-B/clas12_tdr.pdf`).

[41] CLAS12 Detector documentation (`http://clasweb.jlab.org/clas12offline/docs/detectors/html/svt/introduction.html`).

[42] NIST Standard Reference Database 124, M.J. Berger, J.S. Coursey, M.A. Zucker and J. Chang, NISTIR 4999 (2017). DOI:10.18434T4NC7P

[43] M. Kubantsev *et al.*, AIP Conf. Proc. **867**, 51 (2006).

[44] X. Yan *et al.*, Phys. Rev. C **98**, no. 2, 025204 (2018).

[45] M. Garcon and J. W. Van Orden, Adv. Nucl. Phys. **26**, 293 (2001).

[46] D. Abbott *et al.*, Eur. Phys. J A **7**, 421 (2000), `http://irfu.cea.fr/dphn/T20/Parametrisations/`.

[47] A. P. Kobushkin and A. I. Syamtomov, Phys. Atom. Nucl. **58**, 1477 (1995) [Yad. Fiz. **58N9**, 1565 (1995)].

[48] J. J. Kelly, Phys. Rev. C **70**, 068202 (2004).

[49] S. Venkat, J. Arrington, G. A. Miller and X. Zhan, Phys. Rev. C **83**, 015203 (2011).

[50] J. Arrington, Phys. Rev. C **69**, 022201 (2004).

[51] J. Arrington and I. Sick, Phys. Rev. C **76**, 035201 (2007).

[52] Z. Ye, J. Arrington, R. J. Hill and G. Lee, Phys. Lett. B **777**, 8 (2018).

[53] J. M. Alarcón and C. Weiss, Phys. Rev. C **96**, no. 5, 055206 (2017).

[54] J. M. Alarcón and C. Weiss, Phys. Rev. C **97**, 055203 (2018).

[55] J. M. Alarcón and C. Weiss, Phys. Lett. B **784**, 373 (2018).

[56] J. C. Bernauer *et al.* [A1 Collaboration], Phys. Rev. C **90**, no. 1, 015206 (2014).

[57] C. D. Robert *et al.*, TBD.

[58] I. Akushevich, *et al.*, private communication.

[59] C. Gu, "*e-d event generator*", Department of Physics, Duke University (2017).

[60] S. Srednyak, *et al.*, private communication.

[61] I. Akushevich, H. Gao, A. Ilyichev and M. Meziane, Eur. Phys. J. A **51**, 1 (2015).

[62] W. Xiong, "*A High Precision Measurement of the Proton Charge Radius at JLab*", PhD Thesis, Department of Physics, Duke University (2020).

[63] C. Peng, "*PRadAnalyzer Package*", Department of Physics, Duke University (2017), `https://github.com/JeffersonLab/PRadAnalyzer`

[64] Z. Bern, L. J. Dixon, F. Febres Cordero, S. Höche, H. Ita, D. A. Kosower, D. Maître and K. J. Ozeren, J. Phys. Conf. Ser. **523**, 012051 (2014).

[65] N. Arkani-Hamed, J. L. Bourjaily, F. Cachazo, A. B. Goncharov, A. Postnikov and J. Trnka, "*Grassmannian Geometry of Scattering Amplitudes*", [arXiv:1212.5605 [hep-th]].

[66] L. Adams and S. Weinzierl, "*On a class of Feynman integrals evaluating to iterated integrals of modular forms*", [arXiv:1807.01007 [hep-ph]].

[67] H. Takayuki, N. Kenta and N. Takayama, Adv. in Math. **306**, 303 (2017).

[68] M. Saito, B. Sturmfels and N. Takayama, "*Gröbner Deformations of Hypergeometric Differential Equations*", Springer 2000.

[69] A. Gasparian, M. Khandaker, H. Gao, and D. Dutta, JLAB Experiment E12-11-106 (2011) (`http://www.jlab.org/exp_prog/proposals/11/PR12-11-106.pdf`).

[70] B. S. Schlimme *et al.* EPJ Web of Conference, **113**, 04017 (2016).

[71] A. A. Vorobyov. Letter of intent for high precision measurement of the ep elastic cross section at small Q^2. 2016.

[72] M. Christy and P. E. Bosted, Phys. Rev. C **81**, 055213 (2010) doi:10.1103/PhysRevC.81.055213 [arXiv:0712.3731 [hep-ph]].

[73] F. Gross, "Relativistic quantum mechanics and field theory," Wiley, New York, NY, 1993.

[74] E. Hummel and J. Tjon, Phys. Rev. C **49**, 21-39 (1994) doi:10.1103/PhysRevC.49.21 [arXiv:nucl-th/9309004 [nucl-th]].

A More studies on advanced extraction of the deuteron charge radius

A.1 Searching for the robust fitter candidate

Except for the FixedRational(1,3) function, we also studied a modified modified rational function of the following form:

$$f_{\text{modified,Rational (1,1)}}(Q^2) = p_{0,1}\frac{\left(1+p_1^{(a')}Q^2\right)^A}{\left(1+p_1^{(b')}Q^2\right)^B}, \tag{46}$$

which is a modification of the Rational (1,1) function. $p_{0,1}$ is the floating normalization parameter, $p_1^{(a')}$ and $p_1^{(b')}$ are the free fitting parameters. The powers A and B will be given and fixed by different methods. The radius is calculated by $R_d = \sqrt{6\left(B{\cdot}p_1^{(b')} - A{\cdot}p_1^{(a')}\right)}$.

A.1.1 Model-dependent method

To search for the best combination of A and B in Eq. (46), a scanning method is used. In this case A and B are varied (each) from 0 to 10 with the step equal to 0.1, in order to fit the non-smeared pseudo-data generated by the two models in the DRad range (from $2{\cdot}10^{-4}$ to $5{\cdot}10^{-2}$ $(\mathrm{GeV/c})^2$). Based on this method, for A = 3.0 - 4.2 and B = 0.8, the relative bias is smaller than 0.025%, such that the modified Rational (1,1) becomes as

$$f_{\text{modified,Rational (1,1)}}(Q^2) \equiv \text{modRational }(1,1) = p_{0,1}\frac{\left(1+p_1^{(a')}Q^2\right)^{3.0-4.2}}{\left(1+p_1^{(b')}Q^2\right)^{0.8}}, \tag{47}$$

Now, in order to compare the difference between the Rational (1,1) and modRational (1,1) in another range like the Abbott range (from 3×10^{-2} to 1.5 $(\mathrm{GeV/c})^2$) [46], we pick up A = 3.4 as an example, and fix B = 0.8 in the modRational (1,1). Then both functions are plotted in the Abbott ranges, where the parameters in these two different fitters are determined by fitting the pseudo-data generated from the two models independently, in the DRad range.

As shown in Fig. 64, both Rational (1,1) and modRational (1,1) describe the two Abbott models quite well in the low-Q^2 range, while the modRational (1,1) gives smaller bias. However, at high-Q^2 range, the modRational (1,1) describes the models much better than Rational (1,1).

A.1.2 Data-driven method

The previous method is highly model-dependent, which is also limited by the number of the given models. In that case the fewer the models are, the higher the model dependency is. To avoid this issue, we have also tried a data-driven method. Based on the experimental data given at the points of (Q^2, G_C, δG_C) shown in the table 1 from Ref. [46], we can consider fitters with four free parameters and one floating normalization parameter that can be fitted with the high-Q^2 data set given in that table. Besides, in order to control the variance when extracting the radius, at first, two parameters out of those four should be fixed in a fitter, and then it can be used to fit the pseudo-data at low-Q^2 DRad range.

For the modRational (1,1) in Eq. (46), when A and B are also considered as free parameters, in that case there are four parameters in this fitter function. We use this function to fit the data at high-Q^2 region, by which we obtain A = 3.48668 $\pm$ 0.01568 and B = 0.75600 $\pm$ 0.11313, then fix these values for fitting the

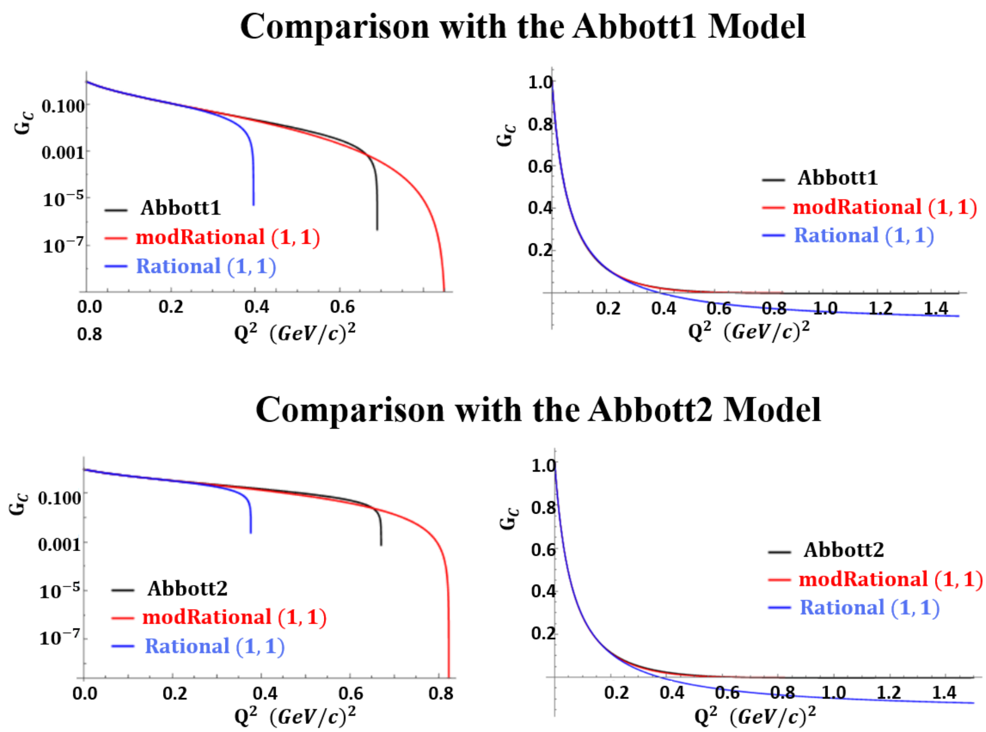

Figure 64: The comparison between the fitters Rational (1,1) and modRational (1,1) (with A = 3.4 and B = 0.8) for the two Abbott deuteron G_C models [46, 47]. Both models are given by the black curve, the Rational (1,1) is given by the blue curve, the modRational (1,1) is given by the red curve. The left plots show the log scale of the same linear plots on the right.

function in the low-Q^2 DRad range. And here is the result given by:

$$f_{\text{Fixed\_modified,Rational}\,(1,1)}(Q^2) \equiv \text{Fixed modRational}\ (1,1) = p_{0,1}\frac{\left(1+p_1^{(a')}Q^2\right)^{3.48668\pm0.01568}}{\left(1+p_1^{(b')}Q^2\right)^{0.75600\pm0.11313}}\ , \quad (48)$$

where the uncertainties in the fixed parameters are also considered when we calculate the bias in the data-driven method[5]

A.1.3 Calculation of the bias

There are two different bias types we calculate:

A) Non-smeared bias. The non-smeared bias is the bias obtained from fitting with pseudo-data generated by the two non-smeared Abbott models. In this case, there are only two sets of pseudo-data, which correspond to the central value generated by the two models. For the modRational (1,1), we fix B = 0.8, and use A from 3.0 to 4.2 with a step 0.1 to fit the pseudo-data. In this case, we use thirteen different modRational (1,1) fitter functions to fit the same sets of pseudo-data independently, and get different bias with different values of A. For the Fixed Rational (1,3) (Eq.(39)) and the Fixed modRational (1,1) (Eq.(48)) with uncertainties

[5] In Eq. (48) and Eq. (39), the method to consider uncertainties in the fixed parameters is discussed in sections 7.2.1 and A.1.3.

Fitter	Abbott1		Abbott2	
	non-smeared	smeared	non-smeared	smeared
Rational (1,1)	0.106%	0.137%	0.077%	0.169%
modRational (1,1)	0.013%	0.070%	0.024%	0.079%
Fixed Rational (1,3)	0.144%	0.177%	0.120%	0.195%
Fixed modRational (1,1)	0.164 %	0.228%	0.180%	0.230%

Table 9: The relative bias obtained from fitting the four discussed fitters with pseudo-data generated by the non-smeared and smeared deuteron (Abbott1 and Abbott2) G_C models.

in the fixed parameters, the values of the parameters are varied in each fit in their 1σ range, following a uniform distribution. Then we use 10,000 such functions with different varied parameters to fit the same sets of pseudo-data and get 10,000 $R_d[fit]$s.

B) Smeared bias. The smeared bias is the bias obtained from fitting with pseudo-data generated by following the procedure in section 7.2.3. For the Rational (1,1), we use its fitter function to fit the 10,000 sets of pseudo-data generated by the two smeared Abbott models. For the modRational (1,1), we again fix B = 0.8, and use A from 3.0 to 4.2 with a step 0.1 to fit the pseudo-data. In this case, as above, we use thirteen different functions to fit 10,000 sets of pseudo-data independently. For the Fixed Rational (1,3) and the Fixed modRational (1,1), the values of the parameters are varied in each fit in their 1σ range, following a uniform distribution. Here we use each function with the varied parameters to fit one set of pseudo-data from the 10,000 sets of pseudo-data that we generate in section 7.2.3, and then use the function with different varied parameters to fit another set of the pseudo-data. In total, there will be 10,000 $R_d[fit]$s from this process.

The relative bias values from different fitter candidates before and after smearing are given in Table 9. For all the fitters, the bias shown in the table is the largest number among the calculated bias distributions, in which case we take it as an upper limit. In our test, the bias value is stable with the repetition procedure mentioned above. As shown in Table 9, when the Rational (1,1) is used as a fitter, the relative bias can be as large as 0.169%. For the modRational (1,1), we tested the different combinations for A from 3.0 to 4.2 and B = 0.8, with the results shown in Table 10. The relative bias is stable inside this range and controlled within 0.079%. However, the two fitters based on the data-driven method give a larger bias compared to the Rational (1,1). This result is within our expectations. As the data-driven method only has constraints from data points in a higher Q^2 range, when it is used to fit the pseudo-data in a lower Q^2 range, its extrapolation may not be very accurate. Moreover, the uncertainties of the parameters in the fitters may also increase the bias.

On the other hand, the model-dependent method can be suitable only if the nature is close to the two parameterization models we tested. Regardless of which method we used for searching for the robust fitter, the best fitter in these studies may or may not exactly describe the true function in the low Q^2 range proposed for the DRad experiment. Note that the numbers shown in Table 9 can not show that the model-dependent method is better than the data-driven method, since the calculation of the bias is also partially model-dependent. Here we just show how the different fitters can control the bias by fitting the pseudo-data within a reliable range.

In order to show the overall ability of different fitters for controlling the bias, its mean and RMS values are also calculated (being the central value and root-mean-square value from the distribution of the 10,000 relative bias values calculated in section A.1.3). The mean value of the bias distribution combined with its RMS value are shown in Table 11 and Table 12. Based on this, overall, all the fitters have a good ability to control the bias.

A	Abbott1		Abbott2	
	non-smeared	smeared	non-smeared	smeared
3.0	0.002%	0.054%	0.024%	0.073%
3.1	0.001%	0.056%	0.022%	0.071%
3.2	0.001%	0.057%	0.020%	0.069%
3.3	0.002%	0.059%	0.019%	0.068%
3.4	0.004%	0.061%	0.017%	0.070%
3.5	0.005%	0.062%	0.016%	0.071%
3.6	0.007%	0.063%	0.014%	0.072%
3.7	0.008%	0.065%	0.013%	0.074%
3.8	0.009%	0.066%	0.012%	0.074%
3.9	0.010%	0.067%	0.011%	0.076%
4.0	0.011%	0.068%	0.010%	0.077%
4.1	0.012%	0.069%	0.009%	0.078%
4.2	0.013%	0.070%	0.008%	0.079%

Table 10: The comparison of the relative bias values for the modRational (1,1) fitter function, with different A and already fixed B.

Fitter	Abbott1		
	upper bound	mean	RMS
Rational (1,1)	0.137%	0.109%	0.010%
modRational (1,1)	0.070%	0.022%	0.015%
Fixed Rational (1,3)	0.177%	0.107%	0.021%
Fixed modRational (1,1)	0.228%	0.062%	0.046%

Table 11: The mean and RMS of the relative bias obtained from fitting with the pseudo-data generated by the Abbott1 smeared deuteron model.

Fitter	Abbott2		
	upper bound	mean	RMS
Rational (1,1)	0.169%	0.088%	0.029%
modRational (1,1)	0.079%	0.020%	0.014%
Fixed Rational (1,3)	0.195%	0.091%	0.031%
Fixed modRational (1,1)	0.230%	0.065%	0.049%

Table 12: The mean and RMS of the relative bias obtained from fitting with the pseudo-data generated by the Abbott2 smeared deuteron model.

A.2 Proof of the robustness test

To verify that the method discussed in the previous section is applicable and valid, which means that smearing of the parameters can mimic the extrapolation behavior from different deuteron models, the proton form factor G_E models can be used for an additional testing.

Here, seven proton parameterization models have been used, including *Kelly* [48], *Arrington1* [49], *Arrington2* [50], *Arrington-Sick* [51], *Ye* [52], *Alarcon* and *Bernauer-2014*, where the *Alarcon* model is our refit based on [53, 54, 55], and the *Bernauer-2014* model is our refit of data from [56]. From the robustness studies of R_p, the largest bias for Rational (1,1) comes from fitting the pseudo-data generated by the *Ye* model, which is 0.476 %. Meanwhile, we can also smear the parameters in the other proton G_E models, to test whether the smearing method can mimic the extrapolation behavior from those models.

Following the same steps shown in the previous section, the bias values obtained from fitting the Rational (1,1) with pseudo-data generated by the above G_E models, before and after smearing, have been determined and are shown in Table 13. The smeared band in each model is shown in Fig. 65.

Model	non-smeared	smeared
Kelly	0.002 %	0.007 %
Arrington1	0.005 %	0.028 %
Arrington2	0.009 %	0.019 %
Arrington-Sick	0.001 %	0.012 %
Alarcon	0.166 %	1.091 %
Ye	0.476 %	0.621 %
Bernauer-2014	0.271 %	0.515 %

Table 13: The relative bias obtained from fitting the Rational (1,1) with pseudo-data generated by the non-smeared and smeared proton G_E models.

By smearing all the parameters for $\pm 10\%$ and restricting the value of χ^2, all the models and the PRad data are covered by most of the smeared bands, except for the Arrington-Sick model, as shown in Fig. 65. The relative bias coming from the Rational (1,1) fitted with the pseudo-data generated by the smeared models shows how the fitter can control the bias with the data inside a band. One smeared model can not precisely mimic the other models, but it can generate a reasonable range for testing, to see whether the fitter can handle the pseudo-data with different kinds of extrapolation. As shown in Table 13, all the relative bias values obtained from the smeared models get closer to or even exceed the largest bias (0.476% from the *Ye* model) obtained from the non-smeared models. Moreover, in the PRad data analysis, we take this number as an upper bound rather than a reasonable 1σ uncertainty contributed to the total uncertainty. Hence, there is no need to obtain the bias (after smearing) to be as large as 0.476% in order to imitate different extrapolations to low-Q^2 regions.

Through these studies, we found that the parameter smearing method in form factor models can help us better calculate the bias, considering different extrapolations to low-Q^2, when the number of the models can also be limited.

A.3 Similarity of the modRational (1,1) and Rational (1,3) fitters

The modRational (1,1) fitter discussed in the section A.1.1 still lacks a clear physical meaning. Meanwhile, one can show that the modRational (1,1) is actually similar to the Ratioanl (1,3), by starting with the fitted modRational (1,1) for generating a set of G_C pseudo-data, and then using the Rational (1,3) for fitting this set of pseudo-data. We can now show how one can do it, and how the similarity between the two fitters can be observed.

(i) The modRational (1,1) with A = 3.4 and B = 0.8 from Eq. (47) is used to fit pseudo-data generated by the Abbott1 model [46]. The fitted function is the following:

$$\mathrm{modRational}\,(1,1) = \frac{\left(1 - 0.0456785\,Q^2\right)^{3.4}}{\left(1 + 0.718695\,Q^2\right)^{0.8}}\,, \tag{49}$$

where the dimension of Q^2 is in fm^{-2}.

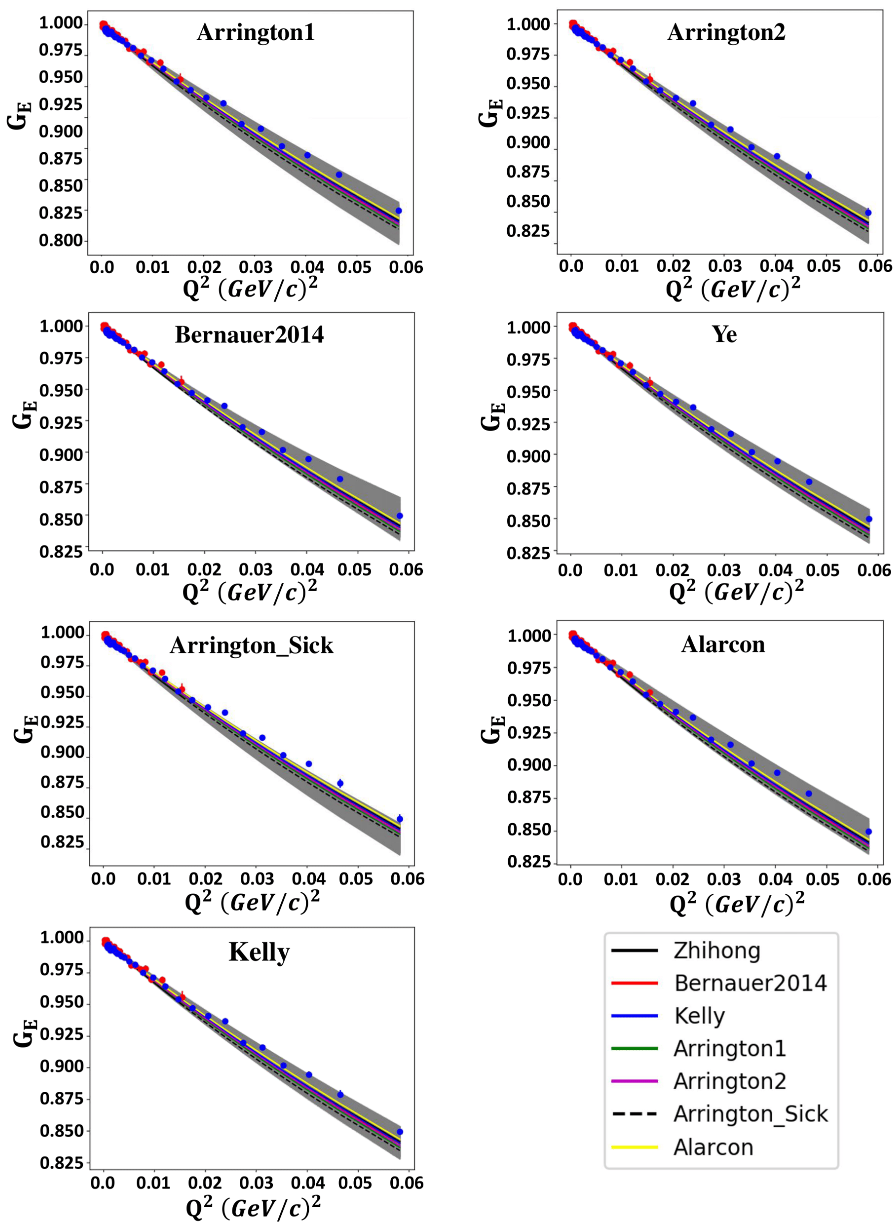

Figure 65: The proton electric form factor G_E models vs. Q^2. The grey bands are the smeared bands generated by each model. The red points are the PRad 1.1 GeV data, the blue points are the PRad 2.2 GeV data.

(ii) To generate a set of G_C pseudo-data with reasonable bins and uncertainties, we choose both the DRad binning with its simulated uncertainty and the Abbott binning from the table 1 of Ref. [46]. In total, there are eighty-two pseudo-data points that are generated by Eq. (49) in the range of Q^2 = 0.006 - 21.344 fm^{-2}.

(iii) Afterwards, the Rational (1,3) function as shown in Eq. (38) is used to fit those pseudo-data.

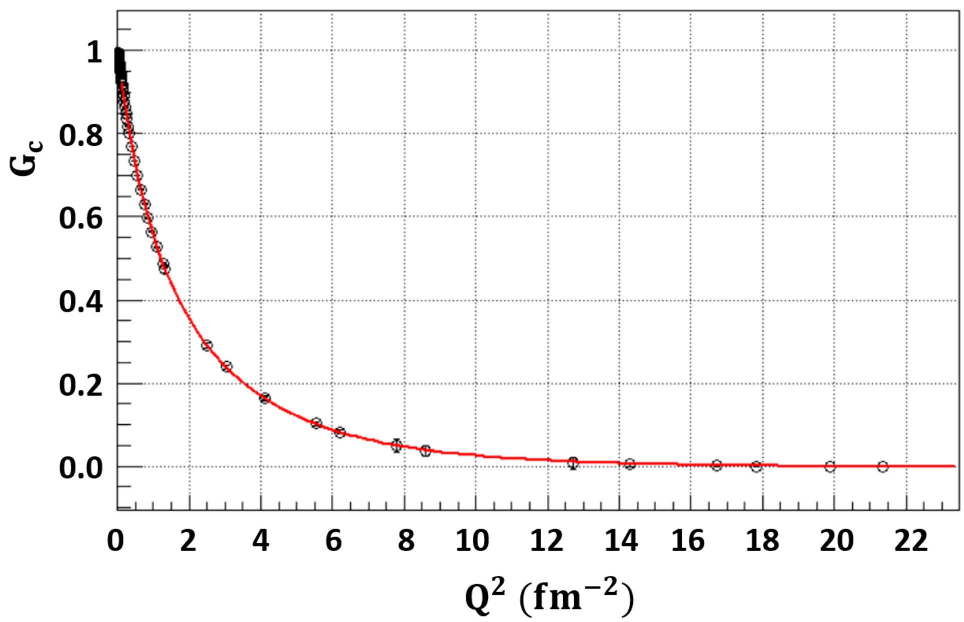

Figure 66: The Rational (1,3) fitting with the pseudo-data generated by Eq. (49).

Fulfilling the above steps, we present the final result in Fig 66, where the black points are the pseudo-data points generated by Eq. (49), the red curve is the fitted Rational (1,3). The value of the fitting parameters are: $a_1 = -0.05107 \pm 0.00216, b_1 = 0.67910 \pm 0.00283, b_2 = 0.02786 \pm 0.00397, b_3 = 0.00832 \pm 0.00130$. The plot shows that the modRational (1,1) has a very similar behavior as the Rational (1,3) in the range of $Q^2 < 21.5\ \mathrm{fm}^{-2}$ or equivalently of $Q^2 < 0.84\ (\mathrm{GeV/c})^2$.

To compare this new fitted Rational (1,3) with the modRational (1,1), the parameters b_2 and b_3 can be now fixed, as shown in Eq. (50). Then one can use the procedure as discussed in section 7.2.3, by which we calculate the relative bias using the non-smeared and smeared deuteron models.

$$\begin{aligned}&\mathrm{New\ Fixed\ Rational}\ (1,3) = \\ &= p_0 \frac{1 + a_1 Q^2}{1 + b_1 Q^2 + (0.02786 \pm 0.00397) Q^4 + (0.00832 \pm 0.00130) Q^6}\,,\end{aligned} \tag{50}$$

As shown in Table 14, the bias values are similar for the New Fixed Rational (1,3) and modRational (1,1) in the smeared case, which indicates the similarity between these two fitter functional forms.

A.4 Discussion and summary

As shown in Table 11 and Table 12, the four fitters show a good control of the bias. One can also visually compare the overall robustness of the R_d extraction based on the fitters from Table 9, which can be seen in Fig. 67. The plots there show the absolute mean bias (in units of fm) from its relative values in Table 11

Fitter	Abbott1		Abbott2	
	non-smeared	smeared	non-smeared	smeared
modRational (1,1)	0.013%	0.070%	0.024%	0.079%
New Fixed Rational (1,3)	0.052%	0.074%	0.030%	0.098%

Table 14: The comparison of the relative bias values for the functional forms in the table.

and Table 12, and the RMS obtained from fitting those four fitters with pseudo-data (including statistical fluctuations only) generated by the non-smeared Abbott1 and Abbott2 deuteron models, respectively. The calculation of this RMS value, which is only related to the statistics of the experiment, is discussed in section 7.2.1. As we see, all the fitters can be considered to be robust.

Besides, one can compare the goodness between the fitters, using the RMSE from Eq. (29). In Table 15 and Table 16 we have the same RMS values as in Fig. 67, and the upper bound of the absolute bias (in units of fm) from its relative values shown in Table 9. As it is shown in these tables, the RMS value from the other three fitters increase slightly compared to that from the Ratioanl (1,1). Since the difference in the bias is larger between different fitters, the RMSE is mostly determined by the bias. Among the three proposed fitters, the modRational (1,1), gives the smallest RMSE.

Required by the precision of the DRad experiment and limited by the number of the available deuteron form factor models, we thereby propose our discussed methods to search for a good fitter function and to test the robustness of the fitter, in order to extract the deuteron charge radius robustly.With the results shown in this note, we suggest to use the modRational (1,1) fitter of Eq. (47), by which we are able to reduce the upper bound of the relative bias in the fitting procedure from 0.169% (given by the Rational (1,1)) to 0.079% (given by the modRational (1,1)). These two numbers come from the smeared Abbott2 model. In Table 9 we can see that the smeared Abbott1 model gives a smaller bias value equal to 0.070% for the modRational (1,1) fitter, however, we take the number 0.079% as a conservative upper limit.

We follow the approach of Ref. [44] to treat the bias as one of the systematic uncertainties imposed on R_d. If we use the modRational (1,1) as a selected fitter for robustly extracting the deuteron charge radius, then in this case the bias will not be the dominant systematic uncertainty among those from other known sources. If we consider the total systematic uncertainty of R_d, then the reduction from 0.169% to 0.079% in the relative bias will be equivalent to 0.05%, which is an absolute number for the reduction of the total systematic uncertainty.

The radius extraction methods discussed above depend on a specific functional form. In Ref. [57], a fresh extraction of the charge radius of the proton is discussed. The cubic spline method is first used to interpolate the data, by which a smooth function is found. Then the radius is extracted with an extrapolation using that smooth function. This method perhaps may also be applicable for extraction of the deuteron charge radius in the future.

Fitter	Abbott1		
	RMS (fm)	Bias (fm)	RMSE (fm)
Rational (1,1)	0.00239	0.00287	0.00374
modRational (1,1)	0.00250	0.00147	0.00289
Fixed Rational (1,3)	0.00246	0.00370	0.00445
Fixed modRational (1,1)	0.00253	0.00477	0.00540

Table 15: The RMSE obtained from fitting with the pseudo-data generated by the Abbott1 smeared deuteron model.

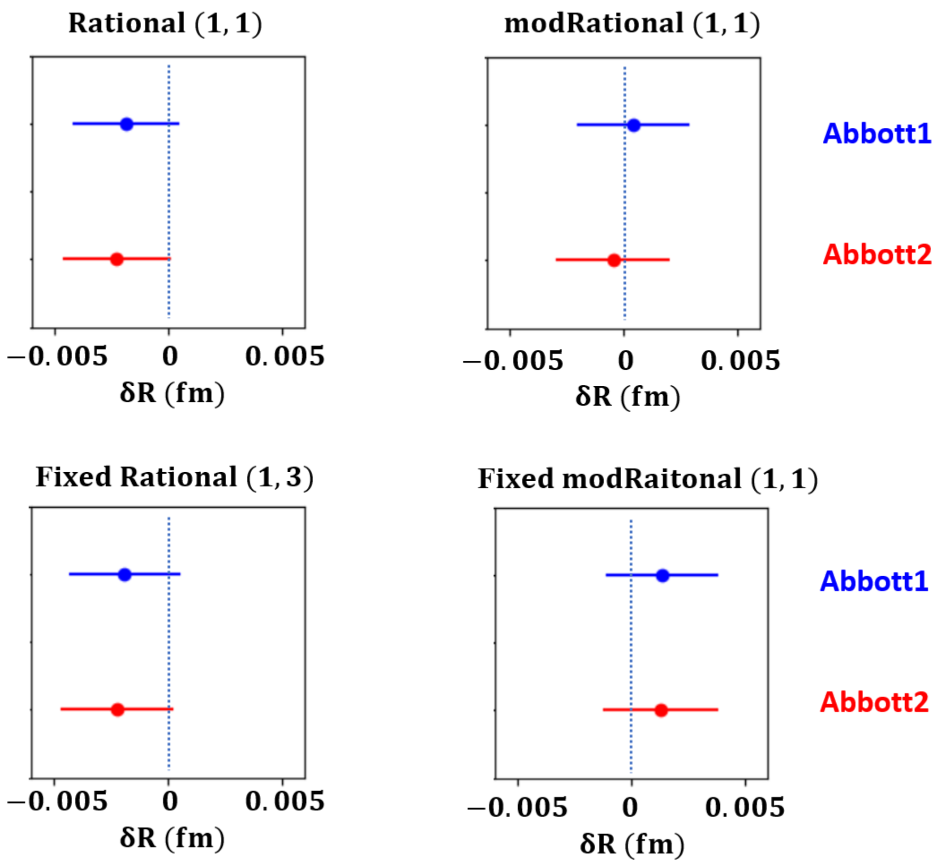

Figure 67: These four plots show the mean bias from Table 11 and Table 12, and the RMS obtained from fitting those four fitters with the pseudo-data (including statistical fluctuations before smearing) generated by the two given deuteron models.

Fitter	Abbott2		
	RMS (fm)	Bias (fm)	RMSE (fm)
Rational (1,1)	0.00236	0.00352	0.00424
modRational (1,1)	0.00246	0.00165	0.00296
Fixed Rational (1,3)	0.00243	0.00407	0.00474
Fixed modRational (1,1)	0.00250	0.00481	0.00542

Table 16: The RMSE obtained from fitting with the pseudo-data generated by the Abbott2 smeared deuteron model.